

Liquid-phase Synthesis of Structure-controllable Functional
Materials

ZHANG, Dieqing

A Thesis Submitted in Partial Fulfillment
of the Requirements for the Degree of
Doctor of Philosophy
in
Environmental Science

The Chinese University of Hong Kong
July 2010

UMI Number: 3445947

All rights reserved

INFORMATION TO ALL USERS

The quality of this reproduction is dependent upon the quality of the copy submitted.

In the unlikely event that the author did not send a complete manuscript and there are missing pages, these will be noted. Also, if material had to be removed, a note will indicate the deletion.



UMI 3445947

Copyright 2011 by ProQuest LLC.

All rights reserved. This edition of the work is protected against unauthorized copying under Title 17, United States Code.



ProQuest LLC
789 East Eisenhower Parkway
P.O. Box 1346
Ann Arbor, MI 48106-1346

Thesis/Assessment Committee

Professor Hung Kay LEE (Chair)

Professor Jimmy Chai Mei YU (Thesis Supervisor)

Professor Jian Fang WANG (Committee Member)

Professor Yun Feng LU (External Examiner)

Professor Kwong Yu CHAN (Alternate External Examiner)

Abstract

This thesis focuses primarily on the preparation of various functional materials with controllable structures and properties. The first part describes the synthesis of materials by solvothermal methods. The second part describes the rapid fabrication of novel semiconductor materials by microwave-assisted methods.

Part I: Size-tunable monodispersed hierarchical metallic Ni nanocrystals (58-190 nm in diameter) were prepared by the reduction of Ni^{2+} with hexadecylamine under atmospheric pressure. The diameter of the particles could be tuned by simply changing the reaction time. A reaction mechanism was proposed and the relationships between the size, hierarchical surfaces and the magnetic properties were investigated. The as synthesized Ni crystals exhibited higher coercivities than the bulk metallic material owing to the reduced size and the hierarchical surface structure. The saturation magnetization (M_s) and the ratio of remanence to saturation (M_r/M_s) increased with increasing particle size.

Bismuth oxyhalide semiconductors (BiOBr , BiOCl) with marigold-like open architectures were also prepared by a solvothermal method involving imidazolium-based ionic liquids and ethylene glycol. The 3D self-assembled marigold-like materials were effective photocatalysts for degrading organic pollutants and generating hydrogen. The main advantages of the new materials were

large surface area, high surface-to-bulk ratio, facile species transportation, and ease of recovery and regeneration.

Part II: A facile microwave-assisted solvothermal method was developed for the controlled synthesis of novel 3D CdS structures. Dendrite-, star-, popcorn- and hollow sphere-like CdS structures could be obtained by changing the reaction conditions including the reaction temperature and the amounts of reagents and solvents. The results revealed that the final structures were related to the solvent properties such as surface tension and viscosity. The degree of supersaturation was also responsible for the morphology variation and it could be adjusted by the reaction temperature. The CdS products with different morphologies exhibited interesting shape-dependent optical properties and photocatalytic activities.

Biocompatible anatase TiO₂ single-crystals with 27 % – 50 % chemically reactive {001} facets were obtained in 90 minutes by using a microwave-assisted method. The preparation involved an aqueous solution of titanium tetrafluoride and an ionic liquid (1-methyl-imidazolium tetrafluoroborate). The as-obtained TiO₂ single-crystals exhibited a truncated tetragonal bipyramidal shape. By simply changing the concentration of the ionic liquid, the level of reactive {001} facets can be continuously tuned from 27 % to 50 %. The use of microwave heating is critical as it allows rapid and uniform heating of the reaction mixture. The TiO₂

single-crystals were characterized by XRD, TEM, XPS and FESEM. The products exhibited excellent photocatalytic efficiency for both oxidation of nitric oxide in air and degradation of organic compounds in aqueous solution under UV light irradiation. The relationship between the physicochemical properties and the photocatalytic performance of the samples was discussed. The TiO₂ single-crystals were found to be nontoxic using Zebrafish (*D. rerio*) as a model.

By using a microwave-assisted hydrothermal method involving titanium tetrafluoride and a tetrafluoroborate-based ionic liquid (1-butyl-3-methyl-imidazolium-tetrafluoroborate), a micro-sheet anatase TiO₂ single crystal photocatalyst with remarkable 80 % reactive {001} facets was synthesized. The as-obtained TiO₂ single-crystal exhibited a truncated tetragonal bipyramidal shape. The high reactivity of {001} facets made these single crystals highly photocatalytically active. They were easily recyclable and thermally stable up to 800 °C.

Furthermore, a simple and environmentally benign approach for the synthesis of photocatalytically active rutile TiO₂ mesocrystals was developed. It was a microwave-assisted hydrothermal method involving titanium(III) chloride as the only reactant. The resulting 1D rutile nanowires could easily assemble into 3D hierarchical architectures without the help of surfactants or additives. The average

aspect ratio for the nanowires was 267. The BET specific surface area of the mesocrystal was 16 m²/g.

The optical band energy of the product exhibited an obvious red-shift of 0.2 eV with aspect to that of pure rutile TiO₂. This red-shift effect may be ascribed to the high aspect ratio of the rutile nanowires. The products showed excellent photocatalytic activity for NO removal in air and the activity was well maintained after three cycles. Gold modification on the rutile TiO₂ resulted in a 50 % improvement in the photocatalytic performance.

摘要

本博士论文研究工作主要涉及制备具有可控结构和性质的功能材料。第一部分讨论了通过溶剂热方法合成的材料及其应用。第二部分讨论了通过微波辅助的方法快速制备的新型半导体材料及其应用。

第一部分：在常压条件下，通过还原存在于十六烷基胺溶剂里的金属镍离子，可得到单分散的尺寸可调（58-190 nm）的多级金属镍纳米晶。通过简单的反应时间的改变，可实现粒子尺寸的可调性。我们研究了镍纳米晶形成的反应机理，也探讨了粒子尺寸，多级结构和磁性性质之间的关系。由于小尺寸效应和表面的多级结构，此法制备的金属镍纳米晶的矫顽磁性远远高于块状金属镍材料。随着粒子尺寸的增大，饱和磁化强度以及剩磁比也随之增大。

使用咪唑基离子液体和乙二醇作为反应体系，通过溶剂热的方法制备了具有万寿菊形状的溴氧铋及氯氧铋半导体开放结构材料。此类具有 3D 结构的半导体光催化材料能有效地降解有机污染物及产氢。此材料的优点在于：大比表面积、高表面对体积比，方便于反应物种的传输，易回收与再生。

第二部分：通过微波辅助溶剂热的方法合成了新型 3D 硫化镉结构。通过对反应温度，反应物的量以及反应溶剂的调变，合成了具有树枝状、星星状、爆米花状及中空球状的硫化镉结构。实验表明材料的结构与溶剂的性质（表面张力、溶液的粘度）密切相关。饱和度是材料形貌改变的另一个因素，它可以通

过反应温度的改变来调变。结果表明，不同形貌的硫化镉产品表现出不同的光学性质和光催化活性。

通过微波辅助的方法，使用 1-甲基咪唑四氟硼酸离子液体和四氟化钛的水溶液作为反应物，在 90 分钟内制备了具有生物兼容性的锐钛矿相二氧化钛微米单晶。此单晶具有可调的（27 %-50 %）化学反应活性面，即{001}面。此晶体显示了独特的两顶端被切割了的四面双锥结构。通过调变离子液体的浓度，{001}面的比例可以得到调变。实验研究发现，微波加热是反应的关键，它使反应均匀快速地进行。并且使用了 XRD, TEM, XPS and FESEM 等表征手段对此材料进行了进一步表征。在紫外光的照射下，此材料表现出很好的光催化氧化一氧化氮及降解水相中有机污染物的活性。此外，对光催化活性及材料物化性质之间的关系进行了讨论。使用斑马鱼进行毒性测试研究，结果证明该材料是生物兼容无毒的材料。

通过微波辅助的方法，使用 1-丁基 3-甲基咪唑四氟硼酸离子液体和四氟化钛的水溶液作为反应物，制备了微米尺寸的{001}活性面高达 80 %的单晶氧化钛薄片。此晶体显示了独特的两顶端被切割了的四面双锥结构。{001}面的高反应活性使得这些单晶具有超高的光催化活性。此产品容易回收，热稳定性高达 800 °C.

另外，通过简便环保的方法制备了具有光催化活性的晶红石相二氧化钛介晶。这是一种微波辅助的水热方法，其中三氯化钛作为唯一的反应物。反应生成的

晶红石相氧化钛纳米线能够自组装成 3D 多级结构,此过程不需要添加辅助剂或表面活性剂。氧化钛纳米线的平均长径比为 267。晶体的比表面积为 $16 \text{ m}^2/\text{g}$ 。

与普通的晶红石相氧化钛相比,此产品的禁带宽度显示了 0.2 eV 的红移。产生红移的原因归因于具有较高长径比的纳米线的存在。此产品显示了很好的去除空气中一氧化氮的光催化活性,在三次重复使用后,产品活性基本保持不变。

在此氧化钛表面修饰金,其光催化活性可以提高 50% 。

Acknowledgement

This dissertation was made possible by the help and support of many people. First of all, I would like to express my sincere gratitude and appreciation to my supervisor, Prof. Jimmy C. Yu, for his expert guidance and support. I have not only learnt a lot from him but have also been inspired by his dedicated attitude to science. I am also deeply impressed by his profound knowledge in research. I shall benefit from this experience in my future work and life. It has been a truly wonderful learning experience.

Special thanks are given to the thesis committee members, Prof. Hung Kay Lee, Prof. Jianfang Wang, Prof. Yunfeng Lu, and Prof. Kwong Yu Chan for their time and energy spent on reading this thesis.

My heartfelt thanks must also go to Dr. Guisheng Li, Dr. Xianfeng Yang and Feng Wang for their highly knowledgeable discussion. Their constructive comments were essential to the completion of this dissertation. I am also indebted to Prof. Frank Shun Cheng Lee and Mr. Yu Huang for their valuable help in the photocatalytic oxidation of NO gas. Thanks to Prof. H. X Li for UV-vis and XPS measurements, Prof. K. M. Chan for toxicity studies and Prof. P. K. Wong for anti-bacteria tests. I am also grateful to Mr. Man Hau Yueng for his TEM analysis.

My sincere thanks are also extended to my groupmates for their generous help,

support and encouragement. They have made my life so fantastic and provided me an enjoyable environment in which to work. I would like to acknowledge all the staff members in the Department of Chemistry for the contribution to an active academic atmosphere. In addition, this research work was made possible by the generous financial support of the Research Grants Council of Hong Kong.

Lastly, and most importantly, I feel very grateful to my parents, mother-in law, my love and my son for their unconditional love, concern, support and patience for the pursuit of my Ph.D. They are the source of my motivation and happiness. Thanks must also go to all my friends who have constantly offered me words of encouragement. Thank you for always being there for me. You have all helped to make my Ph.D. study inspiring and rewarding.

May 2010

Zhang, Dieqing

Environmental Science Programme

The Chinese University of Hong Kong

List of Figures

Figure 1.1 The four principal possibilities to explain the 3D mutual alignment of nanoparticles to a mesocrystal. Reproduced from Reference 51

Figure 1.2 Discharge capacities for A) normal (\blacktriangle), B) nanowire (\star), and C) mesoporous (\circ) forms of LT-LiCoO_2 . Reproduced from Reference 74

Figure 1.3 SEM images of electrospun nanofibers: (a) electrospun $\text{PVA/Fe(NO}_3)_3 \cdot 9\text{H}_2\text{O}$ composite nanofibers at low magnification; (b) electrospun $\text{PVA/Fe(NO}_3)_3 \cdot 9\text{H}_2\text{O}$ composite nanofibers at high magnification; (c) calcined in air at 800°C for 6 h; and (d) TEM image of electrospun nanofibers calcined in air at 800°C for 6 h. Reproduced from Reference 80

Figure. 1.4 Images of *M. lylae* colonies on an agar plate before and after visible light irradiation. Reproduced from Reference 115

Figure 1.5 Band position of selective semiconductors and the redox potentials of O_2/O_2^- and $\cdot\text{OH}/\text{H}_2\text{O}$ redox couples at $\text{pH} = 7$, (a) oxide and (b) Non-oxide semiconductors.

Figure 1.6 SEM and TEM (insets) images of the titania spheres synthesized for (a) 1/24, (b) 0.5, (c) 1, (d) 2, (e) 7, and (f) 14 days, showing transiting interior structure from dense, to sphere-in-sphere, to hollow and surface morphology from smooth to prickly. Reproduced from Reference 127

Figure 1.7 (a) SAXS patterns of $\text{ompg-C}_3\text{N}_4$ and SBA-15 template. The inset shows the corresponding 2D SAXS image of $\text{ompg-C}_3\text{N}_4$. (b, c) TEM images of $\text{g-C}_3\text{N}_4$. The inset in the TEM image shows the corresponding fast Fourier transforms of the patterns. Reproduced from Reference 151

Figure 2.1 TEM, high magnification TEM and FESEM images of the nickel nanocrystals obtained at 210 °C for different reaction times using 0.2 g nickel acetate tetrahydrate. a), b), c) 30 min, d), e), f) 40 min, g), h), i) 50 min, j), k), l) 60 min.

Figure 2.2 Mean particle size (D) of the Ni crystals as a function of reaction time (t).

Figure 2.3 a) Powder XRD patterns of the samples prepared at 210 °C for different durations. b) HRTEM image and c) EDX pattern of the sample prepared at 210 °C for 60 min reaction.

Figure 2.4 Powder XRD patterns of Ni nanocrystals prepared at 200 °C for different durations using 1 g nickel acetate tetrahydrate.

Figure 2.5 TEM images of the samples prepared at 200 °C for different durations. a-c) 1 hr, d) 3 hrs, e) 6 hrs, f) 7 hrs, g,h) 12 hrs, and i) 18 hrs.

Figure 2.6 a) Magnetization loops of (a) Ni nanocrystals prepared at 210 °C for different reaction times using 0.2 g nickel acetate tetrahydrate. i) 30 min (-◇-), ii) 40 min (-△-), iii) 50 min (-●-), iv) 60 min (-■-). b) coercivity, H_c (-■-), and remanence to saturation ratio, M_r/M_s (-○-) vs particle sizes of Ni nanocrystals prepared at 210 °C for different reaction time.

Figure 3.1 SEM images (a-d), TEM (e) and HTTEM (f) images, SAED (g) and EDX pattern (h) of BiOBr.

Figure 3.2 XRD patterns of as-prepared BiOX (X=Cl, Br) powders.

Figure 3.3 FESEM images (a, b) and TEM (c) and HRTEM images of BiOCl.

Figure 3.4 Pore-size distributions and N_2 adsorption and desorption isotherms (inset) for the BiOBr powders (a, -■-) and BiOCl (b, -○-) powders.

Figure 3.5 (a) Photocatalytic H_2 evolution from an aqueous solution of 20 vol %

methanol containing BiOBr and P25 in the presence of H_2PtCl_6 . (b) Photocatalytic oxidative decomposition of MB aqueous solution containing BiOBr and P25. (c) Survival ratio of *M. lylae* vs irradiation time for BiOBr powders.

Figure 4.1 XRD pattern (a), Survey XPS spectrum (b), High-resolution XPS Cd 3d spectrum (c) and S 2p spectrum (d) of sample 1.

Figure 4.2 FESEM images (a and b) and TEM image (c) of sample 1. HRTEM image (d) recorded on the tip of the nanorod. EDX spectrum (e) of sample 1. The signal of Cu is generated from the Cu grids.

Figure 4.3 FESEM and TEM images of sample 2 (a and b) and sample 3 (c and d).

Figure 4.4 SEM images of the samples obtained by different volume ratios of EG/water at different temperature: (a) 0:1, 160 °C (sample 4), (b) 1:1, 160 °C (sample 5), (c) 9:1, 160 °C (sample 6), (d) 0:1, 130 °C (sample 7), (e) 1:1, 130 °C (sample 8), (f) 9:1, 130 °C (sample 9).

Figure 4.5 FESEM (a) and TEM images (b) of sample 8.

Figure 4.6 TEM images of the products prepared at 190 °C with various microwave irradiation time: (a) 1 min (sample 10), (b) 10 min (sample 11), (c) 20 min (sample 12), (d) 30 min (sample 1).

Figure 4.7 XRD patterns of CdS crystals obtained at 190 °C for (a) 1 min (sample 10), (b) 10 min (sample 11), (c) 20 min (sample 12) and (d) 30 min (sample 1).

Figure 4.8 UV-vis (a), PL (b) and Raman spectra (c) of sample 1, 2, 3 (line a, b, c).

Figure 4.9 A comparison of the photoactivities of dendrite-like (sample 1, -▼-), star-like (sample 2, -○-), popcorn-like (sample 3, -△-), sphere-like (sample 8, -■-),

P25 (Degussa, -▲-) and without photocatalysts (-◆-). A is the absorbance of methylene blue ($\lambda_{\text{max}} = 664 \text{ nm}$) and A_0 is the initial absorbance.

Figure 5.1 Typical XRD pattern (a), low-magnification FESEM image (b) and side view FESEM image (c, d) of Sample 1 prepared with 30 mL 0.04 M TiF_4 and 0.5 mL ionic liquid at 210 °C for 90 min.

Figure 5.2 TEM image (a), ED pattern (b), HRTEM image (c) and corresponding intensity profile for the line scan across the lattice fringes (inset) of Sample 1 prepared with 30 mL 0.04 M TiF_4 and 0.5 mL ionic liquid at 210 °C for 90 min.

Figure 5.3 X-ray photoelectron survey spectra (a), fine scan of Ti 2p (b) and F 1s (c) of Sample 1 prepared with 30 mL 0.04 M TiF_4 and 0.5 mL ionic liquid at 210 °C for 90 min.

Figure 5.4 TEM image of hollow anatase TiO_2 nanospheres obtained in the absence of ionic liquid (a) and SEM image of anatase TiO_2 single-crystal aggregates obtained under conventional hydrothermal condition at 210 °C for 48 h (b).

Figure 5.5 FESEM images of Sample 2 (a, b) and Sample 3 (c, d) prepared with 1 mL and 2 mL ionic liquid at 210 °C for 90 min.

Figure 5.6 Simulated models for Samples 1-3, indicating increasing tendency of the percentage of {001} facets.

Figure 5.7 XRD pattern (a) and SEM image (b) of conventional TiO_2 .

Figure 5.8 (a) Plots of the decrease in NO concentration vs irradiation time in the presence of different photocatalysts. (b) Dependence of $\ln(C/C_0)$ on irradiation time. (c) Initial rate constant (-○-) and removal rate (-■-) of NO for TiO_2 single-crystals with different percentage of {001} facets.

Figure 5.9 The effectiveness of the conventional TiO₂ single-crystal and Samples 1-3 on the degradation of 4-chlorophenol under UV irradiation.

Figure 5.10 Livability of 4-day larvae after 24 h exposure to different concentrations of aqueous anatase TiO₂ single-crystals (Sample 3).

Figure 6.1 FESEM image a), Simulated model b), TEM image of a representative anatase single crystal recorded along the [001] axis c), SAED pattern d) and HRTEM image e) of the anatase TiO₂ exposed with reactive {001} facets.

Figure 6.2 Side-view FESEM images of the anatase single crystals exposed with {001} facets.

Figure 6.3 XRD pattern of the anatase single crystal exposed with {001} facets.

Figure 6.4 a) Simulated shape of the TiO₂ anatase single crystal samples. b) Equilibrium shape of anatase TiO₂ crystal. c) the calculation process of S_{001} , is the theoretical value for the angle between the [001] and [101] facets of anatase, GH/IJ is the degree of truncation).

Figure 6.5 F-(001) surfaces of anatase single crystal using. a) HF and b) ionic liquid as the morphology controlling agent. The purple planes are the {001} facets. The elements O, Ti, F and B are shown in red, blue, yellow and white.

Figure 6.6 SEM image a) and XRD pattern c) of the anatase hollow spheres prepared without ionic liquid. SEM image b) and XRD pattern d) of the {001} unexposed TiO₂ single crystals.

Figure 6.7 The effectiveness of samples with (-☆-) or without (-△-)exposed reactive {001} facets on the degradation of 4-chlorophenol under UV irradiation.

Figure 6.8 The recycle experiments of anatase TiO_2 single crystal exposed with $\{001\}$ facets.

Figure 6.9 XRD patterns of a) anatase single crystals exposed with $\{001\}$ facets and b) TiO_2 powders prepared by conventional sol-gel method calcined at different temperatures.

Figure 7.1 SEM image of the self-assembled rutile TiO_2 by microwave heating TiCl_3 at $200\text{ }^\circ\text{C}$ for 1 min.

Figure 7.2 XRD pattern (a), SEM (b), TEM (c) and HRTEM (d) image of the self-assembled rutile TiO_2 by microwave heating TiCl_3 at $200\text{ }^\circ\text{C}$ for 1 min.

Figure 7.3 Nitrogen adsorption-desorption isotherm (a) and BJH pore size distribution plot (b) of the rutile TiO_2 .

Figure 7.4 UV-visible absorption spectrum and determination of indirect interband transition energy (inset) for the rutile TiO_2 .

Figure 7.5 NO removal rate of rutile TiO_2 , Au/rutile TiO_2 and P25 in a single pass flow of air under ultraviolet light (a) and simulated solar light (b). Initial concentration of NO = 400 ppb.

Figure 7.6 Cyclability of the rutile TiO_2 for NO removal in a single pass flow of air.

Figure 7.7 XPS spectra of Au4f, Ti2p and O1s of the pure and gold-doped rutile TiO_2 .

Figure 7.8 UV-visible absorption spectra for the rutile TiO_2 and gold doped rutile TiO_2 .

List of Tables

Table 4.1 Summaries of the experimental results indicating the influence of the composition of a mixed solution on the shape of the product.

Table 5.1 Summary of experimental conditions and physical properties of different samples.

List of Scheme

Scheme 1.1 General reaction scheme displaying the metal oxide precursors used, the solvent, the experimental conditions, and the resulting metal oxide nanoparticles.

Scheme 2.1 Illustration of a proposed mechanism for the formation of Ni nanocrystals.

Scheme 4.1 Proposed growth process for dendritic CdS crystals (sample 1).

Scheme 5.1 Formation mechanism of {001} facets exposed TiO₂ by microwave irradiation.

Table of Contents

| | Page |
|--|-------------|
| Abstract | I |
| Abstract (Chinese) | V |
| Acknowledgement | Viii |
| Lists of Figures | X |
| Lists of Tables | Xvi |
| Lists of Scheme | Xvi |
| Table of Contents | Xvii |
| Chapter 1 Introduction | 1 |
| 1.1 Functional Materials | 1 |
| 1.1.1 Nanocrystals | 1 |
| 1.1.2 Mesocrystals | 3 |
| 1.2 Applications of Advanced Nanomaterials | 4 |
| 1.2.1 New Electrode Materials for Lithium-Based Batteries | 4 |
| 1.2.2 Sensors Based on Functional Materials | 6 |
| 1.2.3 Multifunctional Magnetic Nanocomposites | 9 |
| 1.2.4 Antibacterial Functional Materials | 10 |

| | | |
|---------|---|----|
| 1.2.5 | Functional Materials for Treating Organic Pollutants | 15 |
| 1.2.6 | Photocatalytic Materials for H ₂ Evolution | 18 |
| 1.2.6.1 | Polymeric Photocatalysts | 19 |
| 1.2.6.2 | A “Nonsacrificial” Two-step Water Splitting System | 20 |
| 1.2.7 | Functional Materials for Valuable Hydrocarbons Evolution from CO ₂ | 21 |
| 1.3 | Syntheses of Nanomaterials | 24 |
| 1.3.1 | Preparation Methods | 24 |
| 1.3.2 | Solvothermal Processing | 24 |
| 1.3.3 | Microwave Synthesis | 25 |
| 1.3.3.1 | Background | 25 |
| 1.3.3.2 | Literature Survey | 26 |
| 1.3.3.3 | Summary and Outlook | 30 |
| 1.4 | Summary | 31 |
| 1.5 | Aim of This Research and Its Significance | 31 |
| 1.6 | References | 33 |

Chapter 2 Synthesis of Size-Tunable Monodispersed Metallic 48

Nickel Nanocrystals without Hot Injection

| | | |
|-------|--|----|
| 2.1 | Introduction | 48 |
| 2.2 | Experimental Section | 50 |
| 2.2.1 | Preparation of Monodispersed Nickel Nanocrystals | 50 |
| 2.2.2 | Characterization | 51 |
| 2.3 | Results and Discussion | 51 |
| 2.3.1 | TEM and HRTEM Analysis | 51 |
| 2.3.2 | XRD Analysis | 55 |
| 2.3.3 | Growth Process | 57 |
| 2.3.4 | Magnetic property | 62 |
| 2.4 | Conclusion | 64 |
| 2.5 | References | 65 |

Chapter 3 Ionic Liquids-Assisted Synthesis of 3D BiOX 68

(X=Br, Cl) Ternary Compounds Mesocrystals

| | | |
|-------|-----------------------------|----|
| 3.1 | Introduction | 68 |
| 3.2 | Experimental Section | 71 |
| 3.2.1 | Preparation of BiOBr Sample | 71 |

| | | | |
|------------------|-------|---|-----------|
| | 3.2.2 | Characterization | 71 |
| | 3.2.3 | Measurements of Photocatalytic Activity | 72 |
| | 3.2.4 | Measurements of Bactericidal Activity | 74 |
| 3.3 | | Results and Discussion | 75 |
| | 3.3.1 | TEM and XRD Analysis | 75 |
| | 3.3.2 | N ₂ Adsorption-Desorption Analysis | 80 |
| | 3.3.3 | Photocatalytic Activity | 81 |
| | 3.3.4 | Bactericidal Activity | 82 |
| 3.4 | | Conclusion | 85 |
| 3.5 | | References | 86 |
| Chapter 4 | | Microwave-Assisted Architectural Control | 90 |
| | | Synthesis of 3D CdS Structures | |
| 4.1 | | Introduction | 90 |
| 4.2 | | Experimental Section | 92 |
| | 4.2.1 | Chemicals | 92 |
| | 4.2.2 | Preparation | 92 |
| | 4.2.3 | Photocatalytic Activity Test | 94 |
| | 4.2.4 | Characterization | 94 |
| 4.3 | | Results and Discussion | 96 |

| | | |
|------------------|---|------------|
| 4.3.1 | XRD and XPS Analysis | 95 |
| 4.3.2 | SEM, TEM and EDX Analysis | 97 |
| 4.3.3 | Solvent-Induced Morphology Variation | 99 |
| 4.3.4 | Reaction Temperature-Induced Morphology Variation | 100 |
| 4.3.5 | Reaction Time-Induced Morphology Variation | 102 |
| 4.3.6 | Growth Mechanism | 104 |
| 4.3.7 | Spectroscopic Study | 108 |
| 4.3.8 | Photocatalytic Activity | 111 |
| 4.4 | Conclusions | 112 |
| 4.5 | References | 113 |
| Chapter 5 | Anatase Single-Crystal Photocatalysts with Tunable Percentage of Reactive Facets | 117 |
| 5.1 | Introduction | 117 |
| 5.2 | Experimental Section | 121 |
| 5.2.1 | Preparation of TiO ₂ with Tunable Percentage of Reactive Facets | 121 |
| 5.2.2 | Characterization | 122 |

| | | |
|------------------|--|------------|
| 5.2.3 | Photoactivity Test | 122 |
| 5.2.4 | Toxicity Study | 125 |
| 5.3 | Results and Discussion | 127 |
| 5.3.1 | XRD and SEM Analysis | 126 |
| 5.3.2 | TEM Analysis | 129 |
| 5.3.3 | XPS Analysis | 130 |
| 5.3.4 | The Mechanism for the Formation of {001} Facets Exposed TiO ₂ | 133 |
| 5.3.5 | Photocatalytic Performance Study | 137 |
| 5.3.6 | Toxicity Study | 140 |
| 5.4 | Conclusion | 142 |
| 5.5 | References | 142 |
| Chapter 6 | A Micrometer-Size TiO₂ Single Crystal Photocatalyst with Remarkable 80 % Reactive Facets | 148 |
| 6.1 | Introduction | 148 |
| 6.2 | Experimental Section | 151 |
| 6.2.1 | Preparation of TiO ₂ with Reactive Facets | 151 |
| 6.2.2 | Measurement of Photocatalytic Activity | 152 |

| | | | |
|------------------|-------|---|------------|
| | 6.2.3 | Characterization | 153 |
| 6.3 | | Results and Discussion | 154 |
| | 6.3.1 | FESEM, TEM and XRD Analysis | 154 |
| | 6.3.2 | The role of Ionic Liquid | 157 |
| | 6.3.3 | Photocatalytic Activity | 159 |
| | 6.3.4 | Thermal Stability Study | 162 |
| 6.4 | | Conclusions | 163 |
| 6.5 | | References | 163 |
| Chapter 7 | | Green Synthesis of a Self-Assembled Rutile Mesocrystalline Photocatalyst | 167 |
| | | Mesocrystalline Photocatalyst | |
| | 7.1 | Introduction | 167 |
| | 7.2 | Experimental Section | 168 |
| | 7.2.1 | Preparation of Photocatalysts | 168 |
| | 7.2.2 | Characterization | 169 |
| | 7.2.3 | Measurement of Photocatalytic Activity | 170 |
| | 7.3 | Results and Discussion | 171 |
| | 7.3.1 | XRD, SEM and TEM Measurements | 171 |
| | 7.3.2 | BET Analysis | 174 |
| | 7.3.3 | UV/Vis Diffuse Reflectance Spectroscopy | 175 |

| | | |
|------------------|-----------------------------|------------|
| 7.3.4 | Photocatalytic Activity | 177 |
| 7.4 | Conclusion | 182 |
| 7.5 | References | 182 |
| Chapter 8 | Conclusion | 186 |
| | List of Publications | 189 |

Chapter One

Introduction

1.1 Functional Materials

Functional materials cover a broad range of substances such as the magnetic materials, catalytic materials, electrical materials, optical materials, sensor materials and biological materials. Nanotechnology can create almost limitless kinds of novel functional materials in a variety of ways, including sol process,¹ micelles²⁻⁴, sol-gel process,^{5,6} chemical precipitation,^{7,8} hydrothermal synthesis,⁹⁻¹¹ pyrolysis,¹²⁻¹⁵ vapor deposition,^{16,17} supercritical treatment,¹⁸ and solution combustion synthesis.^{19,20} Functional materials usually exist in the forms of nanocrystals and mesocrystals.

1.1.1 Nanocrystals

Nanocrystals can be described as 'novel materials whose size of elemental structure has been engineered at the nanometer scale'.²¹ Materials in the nanometer size range often exhibit new property.²² Intervention in the properties of materials at the nanoscale permits the creation of materials and devices with remarkable functionality.²³

Nanocrystals include clusters of atoms (quantum dots, nanodots, inorganic macromolecules), grains that are less than 100 nanometers in size (nanocrystalline, nanophase, nanostructured materials), fibres that are less than 100 nanometers in diameter (nanorods,²⁴ nanoplatelets,^{25,26} nanotubes,²⁷ nanofibrils,²⁸ nanowires²⁹), films that are less than 100 nanometers in thickness, nanoholes, and composites that are a combination of these. The composition can be any combination of naturally occurring elements, with the more important compositions being silicates,³⁰ carbides,³¹ nitrides,³² oxides,³³ borides,³⁴ selenides,³⁵ tellurides,³⁶ sulfides,³⁷ halides,³⁸ alloys,³⁹ intermetallics,⁴⁰ metals,⁴¹ organic polymers,⁴² and composites.⁴³

Nanocrystals have been widely utilized in various areas, such as light emitting devices,⁴⁴ luminescent tags,⁴⁵ photocatalysis,⁴⁶ and biomedical applications.^{47,48} Magnetic nanocrystals can be used as efficient diagnostic tools in magnetic resonance imaging, magnetic separation of biological targets⁴⁸ and drug/gene delivery.⁴⁹ Plasmonic properties of noble metal nanocrystals are utilized in molecular-specific imaging and sensing, as well as in photodiagnostic and photothermal therapy.⁵⁰

1.1.2 Mesocrystals

In analogy with atoms and molecules, nanocrystals can also serve as building units to construct mesocrystals. The notation “mesocrystal” is an abbreviation for a mesoscopically structured crystal, which is an ordered superstructure of crystals with mesoscopic size (1~1000 nm). Recently, mesocrystals are experiencing rapidly increasing attention of chemists, physicists, and materials scientists for their special mesoscopic structure, offering unique new opportunities for materials design.⁵¹

Mesocrystals can be regarded as assemblies of crystallographically oriented nanocrystals. They have single-crystal-like atom structures and scattering behaviors but with much higher porosities than conventional single crystals.⁵² Mesocrystals have much higher crystallinity than polycrystalline materials and in some cases even exhibit many characteristic properties of a conventional single crystal.⁵³

Several mechanisms were reported for the formation of mesocrystals.⁵¹ Four basic mechanisms were proposed to form a mesocrystal as shown in Fig.1.1: a) Alignment of nanoparticles by an oriented organic matrix; b) Nanoparticle alignment by physical fields or mutual alignment of identical crystal faces; c) Epitaxial growth of a nanoparticle employing a mineral bridge connecting the two nanoparticles; d) nanoparticle alignment by spatial constraints.⁵¹

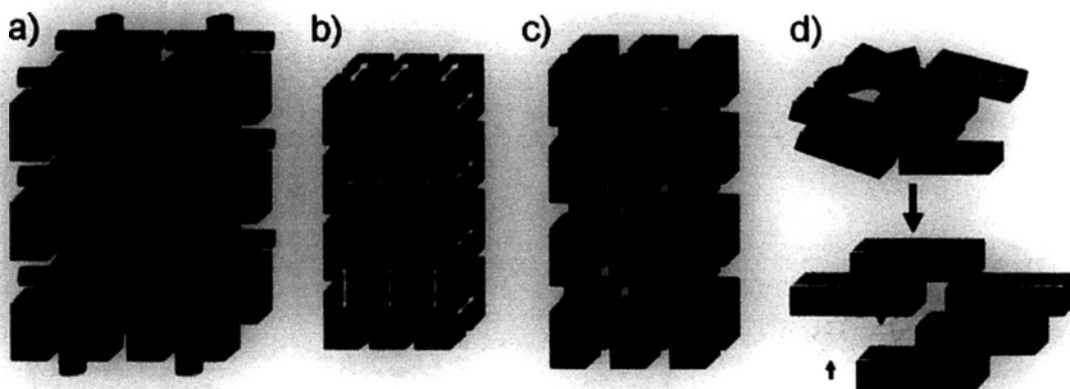


Figure 1.1 The four principal possibilities to explain the 3D mutual alignment of nanoparticles to a mesocrystal. Reproduced from Reference 51.

To date, mesocrystals can be mainly classified into three types: 1) metal oxide-based mesocrystals (ZnO^{54} , WO_3 ,⁵⁵ MgO ,⁵⁶ CeO_2 ,⁵⁷ Fe_3O_4 ,⁵⁸ and TiO_2 ⁵⁹). 2) binary metal oxides-based mesocrystals (BiVO_4 ,⁶⁰ Bi_2WO_6 ,⁶¹ CaMoO_4 ,⁶² SrTiO_3 ,⁶³ and PbTiO_3 ⁶⁴). 3) other functional inorganic materials (CeF_3 ,⁶⁵ GaPO_4 ,⁶⁶ CdS/CdSe ,⁶⁷ Ag ⁶⁸ and PbS ⁶⁹). Such novel mesocrystals are ordered nanocrystal assemblies with a huge potential for the synthesis of advanced materials.⁷⁰

1.2 Applications of Advanced Nanomaterials

1.2.1 New Electrode Materials for Lithium-Based Batteries

Tremendous research effort has been devoted to improving the incomparable performance of lithium-ion batteries. Various nanostructured anodes based on transition metal oxides have been reported.⁷¹⁻⁷³ Owing to the nanocomposite nature

of these electrodes, the conversion reactions are highly reversible, providing large capacities that can be maintained for hundreds of cycles.⁷² To date, different nanostructured materials such as nanoparticles, nanotubes, wires and nanoalloys have been used as high efficient anode/cathode materials.⁷³

Very recently, Bruce et al. demonstrated the low-temperature synthesis of ordered mesoporous LiCoO_2 via a hard template route.⁷⁴ This material exhibited superior properties as a cathode compared with the same compound in nanoparticulate form. As shown in Fig. 1.2, the first discharge capacity for mesoporous LiCoO_2 is some 20 mA h g^{-1} higher than that for the equivalent nanowire material. The initial discharge capacity of normal LiCoO_2 lies between the two nanostructured materials. The capacity of the mesoporous LiCoO_2 decreases by around 45 % after 50 cycles whereas the drop is 75 % for normal LiCoO_2 .

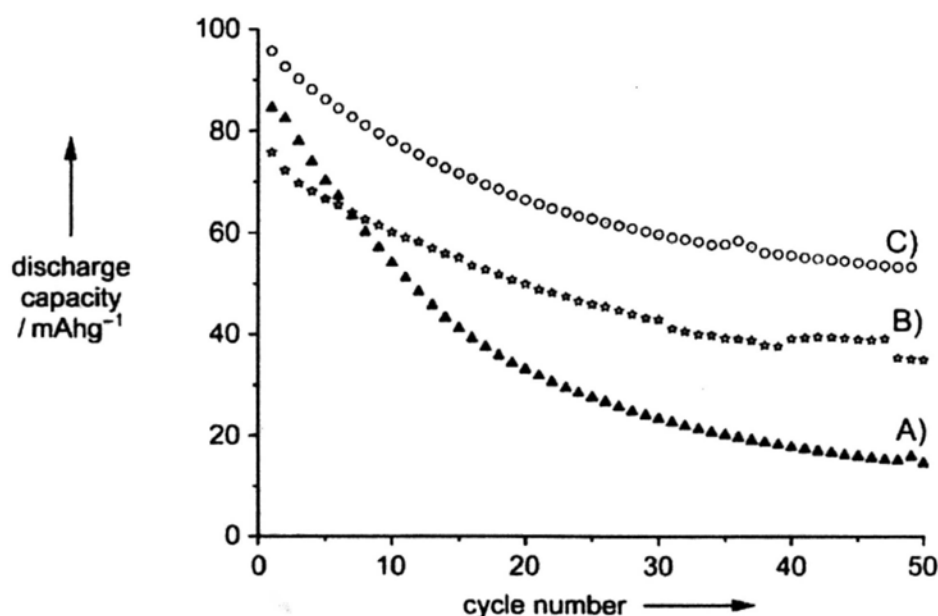


Figure 1.2 Discharge capacities for A) normal (\blacktriangle), B) nanowire (\star), and C) mesoporous (\circ) forms of LT-LiCoO_2 . Reproduced from Reference 74.

Generally, the nanomaterials for lithium batteries offer many advantages: 1) They allow electrode reactions to occur that cannot take place for materials composed of micrometer-sized particles.⁷⁵ 2) Owing to the short distances for lithium-ion transport within the nanoparticles, the reduced dimensions significantly increases the rate of lithium insertion/removal.⁷² 3) A high surface area permits a high contact area with the electrolyte and hence a high lithium-ion flux across the interface. 4) Electron transport within the particles is also enhanced by nanometer-sized particles, as described for lithium ions.⁷² 5) For very small particles, the chemical potentials for lithium ions and electrons may be modified, resulting in a change of electrode potential (thermodynamics of the reaction). 6) The range of composition over which solid solutions exist is often more extensive for nanoparticles and the strain associated with intercalation is often better accommodated.⁷³

1.2.2 Sensors Based on Functional Materials

Sensors capable of detecting and even quantifying both simple and complex gas mixtures present a far more facile analytical method than capturing samples and analyzing them using conventional equipments. In particular, electronic noses are very attractive for on-site monitoring of priority pollutants, as well as for addressing other environmental needs.⁷⁶ New types of chemical sensors for environmental

monitoring, food safety or security applications could be based on nanotechnology. Nanomaterials are very well suited for chemical sensor applications, because their physical properties often vary considerably in response to changes of the chemical environment.

It is well known that the *n*-Type semiconductor metal oxides such as SnO₂, Al₂O₃, ZnO, Fe₂O₃ and TiO₂ are widely utilized as gas sensing nanomaterials owing to their outstanding gas-sensing properties for the detection of flammable and toxic gases at relatively low cost.⁷⁶ When the charge accepting molecules (e.g., NO₂ and O₂) are adsorbed at the vacancy sites, electrons are effectively depleted from the conduction band, thus decreasing conductivity of the *n*-type oxide. Also, oxygen molecules are generally chemisorbed onto the surface of oxides as O₂⁻, O⁻, or O²⁻ species that exist in an equilibrium state (O₂⁻ ⇌ O⁻ ⇌ O²⁻ ⇌ O₂).⁷⁷ Upon being exposed to a reductive gas, such as H₂, CO and alcohol, the surface-adsorbed oxygen species of the *n*-type oxide will react with the gas. This will lower the surface concentration of oxygen species, resulting in an increased conductivity. By measuring the variation in resistance or conductance, gas sensors made of these *n*-type oxides can intelligently detect different kinds of gases.⁷⁸

Recently, a variety of nanostructured Fe₂O₃ such as nanospheres,⁷⁹ nanofibers,⁸⁰ nanocubes⁸¹ and nanotubes⁸² have been investigated for gas sensing. Wang et al.

prepared α -Fe₂O₃ ceramic nanofibers through electrospinning poly(vinyl alcohol)/Fe(NO₃)₃·9H₂O composite nanofibers and calcinations. The as-prepared α -Fe₂O₃ nanofibers, as shown in Fig. 1.3, exhibit rapid response-recovery and high sensitivity characteristics to ethanol vapor.⁸⁰

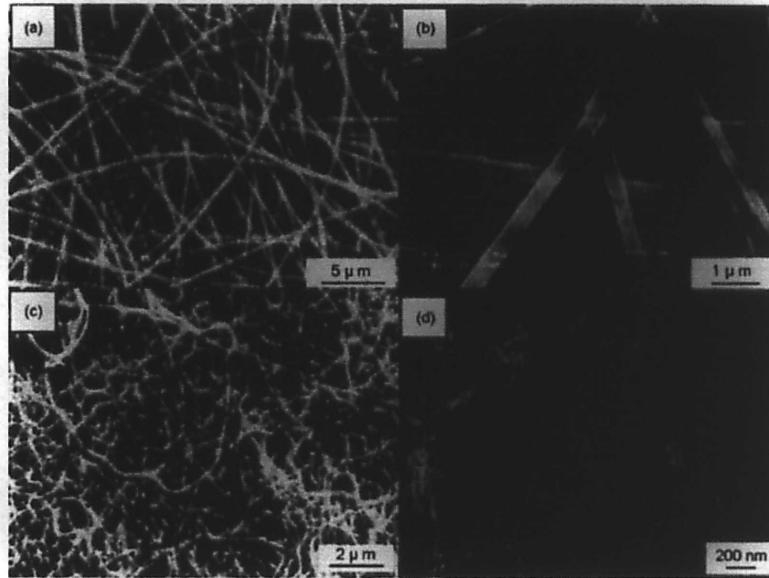


Figure 1.3 SEM images of electrospun nanofibers: (a) electrospun PVA/Fe(NO₃)₃·9H₂O composite nanofibers at low magnification; (b) electrospun PVA/Fe(NO₃)₃·9H₂O composite nanofibers at high magnification; (c) calcined in air at 800 °C for 6 h; and (d) TEM image of electrospun nanofibers calcined in air at 800 °C for 6 h. Reproduced from Reference 80.

Wang et al. reported that SnO₂ monolayer porous hollow spheres, prepared by hard-template route with carbon spheres as templates, exhibited high sensitivity to ethanol.⁸³ Yang et al. synthesized CNT/Au/SnO₂ nanotubes through homogeneous deposition of Au and SnO₂ nanocrystals on carbon nanotubes via layer-by-layer assembly. The as-prepared CNT/Au/SnO₂ nanotubes exhibited excellent sensor performance to CO at room temperature owing to the doping of Au nanocrystals, the

higher surface-to-volume ratio and nanotubular structure.⁸⁴

Despite its great potential for environmental monitoring, broad applications of sensor technology for the control of air and water quality are still in their infancy. In particular, recent advances in novel nanostructured materials serving as sensing units will certainly expand the scope of the sensors towards a wide range of organic and inorganic contaminants.⁷⁶

1.2.3 Multifunctional Magnetic Nanocomposites

Multifunctional nanocomposites with desirable properties have attracted broad interest in recent years.⁸⁵ The applications of nanocomposites with both fluorescent and magnetic properties have been widely explored for bioimaging, diagnosis, and therapeutics.⁸⁶⁻⁸⁹ These multifunctional magnetic nanocomposites can be used as luminescent markers, and they can also be controlled by an external magnetic field. Most of the magnetic fluorescent nanocomposites are core-shell structures with the great majority of emitters being either quantum dots (QDs) or organic dyes.⁸⁵

Lots of efforts have been devoted into the development of magnetic fluorescent nanocomposites. Generally, the preparation methods can be grouped into four classical types: a) a magnetic core covalently bound to a fluorophore via a spacer.⁹⁰ b) a magnetic core coated with silica,⁹¹ lipid,⁹² or polymer⁹³ containing fluorescent

components. c) a magnetic core directly coated with a fluorescent shell.⁹⁴ d) magnetic nanoparticles and QDs encapsulated in a polymer or silica matrix.⁹⁵

Recently, Zhao and Xiao et al. fabricated submicrometer laminated Fe/SiO₂ soft magnetic composites via controlled deformation and subsequent sol-gel coating processes. The bulk materials made of these laminates show flat permeability spectra up to 50 MHz, about two orders of magnitude higher than those made of the parent powders. In addition, the composites have large saturation fields, and thus can be used in high-power devices.⁹⁶ Hyeon et al. synthesized discrete and monodispersed mesoporous silica nanoparticles consisting of a single Fe₃O₄ nanocrystal core and a mesoporous silica shell. They believed that the integrated capability of such core-shell to be used as magnetic resonance and fluorescence imaging agents, along with their potential use as a drug delivery vehicle, could make them a novel candidate for future cancer diagnosis and therapy and for drug delivery.⁹⁷

1.2.4 Antibacterial Functional Materials

Traditional water disinfection methods such as chlorination and ozonation inevitably form harmful disinfection by-products (DBPs). UV irradiation is a safe alternative but it is very energy intensive. It makes perfect sense to enhance the utilization of photons by integrating engineered photocatalytic nanostructures in the

treatment system. Since Matsunaga et al. reported the efficiency of photocatalytic oxidation of *Saccharomyces cerevisiae* (yeast), *Lactobacillus acidophilus* and *Escherichia coli* (bacteria), and *Chlorella vulgaris* (green algae) in water using a Pt-TiO₂ photocatalyst upon illumination with near-UV light, interest in using TiO₂-mediated photocatalysis for water disinfection has grown steadily.⁹⁸ A great of research work was carried out on the preparation of TiO₂-based photocatalytic disinfectants. They can be classified into two categories: TiO₂ suspension system and coated TiO₂ film system.

The use of aqueous suspensions of TiO₂ photocatalysts has been widely investigated. These suspensions require continuous stirring to ensure effective contact of the titania and target species in addition to preventing catalyst settlement. Nano-sized TiO₂ suspension has been proven effective in killing various types of viruses, such as *poliovirus 1*, *hepatitis B virus*, Herpes simplex virus, and MS₂ bacteriophage.⁹⁹ Sonication of TiO₂ suspensions is considered an effective means for increasing the rate of bacterial destruction.¹⁰⁰⁻¹⁰² The use of ultrasound can produce more active sites on the catalytic surface for reaction with target species. The disadvantages of the suspension approach are that the slurry reduces UV light penetration and the catalyst powders need to be removed after treatment.

The use of TiO₂ films obviously overcomes the drawback of having to separate

the catalyst from water after treatment. Many studies have demonstrated that TiO₂ films coated on glass or tiles possess attractive properties, such as being deodorizing, antibacterial and self-cleaning under weak ultraviolet light in living areas.¹⁰³⁻¹¹²

TiO₂ only absorbs wavelengths in the near-UV region ($\lambda < 400$ nm), which is about 4 % of the solar spectrum. Visible-light-induced photocatalytic disinfection seems to be an attractive idea from the viewpoint of utilization the full spectrum of solar energy. Advances in materials design and fabrication at the nano-level make solar-driven photocatalytic disinfection systems possible. These systems can be mainly classified into three types: doped TiO₂, dye-sensitized TiO₂, and composite inorganic nanomaterials.

Doped TiO₂ with non-metallic species such as nitrogen, carbon and sulfur leads to a spectral shift towards the visible region.¹¹³⁻¹¹⁷ Our group reported that sulfur-doped TiO₂ exhibited bactericidal effects on *Micrococcus lylae* in water under visible-light irradiation. As shown in Fig. 1.4, the growth of *M. lylae* was effectively suppressed by the S-doped TiO₂ nanoparticles after an hour of visible-light irradiation. Neither pure TiO₂ nor S-doped TiO₂ in the dark showed any bactericidal effects on *M. lylae*, indicating that the photocatalyst itself was not toxic to *M. lylae*. The ESR results confirmed the generation of hydroxyl radicals from S-doped TiO₂ under visible-light irradiation.¹¹⁵ *Escherichia coli* inactivation by N, S co-doped commercial TiO₂

powders under visible-light was also reported.¹¹⁸ Besides, Shang et al reported an enhanced visible-light photocatalytic disinfection of bacterial spores by palladium-modified nitrogen-doped titanium oxide (TiON/PdO).¹¹⁹

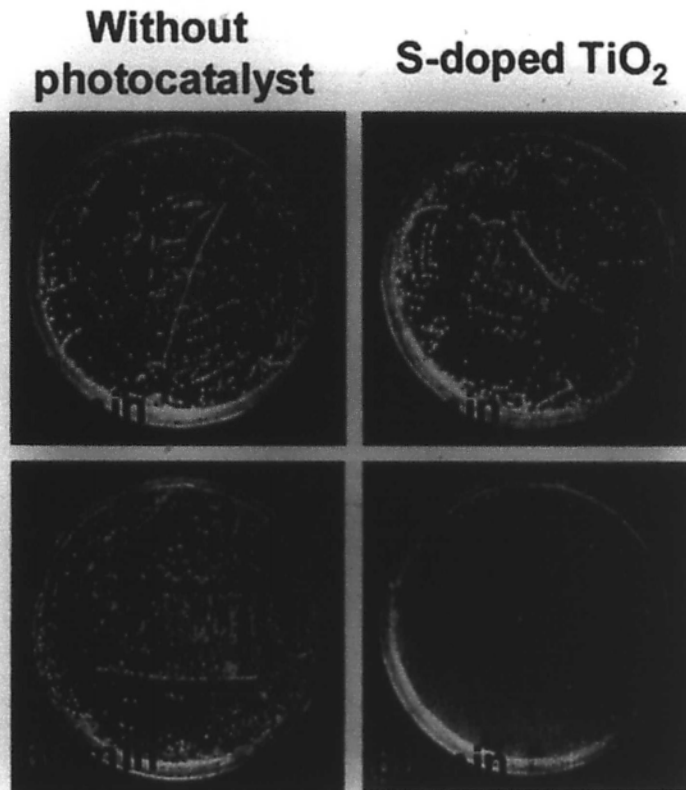


Figure. 1.4 Images of *M. lylae* colonies on an agar plate before and after visible light irradiation. Reproduced from Reference 115.

In the case of dye-sensitized TiO₂ for photocatalytic water disinfection, Yao et al. doped a novel photosensitive dye (5, 10, 15, 20-tetraphenyl-21*H*, 23*H*-porphine nickel, TPPN) into TiO₂ thin films by a sol-gel method. Such dye-sensitized TiO₂ thin film exhibited visible-light-induced bactericidal effects on phytopathogenic bacteria.¹²⁰ To date, dye-sensitization is still the most popular and economical processes for improving the visible-light performance of TiO₂ photocatalysts.

Composite TiO₂-based inorganic nanomaterials including Ag/AgBr/TiO₂¹²¹ and AgI/TiO₂¹²² were found to be effective in destroying *Escherichia coli*. A novel non-TiO₂ based Ag/AgBr/WO₃·H₂O visible-light photocatalyst was fabricated for bacteria destruction.¹²³ This system combined the advantages of a plasmon photocatalyst and a composite photocatalyst, showing high efficiency in the degradation of *Escherichia coli*. An interesting idea in designing new solar-driven photocatalytic disinfection systems is to maintain a certain level of bactericidal activity in the dark cycles. It was found that nitrogen-doped TiO₂ fibers containing highly dispersed palladium oxide nanoparticles (TiON/PdO) could maintain some of its catalytic disinfection capability even after shutting off the visible light source for hours.¹²⁴ This property was attributed to the optoelectronic coupling between PdO nanoparticles and the TiON semiconductor. It promoted charge carrier separation in TiON, resulting in the chemical reduction of PdO to Pd⁰. The “memory” antimicrobial effect came from the catalytic effect of Pd⁰. Another study on apatite-coated Ag/AgBr/TiO₂ photocatalyst also found inhibition of bacterial growth during the dark cycles.¹²⁵ These two studies open up new possibilities for a broad range of environmental applications.

1.2.5 Functional Materials for Treating Organic Pollutants

As recalcitrant organic pollutants continue to increase in air and wastewater streams, environmental laws and regulations become more stringent.¹²⁶ As a response, the development of newer eco-friendly methods of degrading these pollutants became an imperative task. Over the last 10 years, the scientific and engineering interest in the application of semiconductor photocatalysis has grown rapidly. Semiconductor photocatalysis with a primary focus on TiO_2 as a durable photocatalyst has been applied to a variety of problems of environmental interest in addition to water and air purification, owing to its low cost, strong oxidizing power, non-toxicity and long-term photostability.⁴⁶ Photocatalysts can promote reactions in the presence of light without being consumed in the overall reaction. The photocatalysts are inorganic semiconductors (e.g. TiO_2 , ZnO , Fe_2O_3 , CdS , WO_3 , and ZnS)¹²⁷⁻¹³² with band gap energies sufficient for catalyzing a wide range of chemical reactions. As shown in Fig. 1.5, these band gap energies and band gap positions of the semiconductor nanomaterials are of great importance for photocatalysis, because they indicate the thermal-dynamic limitations for the photoreactions that can take place.¹³³

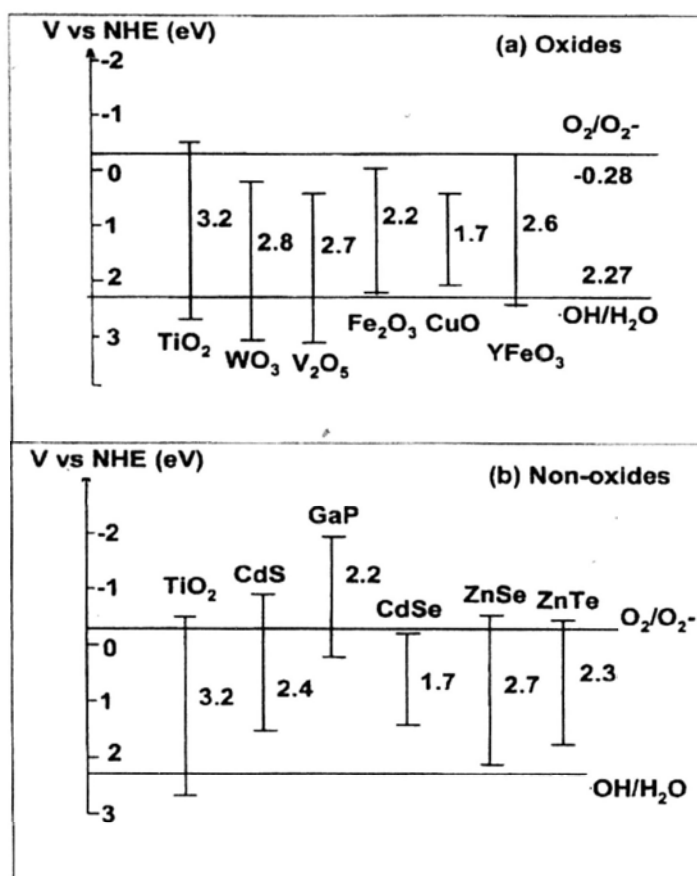


Figure 1.5 Band position of selective semiconductors and the redox potentials of O_2/O_2^- and $\cdot OH/H_2O$ redox couples at $pH = 7$, (a) oxide and (b) Non-oxide semiconductors.

Recently, various TiO_2 -based photocatalysts have been designed and fabricated via some special routes, such as template-free solvothermal method,^{127,134} ionothermal,^{135,136} and ionic-liquid microwave.¹³⁷ Li group adapted a template-free approach, in which a titania precursor, $TiOSO_4$, was solvothermally reacted in glycerol, alcohol, and ethyl ether, to fabricate the photocatalytic hollow anatase TiO_2 spheres with unique urchin-like morphology and tunable interior structure. The as-created sphere-in-sphere structure (as shown in Fig. 1.6) endows the spheres with greatly enhanced photocatalytic activity possibly attributed to multiple reflections of

UV light within the sphere interior voids.¹²⁷ Yu et al. used a one-step low-temperature hydrothermal approach without using any templates to synthesize hierarchical porous F-doped TiO₂ microspheres. The new photocatalysts show high visible light photocatalytic activity on the degradation of 4-chlorophenol.¹³⁴ The visible light photocatalytic activity of F-doped TiO₂ microspheres was achieved by the creation of oxygen vacancies rather than by the improvement of the absorption of bulk TiO₂ in visible light region.¹³⁴

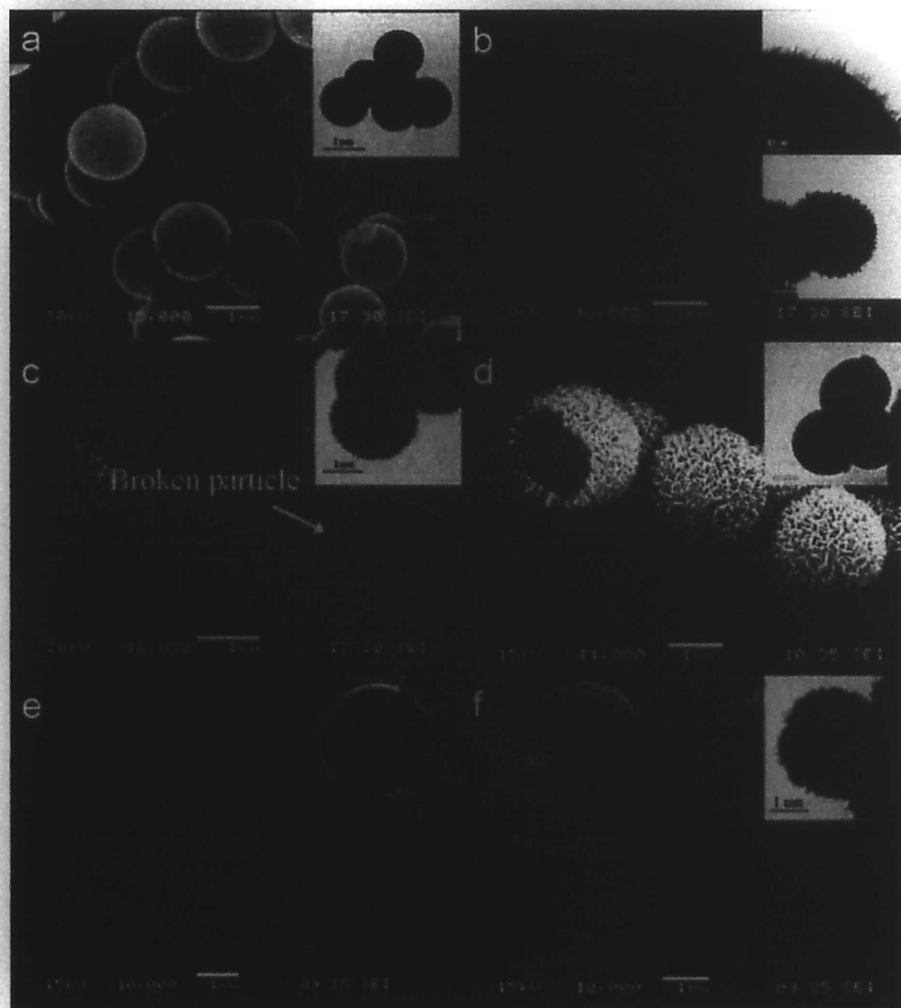


Figure 1.6 SEM and TEM (insets) images of the titania spheres synthesized for (a) 1/24, (b) 0.5, (c) 1, (d) 2, (e) 7, and (f) 14 days, showing transiting interior structure from dense, to sphere-in-sphere, to hollow and surface morphology from smooth to prickly. Reproduced from Reference 127.

Since Lu et al. reported the preparation of single crystal anatase TiO₂ sheets with 47 % reactive {001} facets,¹³⁸ several studies have extended this new route to synthesize TiO₂ sheets as candidates for photocatalysis applications.¹³⁹⁻¹⁴² Lu et al. further demonstrated a new solvothermal synthetic route for morphology-controlled preparation of high-quality anatase TiO₂ single crystals using 2-propanol as a synergistic capping agent and reaction medium together with HF. The synthesized TiO₂ nanocrystals had 64% {001} facets and displayed superior photoreactivity (more than 5 times) compared to P25 as a benchmarking material.¹³⁹ They also developed a facile and new route for one-pot synthesis of nitrogen doped {001} dominant anatase TiO₂ sheets. The as-prepared TiO₂ exhibited a significantly enhanced stability of high visible light absorption by bulk N doping and good photooxidation and photoreduction activity.¹⁴¹

1.2.6 Photocatalytic Materials for H₂ Evolution

Much research efforts have been devoted to the generation of hydrogen since this is the fuel with the highest energy capacity per unit mass. Hydrogen is also a clean energy carrier because it produces neither CO₂ nor pollutants. Many reviews on heterogeneous photocatalytic materials such as metal oxides, metal oxynitrides, metal oxysulfides, metal sulfides have been published.¹⁴³⁻¹⁴⁷ In this section, novel

polymeric photocatalysts for H₂ evolution are introduced. Besides, a “nonsacrificial” two-step water splitting system under monochromatic visible light irradiation is highlighted.

1.2.6.1 Polymeric Photocatalysts

Recently, a metal-free polymeric visible light driven photocatalyst for hydrogen production has been reported.¹⁴⁸ It was a graphitic carbon nitride (g-C₃N₄) synthesized via a thermal polycondensation of cyanamide. The photocatalyst produced H₂ from water containing triethanolamine as a sacrificial electron donor on light illumination ($\lambda > 420$ nm) in the absence of noble metal catalysts such as Pt. This is the first polymeric photocatalyst that is cheap and commonly available. It will open new way for the organic semiconductors as energy transducers.

However, the quantum yield of the above system (0.1 % at 420-460 nm) needs to be improved. Wang et al. advanced g-C₃N₄ by generating nanopore structure into the polymeric matrix to improve its structural and electronic functions for solar energy conversion.¹⁴⁹ The photocatalyst had a 3D porous framework, exhibiting an improved efficiency by ~ 1 order of magnitude. This example showed excellent artificial photosynthesis over mesoporous polymer semiconductors.

The ordered mesostructure permits structural orientation of guest molecules in the

periodic nanopores, which would enhance the selectivity and activity in photocatalysis.¹⁵⁰ Very recently, the photocatalytic activity of highly ordered porous g-C₃N₄ materials (as shown in Fig. 1.7) was evaluated by photochemical reduction of water in the presence of an electron donor with visible light.¹⁵¹ The total evolution of H₂ reached 2.1 mmol after 25 h visible light irradiation. The H₂ evolution on the order mesoporous C₃N₄ was about 5 times higher than that of bulk g-C₃N₄. Such structure is promising as a host semiconductor scaffold for the design of hybrid visible-light photocatalyst.

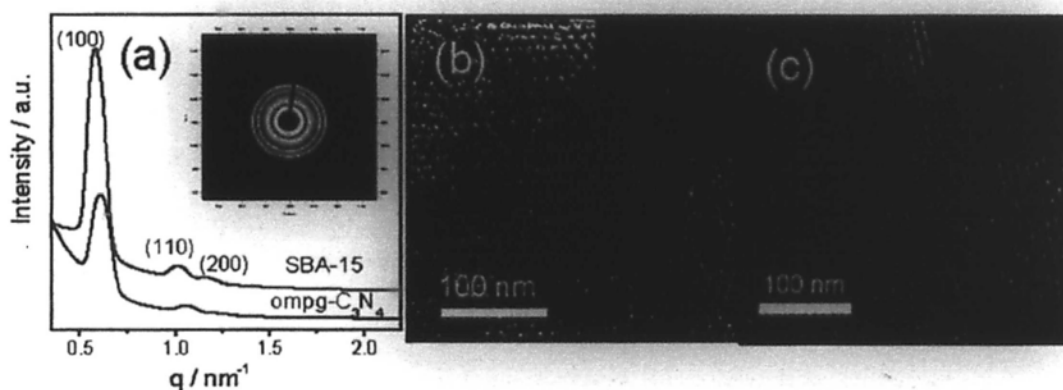


Figure 1.7 (a) SAXS patterns of ompg-C₃N₄ and SBA-15 template. The inset shows the corresponding 2D SAXS image of ompg-C₃N₄. (b, c) TEM images of g-C₃N₄. The inset in the TEM image shows the corresponding fast Fourier transforms of the patterns. Reproduced from Reference 151.

1.2.6.2 A “Nonsacrificial” Two-step Water Splitting System

Sacrificial reagents are often used to evaluate the photocatalytic activity for water splitting. From this point, the term of “water splitting” should be distinguishably used for H₂ or O₂ evolution from aqueous solutions in the presence of sacrificial

reagents. Water splitting means to split water into H_2 and O_2 in a stoichiometric amount in the absence of sacrificial reagents. Very recently, an efficient nonsacrificial water splitting system has been developed. It was a two-step photocatalytic water splitting (Z-scheme) system consisting of a modified $ZrO_2/TaON$ species (H_2 evolution photocatalyst), an O_2 evolution photocatalyst, and a reversible donor/acceptor pair (i.e., redox mediator). $Pt/ZrO_2/TaON$, Pt/WO_3 , and IO_3^-/I^- pairs were the most active components, because each photocatalyst efficiently promoted the forward reactions involving the redox couple (photooxidation of I^- on $Pt/ZrO_2/TaON$ and photoreduction of IO_3^- on Pt/WO_3).

1.2.7 Functional Materials for Valuable Hydrocarbons Evolution from CO_2

For solar-driven catalytic conversion of CO_2 to fuels to be practicable, highly efficient photocatalysts are required. Titanium dioxide (TiO_2) has been considered the most appropriate candidate as a photocatalyst due to its powerful oxidizing nature, superior charge transport properties, and corrosion resistance. Earlier studies, however, could only achieve low CO_2 conversion rates in spite of using UV illumination for band gap excitation. Recently, numerous studies on the preparation of solar-light-driven photocatalysts for hydrocarbon formation have been reported. They can be classified into two categories: TiO_2 based photocatalysts and composite

photocatalysts.

Metal doped TiO₂ catalyst sensitized with N3 dye was employed to photoreduce CO₂ with H₂O under concentrated natural sunlight to fuels in an optical-fiber photoreactor.¹⁵² A methane production rate of 0.617 μmol/(g h) was achieved on N3-dye-Cu(0.5 wt%)-Fe(0.5 wt%)/TiO₂ coated on optical fiber under an average solar light intensity of 20 mW/cm². The N3 dye could substantially improve the photoactivity of Cu(0.5 wt%)-Fe(0.5 wt%)/TiO₂ catalyst towards methane production under concentrated natural sunlight due to its full visible light adsorption. The photocatalyst was stable up to 6 h.

Recently, N-doped TiO₂ nanotubes with copper and platinum nanoparticles loaded onto the surfaces were developed to realize efficient solar conversion of carbon dioxide and water vapor to methane and other hydrocarbons.¹⁵³ The experiments were conducted in outdoor sunlight at University Park, PA. Using outdoor global AM 1.5 sunlight, 100 mW/cm², a hydrocarbon production rate of 111 ppm cm⁻² h⁻¹, or ≈160 μL/(g h), was obtained when the nanotube array samples were loaded with both 52 % Cu and 48 % Pt nanoparticles. The authors pointed out that the efficiency of the catalyst was still quite low, but they were optimistic that future work could improve it.

Carbon dioxide could be reduced with water to organic compounds over a hybrid

catalyst under concentrated sunlight.¹⁵⁴ The catalyst used was a Pt-loaded $\text{K}_2\text{Ti}_6\text{O}_{13}$ coupled with a Fe-based catalyst supported on a dealuminated Y-type zeolite (Fe-Cu-K/DAY). The Pt/ $\text{K}_2\text{Ti}_6\text{O}_{13}$ catalyst decomposed water to produce H_2 and the Fe-Cu-K/DAY catalyst reduced CO_2 with the resulting H_2 into organic compounds such as CH_4 , HCOOH , HCHO , CH_3OH , and $\text{C}_2\text{H}_5\text{OH}$. The Pt/ $\text{K}_2\text{Ti}_6\text{O}_{13}$ catalysts could be combined with another CO_2 hydrogenation catalyst of Cu/ZnO.¹⁵⁵ The generation of CH_3OH over this composite photocatalyst under concentrated sunlight means successful photocatalytic conversion carbon dioxide to fuels. These studies suggest that sunlight driven photocatalytic processes have the potential for organic compound evolution from CO_2 and water.

Recently, a NiO/InTaO₄ photocatalyst with a band gap of 2.6 eV has been developed by Chen's Group.¹⁵⁶ The NiO cocatalyst was loaded by incipient-wetness impregnation with aqueous solution of $\text{Ni}(\text{NO}_3)_2$. The product was calcined at 350 °C for 1 h in air, and then pretreated by H_2 reduction at 500 °C for 2 h and subsequent O_2 oxidation at 200 °C for 1 h. This catalyst was able to reduce CO_2 to methanol under visible light illumination. A 1.0 wt.% NiO-InTaO₄ photocatalyst in 0.2 M KHCO_3 gave the highest activity (1.394 $\mu\text{mol}/(\text{h}\cdot\text{g})$). The reduction-oxidation pretreatment had a positive effect on the activity of the catalyst.

CdSe quantum dot (QD)-sensitized TiO_2 heterostructures have been fabricated for

the photocatalytic reduction of CO₂ in the presence of H₂O.¹⁵⁷ These heterostructured materials were capable of catalyzing the photoreduction of CO₂ using visible light illumination ($\lambda > 420$ nm) only. Typical yields of the gas-phase products after visible light illumination ($\lambda > 420$ nm) were 48 ppm g⁻¹ h⁻¹ of CH₄, 3.3 ppm g⁻¹ h⁻¹ of CH₃OH (vapor), and trace amounts of CO and H₂.

1.3 Synthesis of Nanomaterials

1.3.1 Preparation Methods

Nanoparticles can be synthesized by coprecipitation, sol-gel processing, microemulsions, hydrothermal/solvothermal methods, templated syntheses, biomimetic syntheses and microwave synthesis.¹⁵⁸ Herein, we will focus on the discussion of solvothermal processing and microwave synthesis.

1.3.2 Solvothermal Processing

In a sealed vessel (bomb, autoclave, etc.), solvents can be brought to temperatures well above their boiling points by the increase in autogenous pressures resulting from heating. Performing a chemical reaction under such conditions is referred to as solvothermal processing.¹⁵⁸ Some solvothermal processes indeed involve supercritical solvents. However, most take advantage of the increased solubility and

reactivity of metal salts and complexes without bringing the solvents to its critical. Therefore, the solvothermal processing allows many inorganic materials to be prepared at relatively lower temperature than that required by the traditional solid-state reactions. Furthermore, the resulted products are often well crystallized and do not require postannealing treatment.

Despite these advantages, solvothermal synthesis still suffers from time-consuming process and complex devices. Under the conditions of solvothermal synthesis, the pressure can be very high in the reaction system. Therefore, a pressure-resistant vessel such as a metal autoclave is needed. As a matter of safety, the pressures generated in a sealed vessel should be estimated beforehand. Besides, unique synthesis techniques are highly demanded to improve the reaction efficiency and shorten the reaction time.

1.3.3 Microwave Synthesis

1.3.3.1 Background

High-speed synthesis with microwaves has attracted a considerable amount of attention in recent years. Microwaves are the part of the electromagnetic radiation spectrum in the approximate frequency range 0.3 to 300 GHz. with corresponding wavelengths ranging from 1 m to 1 mm in air. Microwave-enhanced chemistry is

based on the efficient heating of materials by “microwave dielectric heating” effects.¹⁵⁹ This phenomenon is dependent on the ability of a specific material (solvent or reagent) to absorb microwave energy and convert it into heat. The electric component of an electromagnetic field causes heating by two main mechanisms: dipolar polarization and ionic conduction. Irradiation of the sample at microwave frequencies results in the dipoles or ions aligning in the applied electric field. As the applied field oscillates, the dipole or ion field attempts to realign itself with the alternating electric field and, in the process, energy is lost in the form of heat through molecular friction and dielectric loss. It is now well known that microwaves generate an inverse temperature profile during heating. The centre of a body will become hotter than its surface. This can result the morphology of the product completely different from that resulting from conventional method.

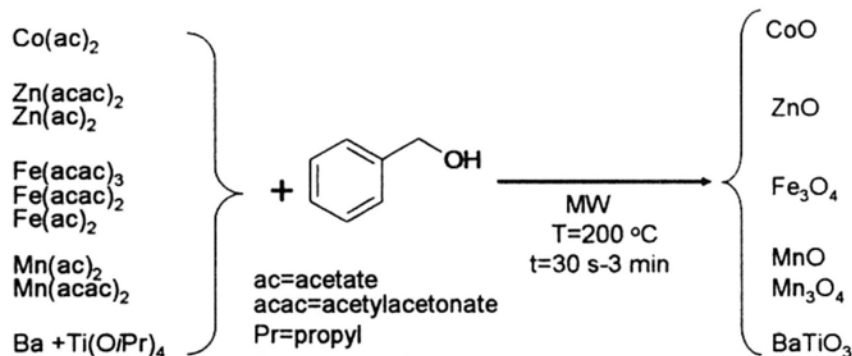
1.3.3.2 Literature Survey

This section highlights recent publications of materials fabricated by controlled microwave heating technology.

- **Nanoparticles**

Highly crystalline metal oxide nanoparticles such as CoO, ZnO, Fe₃O₄, MnO, Mn₃O₄, and BaTiO₃ were synthesized (shown in Scheme 1.1) in just a few minutes

by reacting metal alkoxides, acetates or acetylacetonates with benzyl alcohol under microwave heating.¹⁶⁰ The pronounced dependence of the crystallite size on the heating time (which was not found in analogous solvothermal experiments in the autoclave¹⁶¹⁻¹⁶³) provided a precious tool to tailor this parameter. Microwave irradiation can be used as a powerful tool to accelerate the formation of metal oxide nanoparticles through directly influencing the organic reaction pathways. A simple and rapid microwave-assisted wet chemical route was developed for the preparation of Sb_2Te_3 hexagonal single-crystalline nanoplates with edge length of hundreds of nanometers.¹⁶⁴



Scheme 1.1 General reaction scheme displaying the metal oxide precursors used, the solvent, the experimental conditions, and the resulting metal oxide nanoparticles. Reproduced from Reference 160.

Anatase nanocrystals with uniform size and shape were synthesized via a microwave-assisted route in ionic liquid.¹³⁷ This reaction involved 1-butyl-3-methylimidazolium tetrafluoroborate as the solvent and titanium isopropoxide as the precursor. This process is fast and simple. The reaction could be

performed under atmospheric pressure in a domestic microwave oven. No high-pressure and high temperature apparatus is needed. The size of nanoparticles could be easily controlled.

- Micrometer-sized crystals

A simple microwave irradiation method for the large-scale synthesis of submicrometer-sized TiO_2 rods at normal atmospheric pressure was demonstrated.¹⁶⁵

It was emphasized that only 1-3 min of microwave irradiation was adequate for the reaction of tetra-isopropyl orthotitanate with ethylene glycol to produce rods of titanium glycolate with diameters of $\sim 0.4 \mu\text{m}$ and lengths up to $5 \mu\text{m}$. The as-formed titanium glycolate rods, followed by calcination under air for 2 h, fabricated anatase (500°C) and rutile (900°C) titania without changing their rod-shaped morphology. A mechanism based on microwave superheating phenomena was presented.¹⁶⁵

Micro-sized decaoctahedron BaZrO_3 powders were synthesized by means of a hydrothermal microwave method at 140°C for 40 min.¹⁶⁶ This is the first synthesis of microcrystalline BaZrO_3 powders presenting a decaoctahedron shape.

- Porous materials

The currently available microwave technology permits the development and implementation of a temperature-programmed microwave-assisted synthesis of ordered mesoporous silicas (OMSs).¹⁶⁷ SBA-15 samples were obtained in as little as

3 h at higher temperatures (such as 160, 180, and even 200 °C). They showed better thermal stability than those synthesized at commonly used temperatures (< 150 °C). This simple process significantly reduced the time of synthesis from days to hours. The adsorption and structural properties could be tailored by this temperature-programmed microwave-assisted approach.

A series of aluminophosphate molecular sieves were synthesized by the microwave-assisted ionothermal approach.¹⁶⁸ In hydrothermal synthesis of molecular sieves, a pressure-resistant vessel such as a metal autoclave would be needed, but this was not suitable for microwave dielectric heating. Therefore, Teflon and other microwave-transparent polymers were widely used to make autoclaves for microwave heating. However, these materials became flexible at high temperatures and could not withstand the high pressure. The use of an ionic liquid such as 1-ethyl-3-methylimidazolium bromide ([emim]Br) addressed this problem, since it had negligible vapor pressure and high stability at 150 °C or even higher temperatures. Therefore, ionic liquids are the ideal solvent for the safe synthesis of molecular sieves by microwave irradiation.

1.3.3.3 Summary and Outlook

The examples provided in Section 1.3.3.2 should make it clear that many types of inorganic materials can be fabricated under microwave conditions. Dramatic rate enhancements were observed in all cases. The simple convenience of using microwave technology will make this nonclassical heating method a standard tool in the laboratory within a few years. Using sealed-vessel systems, the benefits of controlled microwave heating are manifold:

- Microwave processing can dramatically reduce reaction time. It also can provide higher yields and cleaner reaction profiles. In many cases the observed rate enhancements may be simply a consequence of the high reaction temperatures that can rapidly be obtained by using this nonclassical heating method. In addition, many enhancements result from the involvement of so-called specific or non-thermal microwave effects.
- The choice of solvent for a given reaction is determined by dielectric properties of the reaction medium. This property can be easily tuned by, for example, addition of polar materials such as ionic liquids.
- The modern microwave reactors allow for an excellent control of reaction parameters by monitoring the temperature and pressure. This generally leads to more reproducible reaction conditions.

- The overall process is more energy efficient than classical oil-bath heating since direct “in-core” heating of the medium occurs.

1.4 Summary

This chapter gave a brief introduction on the classification of functional material, the applications of functional material and the preparation methods. Functional materials fabricated by microwave-assisted method were fully discussed. The benefits of controlled microwave heating were highlighted.

1.5 Aim of This Research and Its Significance

The aim of this thesis work is to design safe and energy-saving approaches to fabricate functional materials with tunable sizes and controllable morphologies. These materials are expected to have promising applications in photocatalysis and magnetically driven applications.

A fast and energy saving method was developed to fabricate well crystallized Ni particles with continuously tunable sizes by a simple reaction involving nickel acetate tetrahydrate and hexadecylamine. This was much easier than the methods reported in the literature that require multi-stabilizers to control the size and morphology of magnetic nanoparticles. Our simple process was therefore less prone

to contamination and it ensured high-purity products. Another advantage of this method was that the reaction proceeded at atmospheric pressure in the absence of protective gas (e.g. Ar or N₂) without stirring or refluxing. This was an improvement over the solvothermal method in which high pressure and high temperature were involved.

Furthermore, an energy-saving solvothermal method for fabricating 3D bismuth oxyhalides was developed involving an imidazolium-based ionic liquid as the reagent. The reaction time was only 1 hr. This was the first example of ternary compound mesocrystal grown from ionic liquids. The key in this method was the use of the imidazolium-based ionic liquid which formed an ionic-liquid-bismuth complex. It evolved into the final 3D superstructure. By selecting an appropriate anion for the ionic liquid, bismuth oxybromide and oxychloride could be synthesized.

Additionally, TiO₂ mesocrystals with controllable morphologies were fabricated via the microwave-assisted hydrothermal method. These materials included anatase TiO₂ single crystals with tunable percentage of reactive {001} facets and 3D rutile TiO₂ mesocrystals. These TiO₂-based mesocrystals exhibited excellent photocatalytic activities in the degradation of 4-chlorophenol and the oxidation of nitric oxide.

1.6 References

- [1] Peng, Z. A.; Peng, X. G. *J. Am. Chem. Soc.* **2001**, *123*, 183.
- [2] Tanori, J.; Pileni, M. P. *Langmuir* **1997**, *13*, 639.
- [3] Vaidya, S.; Ahmed, J.; Ganguli, A. K. *Defence Sci. J.* **2008**, *58*, 531.
- [4] Kim, J. S.; Youk, J. H. *Macro. Res.* **2009**, *17*, 926.
- [5] Lee, S.; Cho, I. S.; Lee, J. H.; Kim, D. H.; Kim, D. W.; Kim, J. Y.; Shin, H.; Lee, J. K.; Jung, H. S.; Park, N. G.; Kim, K.; Ko, M. J.; Hong, K. S. *Chem. Mater.* **2010**, *22*, 1958.
- [6] Yajima, S.; Nakajima, T.; Higashi, M.; Kimura, K. *Chem. Commun.* **2010**, 1914.
- [7] Levin, D.; Soled, S. L.; Ying, J. Y. *Inorg. Chem.* **1996**, *35*, 4191.
- [8] Wang, W.; Qiao, X. L.; Chen, J. G. *J. Am. Ceram. Soc.* **2008**, *91*, 1697.
- [9] Takami, S.; Hayakawa, R.; Wakayama, Y.; Chikyow, T. *Nanotechnology* **2010**, *21*, 134009.
- [10] Wu, X. S.; Kawi, S. *Cryst. Growth. Des.* **2010**, *10*, 1833.
- [11] Tian, Y. M.; Zhao, X.; Shen, L. C.; Meng, F. Y.; Tang, L. Q.; Deng, Y. H.; Wang, Z. C. *Mater. Lett.* **2006**, *60*, 527.
- [12] Beguin, F.; Szostak, K.; Lota, G.; Frackowiak, E. *Adv. Mater.* **2005**, *17*, 2380.
- [13] Schneider, S.; Yang, Y.; Marks, T. J. *Chem. Mater.* **2005**, *17*, 4286.
- [14] Huang, Y.; Ai, Z. H.; Ho, W. K.; Chen, M. J.; Lee, S. *J. Phys. Chem. C* **2010**,

114, 6342.

- [15] Shin, K.; Il Seok, S.; Im, S. H.; Park, J. H. *Chem. Commun.* **2010**, 2385.
- [16] Zeng, X. H.; Pogrebnyakov, A. V.; Zhu, M. H.; Jones, J. E.; Xi, X. X.; Xu, S. Y.; Wertz, E.; Li, Q.; Redwing, J. M.; Lettieri, J.; Vaithyanathan, V.; Schlom, D. G.; Liu, Z. K.; Trithaveesak, O.; Schubert, J. *Appl. Phys. Lett.* **2003**, 82, 2097.
- [17] Hirai, Y.; Yabu, H.; Matsuo, Y.; Ijio, K.; Shimomura, M. *Chem. Commun.* **2010**, 2298.
- [18] Adschiri, T.; Takami, S.; Umetsu, M.; Ohara, S.; Tsukada, T. *Ceram. Trans.* **2005**, 146, 3.
- [19] Shivakumara, C.; Bellakki, M. B. *Bull. Mater. Sci.* **2009**, 32, 443.
- [20] Rao, G. R.; Mishra, B. G.; Sahu, H. R. *Mater. Lett.* **2004**, 58, 3523.
- [21] Alivisatos, A. P. *NATO Sci. Ser., Ser. C* **1999**, 519, 405.
- [22] Trindade, T.; O'Brien, P.; Pickett, N. L. *Chem. Mater.* **2001**, 13, 3843.
- [23] Kwon, K. W.; Lee, B. H.; Shim, M. *Chem. Mater.* **2006**, 18, 6357.
- [24] Meuer, S.; Oberle, P.; Theato, P.; Tremel, W.; Zentel, R. *Adv. Mater.* **2007**, 19, 2073
- [25] Ou, Y. N.; Li, G. R.; Wang, Z. L.; Yu, X. L.; Tong, Y. X. *J. Electrochem. Soc.* **2010**, 157, D264.
- [26] Pan, M. H.; Liu, H.; Wang, J. Z.; Jia, J. F.; Xue, Q. K.; Li, J. L.; Qin, S.;

- Mirsaidov, U. M.; Wang, X. R.; Markert, J. T.; Zhang, Z. Y.; Shih, C. K. *Nano Lett.* **2005**, *5*, 87.
- [27] Elias, J.; Tena-Zaera, R.; Wang, G. Y.; Levy-Clement, C. *Chem. Mater.* **2008**, *20*, 6633.
- [28] Lin, H. H.; Wang, C. Y.; Shih, H. C.; Chen, J. M.; Hsieh, C. T. *J. Appl. Phys.* **2004**, *95*, 5889.
- [29] Tao, C. G.; Cullen, W. G.; Williams, E. D.; Hunyadi, S. E.; Murphy, C. J. *Surf. Sci.* **2007**, *601*, 4939.
- [30] Song, K.; Guan, J. Q.; Wu, S. J.; Kan, Q. B. *Catal. Commun.* **2009**, *10*, 631.
- [31] Vallance, S. R.; Round, D. M.; Ritter, C.; Cussen, E. J.; Kingman, S.; Gregory, D. H. *Adv. Mater.* **2009**, *21*, 4502.
- [32] Silva, G. W. C.; Yeaman, C. B.; Ma, L. Z.; Cerefice, G. S.; Czerwinski, K. R.; Sattelberger, A. P. *Chem. Mater.* **2008**, *20*, 3076.
- [33] Pillay, D.; Wang, Y.; Hwang, G. S. *J. Am. Chem. Soc.* **2006**, *128*, 14000.
- [34] Kher, S. S.; Romero, J. V.; Caruso, J. D.; Spencer, J. T. *Appl. Organomet. Chem.* **2008**, *22*, 300.
- [35] Silveira, C. C.; Santos, P. C. S.; Mendes, S. R.; Braga, A. L. *J. Org. Chem.* **2008**, *693*, 3787.
- [36] Pore, V.; Hatanpaa, T.; Ritala, M.; Leskela, M. *J. Am. Chem. Soc.* **2009**, *131*,

- 3478.
- [37] Gramp, J. P.; Bigham, J. M.; Jones, F. S.; Tuovinen, O. H. *J. Hazard. Mater.* **2010**, *175*, 1062.
- [38] Bi, Y. P.; Ye, J. H. *Chem. Commun.* **2010**, 1532.
- [39] He, Y.; Jiang, Y.; Xu, N. P.; Zou, J.; Huang, B. Y.; Liu, C. T.; Liaw, P. K. *Adv. Mater.* **2007**, *19*, 2102.
- [40] Aleandri, L. E.; Bogdanovic, B.; Durr, C.; Jones, D. J.; Roziere, J.; Wilczok, U. *Adv. Mater.* **1996**, *8*, 600.
- [41] Kumai, Y.; Tsukada, H.; Akimoto, Y.; Sugimoto, N.; Seno, Y.; Fukuoka, A. T.; Ichikawa, M.; Inagaki, S. *Adv. Mater.* **2006**, *18*, 760.
- [42] Wood, C. D.; Tan, B.; Trewin, A.; Su, F.; Rosseinsky, M. J.; Bradshaw, D.; Sun, Y.; Zhou, L.; Cooper, A. I. *Adv. Mater.* **2008**, *20*, 1916.
- [43] Novak, B. M. *Adv. Mater.* **1993**, *5*, 422.
- [44] Kamtekar, K. T.; Monkman, A. P.; Bryce, M. R. *Adv. Mater.* **2010**, *22*, 572.
- [45] Sculimbrene, B. R.; Imperiali, B. *J. Am. Chem. Soc.* **2006**, *128*, 7346.
- [46] Gaya, U. I.; Abdullah, A. H. *J. Photoch. Photobio. C-Photochem. Rev.* **2008**, *9*, 1.
- [47] Alivisatos, A. P.; Gu, W. W.; Larabell, C. *Annu. Rev. Biomed. Eng.* **2005**, *7*, 55.
- [48] Cheon, J.; Lee, J. H. *Acc. Chem. Res.* **2008**, *41*, 1630.

- [49] Laurent, S.; Forge, D.; Port, M.; Roch, A.; Robic, C.; Elst, L. V.; Muller, R. N. *Chem. Rev.* **2008**, *108*, 2064.
- [50] Talapin, D. V.; Lee, J. S.; Kovalenko, M. V.; Shevchenko, E. V. *Chem. Rev.* **2010**, *110*, 389.
- [51] Song, R. Q.; Cölfen, H. *Adv. Mater.* **2010**, *22*, 1301.
- [52] Wang, T. X.; Cölfen, H.; Antonietti, M. *J. Am. Chem. Soc.* **2005**, *127*, 3246.
- [53] Li, H. Y.; Estroff, L. A. *Crystengcomm* **2007**, *9*, 1153.
- [54] Li, Z. H.; Gessner, A.; Richters, J. P.; Kalden, J.; Voss, T.; Kubel, C.; Taubert, A. *Adv. Mater.* **2008**, *20*, 1279.
- [55] Polleux, J.; Pinna, N.; Antonietti, M.; Niederberger, M. *J. Am. Chem. Soc.* **2005**, *127*, 15595.
- [56] Oaki, Y.; Imai, H. *J. Mater. Chem.* **2007**, *17*, 316.
- [57] Yang, S. W.; Gao, L. *J. Am. Chem. Soc.* **2006**, *128*, 9330.
- [58] Ge, J. P.; Hu, Y. X.; Biasini, M.; Beyermann, W. P.; Yin, Y. D. *Angew. Chem. Int. Ed.* **2007**, *46*, 4342.
- [59] Zhang, D. Q.; Li, G. S.; Wang, F.; Yu, J. C. *CrystEngComm* **2010**, DOI: 10.1039/b922477g.
- [60] Zhou, L.; Wang, W. Z.; Xu, H. L. *Cryst. Growth Des.* **2008**, *8*, 728.
- [61] Liu, S. W.; Yu, J. G. *J. Solid State Chem.* **2008**, *181*, 1048.

- [62] Gong, Q.; Qian, X. F.; Ma, X. D.; Zhu, Z. K. *Cryst. Growth Des.* **2006**, *6*, 1821.
- [63] Calderone, V. R.; Testino, A.; Buscaglia, M. T.; Bassoli, M.; Bottino, C.; Viviani, M.; Buscaglia, V.; Nanni, P. *Chem. Mater.* **2006**, *18*, 1627.
- [64] Rorvik, P. M.; Almli, A.; van Helvoort, A. T. J.; Holmestad, R.; Tybell, T.; Grande, T.; Einarsrud, M. A. *Nanotechnology* **2008**, *19*, 225605.
- [65] Zhang, C.; Chen, J.; Zhou, Y. C.; Li, D. Q. *J Phys. Chem. C* **2008**, *112*, 10083.
- [66] Yang, C. S.; Chen, C. J.; Lin, X. H. *New J. Chem.* **2007**, *31*, 363.
- [67] Carbone, L.; Nobile, C.; De Giorgi, M.; Sala, F. D.; Morello, G.; Pompa, P.; Hytch, M.; Snoeck, E.; Fiore, A.; Franchini, I. R.; Nadasan, M.; Silvestre, A. F.; Chiodo, L.; Kudera, S.; Cingolani, R.; Krahne, R.; Manna, L. *Nano Lett.* **2007**, *7*, 2942.
- [68] Rycenga, M.; McLellan, J. M.; Xia, Y. *Adv. Mater.* **2008**, *20*, 2416.
- [69] Wang, N.; Cao, X.; Guo, L.; Yang, S. H.; Wu, Z. Y. *Acs Nano* **2008**, *2*, 184.
- [70] Meldrum, F. C.; Colfen, H. *Chem. Rev.* **2008**, *108*, 4332.
- [71] Poizot, P.; Laruelle, S.; Grugeon, S.; Dupont, L.; Tarascon, J. M. *Nature* **2000**, *407*, 496.
- [72] Arico, A. S.; Bruce, P.; Scrosati, B.; Tarascon, J. M.; Van Schalkwijk, W. *Nat. Mater.* **2005**, *4*, 366.
- [73] Bruce, P. G.; Scrosati, B.; Tarascon, J. M. *Angew. Chem. Int. Ed.* **2008**, *47*, 2930.

- [74] Jiao, F.; Shaju, K. M.; Bruce, P. G. *Angew. Chem. Int. Ed.* **2005**, *44*, 6550.
- [75] Jiao, F.; Bruce, P. G. *Adv. Mater.* **2007**, *19*, 657.
- [76] Hu, X. L.; Li, G. S.; Yu, J. C. *Langmuir* **2010**, *26*, 3031.
- [77] Huang, X. J.; Meng, F. L.; Pi, Z. X.; Xu, W. H.; Liu, J. H. *Sensor. Actuat. B-Chem* **2004**, *99*, 444.
- [78] Varghese, O. K.; Gong, D. W.; Paulose, M.; Ong, K. G.; Grimes, C. A. *Sensor. Actuat. B-Chem* **2003**, *93*, 338.
- [79] Chen, H. M.; Zhao, Y. Q.; Yang, M. Q.; He, J. H.; Chu, P. K.; Zhang, J.; Wu, S. H. *Anal. Chim. Acta* **2010**, *659*, 266.
- [80] Zheng, W.; Li, Z. Y.; Zhang, H. N.; Wang, W.; Wang, Y.; Wang, C. *Mater. Res. Bull.* **2009**, *44*, 1432.
- [81] Zhang, D. J.; Sun, H.; Liu, J. Q.; Liut, C. B. *J. Phys. Chem. C* **2009**, *113*, 21.
- [82] Sun, Z. Y.; Yuan, H. Q.; Liu, Z. M.; Han, B. X.; Zhang, X. R. *Adv. Mater.* **2005**, *17*, 2993.
- [83] Yin, X. M.; Li, C. C.; Zhang, M.; Hao, Q. Y.; Liu, S.; Li, Q. H.; Chen, L. B.; Wang, T. H. *Nanotechnology* **2009**, *20*, 455503.
- [84] Du, N.; Zhang, H.; Ma, X. Y.; Yang, D. *Chem. Commun.* **2008**, 6182.
- [85] Ma, Z. Y.; Dosev, D.; Nichkova, M.; Gee, S. J.; Hammock, B. D.; Kennedy, I. *M. J. Mater. Chem.* **2009**, *19*, 4695.

- [86] Corr, S. A.; O' Byrne, A.; Gun'ko, Y. K.; Ghosh, S.; Brougham, D. F.; Mitchell, S.; Volkov, Y.; Prina-Mello, A. *Chem. Commun.* **2006**, 4474.
- [87] Yoon, T. J.; Kim, J. S.; Kim, B. G.; Yu, K. N.; Cho, M. H.; Lee, J. K. *Angew. Chem. Int. Ed.* **2005**, *44*, 1068.
- [88] Wu, J.; Ye, Z. Q.; Wang, G. L.; Yuan, J. L. *Talanta* **2007**, *72*, 1693.
- [89] Veiseh, O.; Sun, C.; Gunn, J.; Kohler, N.; Gabikian, P.; Lee, D.; Bhattarai, N.; Ellenbogen, R.; Sze, R.; Hallahan, A.; Olson, J.; Zhang, M. Q. *Nano Lett.* **2005**, *5*, 1003.
- [90] Huh, Y. M.; Jun, Y. W.; Song, H. T.; Kim, S.; Choi, J. S.; Lee, J. H.; Yoon, S.; Kim, K. S.; Shin, J. S.; Suh, J. S.; Cheon, J. *J. Am. Chem. Soc.* **2005**, *127*, 12387.
- [91] Yoon, T. J.; Yu, K. N.; Kim, E.; Kim, J. S.; Kim, B. G.; Yun, S. H.; Sohn, B. H.; Cho, M. H.; Lee, J. K.; Park, S. B. *Small* **2006**, *2*, 209.
- [92] Becker, C.; Hodenius, M.; Blendinger, G.; Sechi, A.; Hieronymus, T.; Muller-Schulte, D.; Schmitz-Rode, T.; Zenke, M. *J. Magn. Magn. Mater.* **2007**, *311*, 234.
- [93] Hong, X.; Li, J.; Wang, M. J.; Xu, J. J.; Guo, W.; Li, J. H.; Bai, Y. B.; Li, T. J. *Chem. Mater.* **2004**, *16*, 4022.
- [94] Gao, J. H.; Zhang, B.; Gao, Y.; Pan, Y.; Zhang, X. X.; Xu, B. *J. Am. Chem. Soc.*

2007, 129, 11928.

[95] Yi, D. K.; Selvan, S. T.; Lee, S. S.; Papaefthymiou, G. C.; Kundaliya, D.; Ying, J.

Y. J. Am. Chem. Soc. **2005**, 127, 4990.

[96] Zhao, Y. W.; Zhang, X. K.; Xiao, J. Q. *Adv. Mater.* **2005**, 17, 915.

[97] Kim, J.; Kim, H. S.; Lee, N.; Kim, T.; Kim, H.; Yu, T.; Song, I. C.; Moon, W. K.;

Hyeon, T. *Angew. Chem. Int. Ed.* **2008**, 47, 8438.

[98] Matsunaga, T.; Tomoda, R.; Nakajima, T.; Wake, H. *FEMS Microbiol. Lett.*

1985, 29, 211.

[99] Li, Q. L.; Mahendra, S.; Lyon, D. Y.; Brunet, L.; Liga, M. V.; Li, D.; Alvarez, P.

J. J. Water Res. **2008**, 42, 4591.

[100] Ibanez, J. A.; Litter, M. I.; Pizarro, R. A. *J. Photoch. Photobio A-Chem.* **2003**,

157, 81.

[101] Watts, R. J.; Kong, S. H.; Orr, M. P.; Miller, G. C.; Henry, B. E. *Water Res.*

1995, 29, 95.

[102] Li, X. Z.; Zhang, M.; Chua, H. *Water Sci. Technol.* **1996**, 33, 111.

[103] Goswami, D. Y.; Trivedi, D. M.; Block, S. S. *J. Solar Energ.-T Asme* **1997**, 119,

92.

[104] Sunada, K.; Kikuchi, Y.; Hashimoto, K.; Fujishima, A. *Environ. Sci. Technol.*

1998, 32, 726.

- [105]Hur, J. S.; Koh, Y. J. *Biotechnol. Lett.* **2002**, *24*, 23.
- [106]Wang, R.; Hashimoto, K.; Fujishima, A.; Chikuni, M.; Kojima, E.; Kitamura, A.; Shimohigoshi, M.; Watanabe, T. *Nature* **1997**, *388*, 431.
- [107]Sakai, N.; Wang, R.; Fujishima, A.; Watanabe, T.; Hashimoto, K. *Langmuir* **1998**, *14*, 5918.
- [108]Watanabe, T.; Nakajima, A.; Wang, R.; Minabe, M.; Koizumi, S.; Fujishima, A.; Hashimoto, K. In *2nd International Conference on Coating on Glass [ICCG]* Saarbrucken, Germany, 1998, 260.
- [109]Sakai, N.; Fujishima, A.; Watanabe, T.; Hashimoto, K. *J. Phys. Chem. B* **2001**, *105*, 3023.
- [110]Miyauchi, M.; Nakajima, A.; Fujishima, A.; Hashimoto, K.; Watanabe, T. *Chem. Mater.* **2000**, *12*, 3.
- [111]Lee, H. Y.; Park, Y. H.; Ko, K. H. *Langmuir* **2000**, *16*, 7289.
- [112]Sun, R. D.; Nakajima, A.; Fujishima, A.; Watanabe, T.; Hashimoto, K. *J. Phys. Chem. B* **2001**, *105*, 1984.
- [113]Sakthivel, S.; Janczarek, M.; Kisch, H. *J. Phys. Chem. B* **2004**, *108*, 19384.
- [114]Miyauchi, M.; Ikezawa, A.; Tobimatsu, H.; Irie, H.; Hashimoto, K. *Phys. Chem. Chem. Phys.* **2004**, *6*, 865.
- [115]Yu, J. C.; Ho, W. K.; Yu, J. G.; Yip, H.; Wong, P. K.; Zhao, J. C. *Environ. Sci.*

Technol. **2005**, *39*, 1175.

[116]Li, G. S.; Yu, J. C.; Zhang, D. Q.; Hu, X. L.; Lau, W. M. *Sep. Purif. Technol.*

2009, *67*, 152.

[117]Huo, Y. N.; Bian, Z. F.; Zhang, X. Y.; Jin, Y.; Zhu, J.; Li, H. X. *J. Phys. Chem.*

C **2008**, *112*, 6546.

[118]Rengifo-Herrera, J. A.; Mielczarski, E.; Mielczarski, J.; Castillo, N. C.; Kiwi, J.;

Pulgarin, C. *Appl Catal B-Environ* **2008**, *84*, 448.

[119]Wu, P. G.; Xie, R. C.; Shang, J. K. *J. Am. Ceram. Soc.* **2008**, *91*, 2957.

[120]Yao, K. S.; Wang, D. Y.; Chang, C. Y.; Weng, K. W.; Yang, L. Y.; Lee, S. J.;

Cheng, T. C.; Hwang, C. C. *Surf. Coat. Technol.* **2007**, *202*, 1329.

[121]Hu, C.; Lan, Y. Q.; Qu, J. H.; Hu, X. X.; Wang, A. M. *J. Phys. Chem. B* **2006**,

110, 4066.

[122]Hu, C.; Guo, J.; Qu, J. H.; Hu, X. X. *Langmuir* **2007**, *23*, 4982.

[123]Wang, P.; Huang, B. B.; Qin, X. Y.; Zhang, X. Y.; Dai, Y.; Whangbo, M. H.

Inorg. Chem. **2009**, *48*, 10697.

[124]Li, Q.; Li, Y. W.; Wu, P. G.; Xie, R. C.; Shang, J. K. *Adv. Mater.* **2008**, *20*, 3717.

[125]Elahifard, M. R.; Rahimnejad, S.; Haghghi, S.; Gholami, M. R. *J. Am. Chem.*

Soc. **2007**, *129*, 9552.

[126]Gulyas, H.; Jain, H. B.; Susanto, A. L.; Malekpur, M.; Harasiuk, K.; Krawczyk,

- I.; Choromanski, P.; Furmanska, M. *Environ. Technol.* **2005**, *26*, 501.
- [127]Li, H. X.; Bian, Z. F.; Zhu, J.; Zhang, D. Q.; Li, G. S.; Huo, Y. N.; Li, H.; Lu, Y. *F. J. Am. Chem. Soc.* **2007**, *129*, 8406.
- [128]Lin, G. F.; Zheng, J. W.; Xu, R. *J. Phys. Chem C* **2008**, *112*, 7363.
- [129]Zhang, Z. H.; Hossain, M. F.; Takahashi, T. *Mater. Lett.* **2010**, *64*, 435.
- [130]Iwasaki, M.; Park, W. K. *J. Nanomater.* **2008**, 169536.
- [131]Zhang, L. W.; Cheng, H. Y.; Zong, R. L.; Zhu, Y. F. *J. Phys. Chem C* **2009**, *113*, 2368.
- [132]Lu, M. Y.; Lu, M. P.; Chung, Y. A.; Chen, M. J.; Wang, Z. L.; Chen, L. J. *J. Phys. Chem C* **2009**, *113*, 12878.
- [133]Mills, A.; Davies, R. H.; Worsley, D. *Chem. Soc. Rev.* **1993**, *22*, 417.
- [134]Ho, W.; Yu, J. C.; Lee, S. *Chem. Commun.* **2006**, 1115.
- [135]Liu, Y. H.; Lin, C. W.; Chang, M. C.; Shao, H.; Yang, A. C. M. *J. Mater. Sci.* **2008**, *43*, 5005.
- [136]Yoo, K.; Choi, H.; Dionysiou, D. D. *Chem. Commun.* **2004**, 2000.
- [137]Ding, K. L.; Miao, Z. J.; Liu, Z. M.; Zhang, Z. F.; Han, B. X.; An, G. M.; Miao, S. D.; Xie, Y. *J. Am. Chem. Soc.* **2007**, *129*, 6362.
- [138]Yang, H. G.; Sun, C. H.; Qiao, S. Z.; Zōu, J.; Liu, G.; Smith, S. C.; Cheng, H. M.; Lu, G. Q. *Nature* **2008**, *453*, 638.

- [139]Yang, H. G.; Liu, G.; Qiao, S. Z.; Sun, C. H.; Jin, Y. G.; Smith, S. C.; Zou, J.; Cheng, H. M.; Lu, G. Q. *J. Am. Chem. Soc.* **2009**, *131*, 4078.
- [140]Zhang, D. Q.; Li, G. S.; Yang, X. F.; Yu, J. C. *Chem. Commun.* **2009**, 4381.
- [141]Liu, G.; Yang, H. G.; Wang, X. W.; Cheng, L. N.; Pan, J.; Lu, G. Q.; Cheng, H. M. *J. Am. Chem. Soc.* **2009**, *131*, 12868.
- [142]Liu, M.; Piao, L. Y.; Zhao, L.; Ju, S. T.; Yan, Z. J.; He, T.; Zhou, C. L.; Wang, W. *J. Chem. Commun.* **2010**, *46*, 1664.
- [143]Kudo, A.; Miseki, Y. *Chem. Soc. Rev.* **2009**, *38*, 253.
- [144]Osterloh, F. E. *Chem. Mater.* **2008**, *20*, 35.
- [145]Eisenberg, R. *Science* **2009**, *324*, 44.
- [146]Maeda, K.; Teramura, K.; Lu, D. L.; Takata, T.; Saito, N.; Inoue, Y.; Domen, K. *Nature* **2006**, *440*, 295.
- [147]Yerga, R. M. N.; Galvan, M. C. A.; del Valle, F.; de la Mano, J. A. V.; Fierro, J. L. G. *Chemsuschem* **2009**, *2*, 471.
- [148]Wang, X. C.; Maeda, K.; Thomas, A.; Takanabe, K.; Xin, G.; Carlsson, J. M.; Domen, K.; Antonietti, M. *Nat. Mater.* **2009**, *8*, 76.
- [149]Wang, X. C.; Maeda, K.; Chen, X. F.; Takanabe, K.; Domen, K.; Hou, Y. D.; Fu, X. Z.; Antonietti, M. *J. Am. Chem. Soc.* **2009**, *131*, 1680.
- [150]Yu, J. C.; Wang, X. C.; Fu, X. Z. *Chem. Mater.* **2004**, *16*, 1523.

- [151]Chen, X. F.; Jun, Y. S.; Takanabe, K.; Maeda, K.; Domen, K.; Fu, X. Z.; Antonietti, M.; Wang, X. C. *Chem. Mater.* **2009**, *21*, 4093.
- [152]Nguyen, T. V.; Wu, J. C. S.; Chiou, C. H. *Catal. Commun.* **2008**, *9*, 2073.
- [153]Varghese, O. K.; Paulose, M.; LaTempa, T. J.; Grimes, C. A. *Nano Lett.*, *10*, 750.
- [154]Guan, G. Q.; Kida, T.; Yoshida, A. *Appl Catal B-Environ.* **2003**, *41*, 387.
- [155]Guan, G. Q.; Kida, T.; Harada, T.; Isayama, M.; Yoshida, A. *Appl. Catal. A-Gen.* **2003**, *249*, 11.
- [156]Pan, P. W.; Chen, Y. W. *Catal. Commun.* **2007**, *8*, 1546.
- [157]Wang, C. J.; Thompson, R. L.; Baltrus, J.; Matranga, C. *J. Phys. Chem. Lett.* **2010**, *1*, 48.
- [158]Cushing, B. L.; Kolesnichenko, V. L.; O'Connor, C. J. *Chem. Rev.* **2004**, *104*, 3893.
- [159]Polshettiwar, V.; Varma, R. S. *Chem. Soc. Rev.* **2008**, *37*, 1546.
- [160]Bilecka, I.; Djerdj, I.; Niederberger, M. *Chem. Commun.* **2008**, 886.
- [161]Pinna, N.; Grancharov, S.; Beato, P.; Bonville, P.; Antonietti, M.; Niederberger, M. *Chem. Mater.* **2005**, *17*, 3044.
- [162]Djerdj, I.; Arcon, D.; Jaglicic, Z.; Niederberger, M. *J. Phys. Chem. C* **2007**, *111*, 3614.

- [163]Niederberger, M.; Garnweitner, G.; Pinna, N.; Antonietti, M. *J. Am. Chem. Soc.* **2004**, *126*, 9120.
- [164]Zhou, B.; Ji, Y.; Yang, Y. F.; Li, X. H.; Zhu, J. H. *Cryst. Growth Des.* **2008**, *8*, 4394.
- [165]Pol, V. G.; Langzam, Y.; Zaban, A. *Langmuir* **2007**, *23*, 11211.
- [166]Moreira, M. L.; Andres, J.; Varela, J. A.; Longo, E. *Cryst. Growth Des.* **2009**, *9*, 833.
- [167]Celer, E. B.; Jaroniec, M. *J. Am. Chem. Soc.* **2006**, *128*, 14408.
- [168]Xu, Y. P.; Tian, Z. J.; Wang, S. J.; Hu, Y.; Wang, L.; Wang, B. C.; Ma, Y. C.; Hou, L.; Yu, J. Y.; Lin, L. W. *Angew. Chem. Int. Ed.* **2006**, *45*, 3965.

Chapter Two

Synthesis of Size-Tunable Monodispersed Metallic Nickel Nanocrystals without Hot Injection

2.1 Introduction

High-quality nanocrystals with well-defined shapes and controllable sizes play a key role in nanotechnology because the properties of nanometric materials are strongly related to their mean size and size distribution.¹⁻³ Uniform magnetic nanoscale materials have become the focus of intensive research due to their potential applications in high-density data storage⁴ and medical diagnosis.⁵ For the preparation of nickel nanomaterials, chemical or electrochemical reduction of Ni²⁺ ions in aqueous solution has been widely used.⁶⁻⁸ However, the as-synthesized nanometer-sized Ni particles are easily oxidized in an aqueous solution owing to their high reactivity. To overcome this problem, non-aqueous approaches have been developed as alternatives to aqueous systems.⁹⁻¹² The non-aqueous methods, however, often require a large amount of surfactants for controlling the growth and crystal size of the products. Furthermore, complex devices with protective atmosphere are

needed to inject rapidly precursors into a hot organic reaction medium.⁹⁻¹² Another problem with hot injection is that the Ni nanoparticles prepared are usually amorphous¹⁰ or poorly crystallized.^{13,14} Additional treatment steps are therefore required to achieve good crystallinity. It has also been reported that the resulting structures are strongly dependent on the reaction conditions.^{15,16} It is well known that intermolecular forces, such as Van der Waals forces and π - π interactions contribute to the aggregation of nanoparticles. As for magnetic nanoparticles, magnetic dipole-dipole interaction makes this kind of attraction even stronger.¹⁷ Thus, it is difficult to obtain uniformly dispersed magnetic nanoparticles without aggregation.

Herein, we present a fast and energy saving method to fabricate well crystallized Ni particles with continuously tunable sizes by a simple reaction involving nickel acetate tetrahydrate and hexadecylamine (HDA). As far as we know, such a one-pot route to the size-tunable crystallized Ni particles without precursor injection has never been reported. The resulting metallic nickel spherical particles were well dispersed and had uniform diameters. The diameter of the product could be tuned from ca. 58 nm to ca. 190 nm by controlling the reaction time. This is much easier than the methods reported in the literature which require multi-stabilizers to control the size and morphology of magnetic nanoparticles.^{10, 18} Our simple process is therefore less prone to contamination and it ensures high-purity products. Another

advantage of this method is that the reaction proceeds at atmospheric pressure in the absence of a protective gas (e.g. Ar or N₂) without stirring or refluxing. This is an improvement over the hydrothermal method in which high pressure and high temperature are involved.¹⁹

2.2 Experimental Section

2.2.1 Preparation of Monodispersed Nickel Nanocrystals

All reagents are of analytic purity and were used without further purification. In a typical synthesis, a mixture of 0.20 g nickel acetate tetrahydrate (Ni(OAc)₂) (ACROS, 99 %) and 8.20 g hexadecylamine (HDA) (IL, 99 %) was heated to 85 °C to make a homogeneous green solution. Then, the mixture in an open glass bottle was directly placed in the muffle furnace of 210 °C for 30 - 60 min. After the reaction, the resulting black Ni powder was easily collected by a magnet and was rinsed with 70 °C toluene for 5 times to remove the hexadecylamine, and then dried in a vacuum at 80 °C for 4 h.

2.2.2 Characterization

The products were characterized by X-ray diffraction measurements which was carried out in a parallel mode ($\omega = 0.5^\circ$, 2θ varied from 20° to 80°) using a Bruker D8 Advance X-ray diffractometer (Cu K α radiation, $\lambda = 1.5406 \text{ \AA}$). The morphology and the microstructures of the products were investigated by transmission electron microscope (TEM) and selected area electron diffraction (SAED) with a JEM-200CX (JEOL, 200 kV) TEM, and a high-resolution transmission electron microscope (HRTEM, JEOL-2010). The electron microscopy samples were recorded prepared by grinding and dispersing the powder in acetone with ultrasonication for 20 seconds. Carbon-coated copper grids were used as sample holders. The scanning electron microscopy images were recorded on a FEI Quanta 400 FEG microscope. The magnetic properties of the Ni samples were investigated using a vibrating sample magnetometer (VSM) from Lakeshore (Model 7300).

2.3 Results and Discussion

2.3.1 TEM and HRTEM Analysis

The particle size and shape of the products were examined by transmission electron microscopy (TEM) and field emission scanning electron microscopy

(FESEM). Fig. 2.1 shows the TEM and SEM images of products prepared at 210 °C for 30-60 min from 0.2 g nickel acetate tetrahydrate and 8.2 g HDA. It is observed that all of the products are composed of a large quantity of uniform particles. These particles are characterized by a narrow size distribution (relative standard deviation σ below 5 %), obtained from a statistical analysis of over 100 particles. It is very interesting that the mean diameter of the products is linearly dependent on the reaction time over the period from 30 to 60 min (Fig. 2.1a, d, g and j). When the reaction time was prolonged from 30 to 40, 50 and 60 min, the diameters of the resulting Ni nanocrystals were roughly 58, 123, 160 and 190 nm, respectively. A reaction time shorter than 30 min is not advised as a NiO byproduct will be formed. All the samples assemble spontaneously to form a 2D close-packed structure on the TEM grids, demonstrating the uniformity of the particle size. The high magnification TEM images (Fig. 2.1b, e, h and k) and FESEM images (Fig. 2.1c, f, i and l) further show clearly that the samples exhibit spherical morphology with hierarchical surfaces.

It is also worth noting that these as-formed Ni nanocrystals are well-dispersed nanocrystals. It has been reported that metallic Fe spheres form nanowires easily in aqueous systems because of internal forces of attraction.²⁰ In the current system, the Ni nanocrystals stay well separated in spite of the high magnetic property of metallic

Ni. This result illustrates the effectiveness of HDA molecules as a stabilizer.⁹ The HDA molecule serves as a template within which the nanoparticles grow, a scenario similar to that where nanoparticles are formed in micellar systems. A possible model for such nanoparticle growth is shown in Scheme 2.1. Due to the steric hindrance between the hydrocarbon units of HDA, the chance of self-aggregation for the magnetic nanoparticle is decreased. Concerning the diameter evolution of the Ni crystals, HDA can also act as an excellent solvent for the growth of metallic nickel. Fig. 2.2 shows the mean particle size (D) of the Ni crystals as a function of reaction time (t). It reveals a clear trend of particle size evolution. The former (D) nearly increases in direct proportion to the latter (t) with an equation, D (nm) = $-63.7 + 4.35 \cdot t$ (min). This equation has a very high gradient of 4.35, representative of the growth rate of the Ni crystals. It is reasonable that the reaction proceeds at a fast rate because the nickel acetate precursors dissolved in HDA can be easily decomposed at fixed reaction temperature and thus lead to a high concentration of the free Ni nanocrystal monomers. It has been demonstrated that the fine control of the particle size of Ni crystals has been achieved from direct thermal decomposition of nitrate salts in HDA by choosing different reaction times, as shown in Fig. 2.1 and Fig. 2.2.

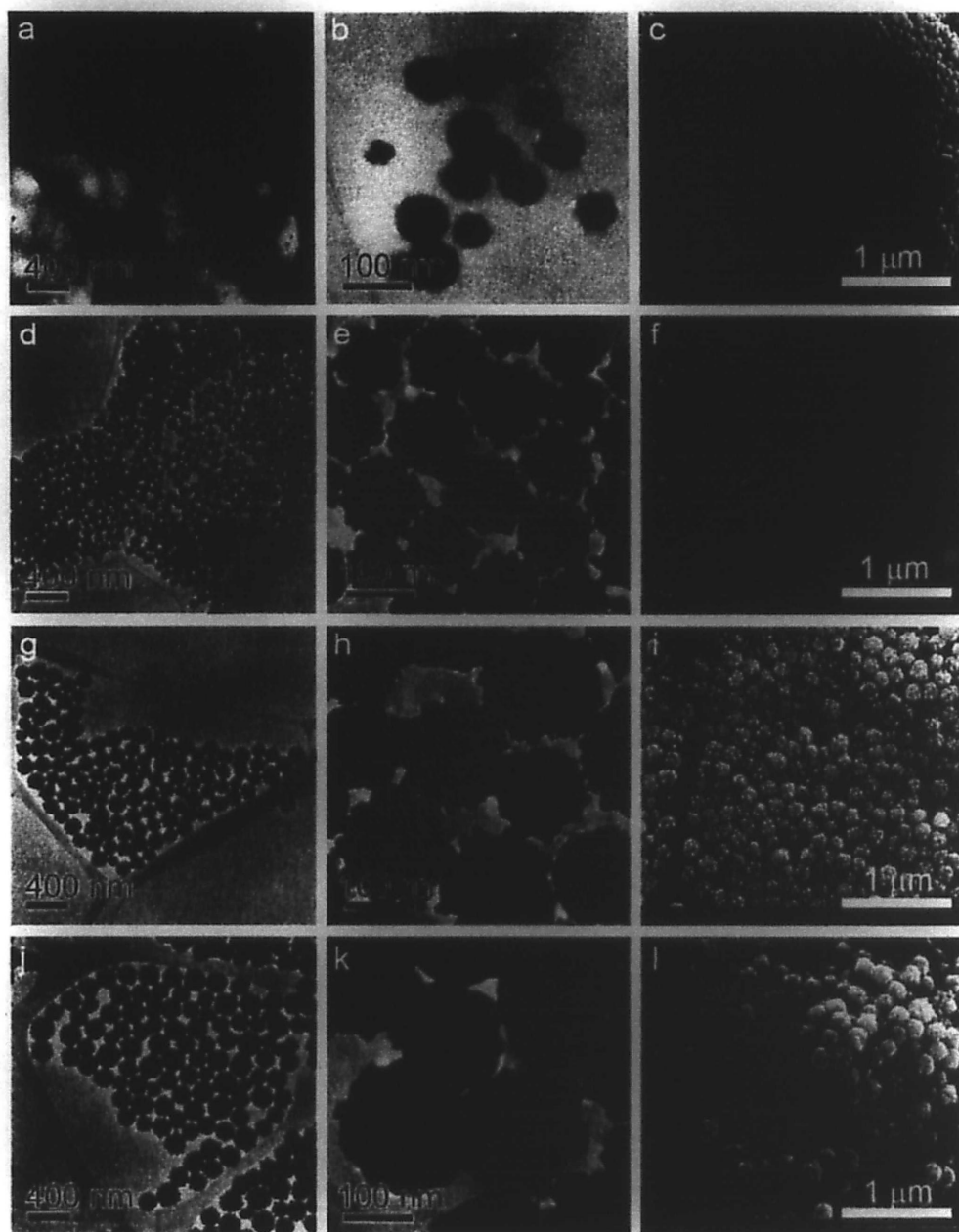


Figure 2.1 TEM, high magnification TEM and FESEM images of the nickel nanocrystals obtained at 210 °C for different reaction times using 0.2 g nickel acetate tetrahydrate. a), b), c) 30 min, d), e), f) 40 min, g), h), i) 50 min, j), k), l) 60 min.

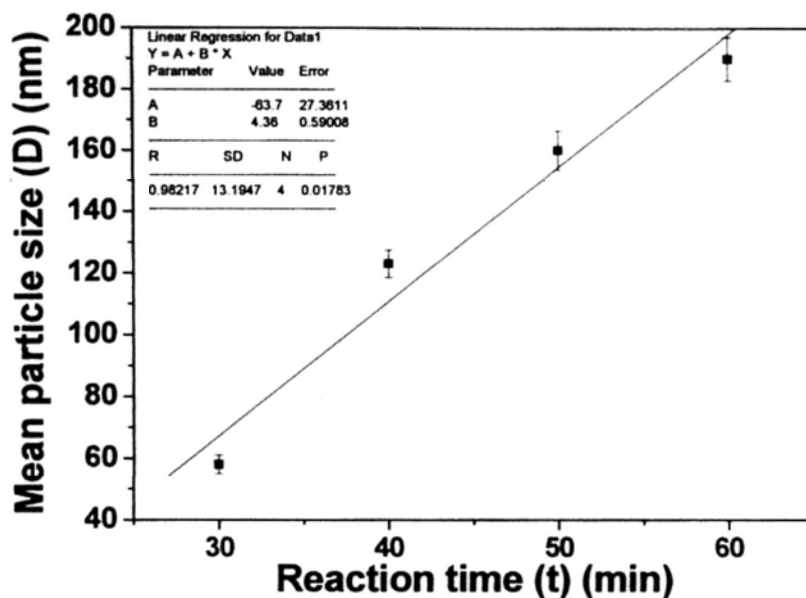


Figure 2.2 Mean particle size (D) of the Ni crystals as a function of reaction time (t).

2.3.2 XRD Analysis

As reported previously, the Ni nanoparticles prepared by chemical reduction in organic media are often amorphous or poorly crystallized.^{13,14} Therefore, an annealing treatment is usually needed in order to improve the crystallinity of the Ni colloidal nanoparticles. It is also known that despite an improvement of the atomic order towards the face-centered cubic (fcc) structure being obtained after calcination, defects in the structure could not be avoided. Moreover, it is difficult to improve the crystallinity by increasing the temperature and treatment time.¹² Our method overcomes these limitations. Fig. 2.3a shows the powder X-ray diffraction (XRD) patterns of the Ni particles. The three well resolved diffraction peaks suggest good crystallinity. The peaks are located at 44.53°, 51.82° and 76.41° which can be

indexed to the (111), (200) and (220) Bragg reflections of the fcc structure of Ni (Joint Committee on Powder Diffraction Standards (JCPDS) file No. 04-0850). No nickel oxide peaks (such as NiO or Ni₂O₃) could be detected, indicating that metallic nickel is the only product from the decomposition of nickel acetate tetrahydrate in hexadecylamine. Further structural information on the as-synthesized Ni products after 60 min reaction can be obtained from the high resolution TEM (HRTEM) image (Fig. 2.3b). The lattice fringes identified in the images are consistent with the {111} planes of the fcc structure phase of metallic Ni, with a ~2.0 Å periodicity. The local elemental composition of the as-formed sample obtained after 60 min reaction was studied by energy-dispersive X-ray (EDX) analysis at the single nanocrystal level, shown in Fig. 2.3c. It confirms that besides nickel only trace amounts of copper from the TEM grids and carbon from the residue of HDA are found in the products.

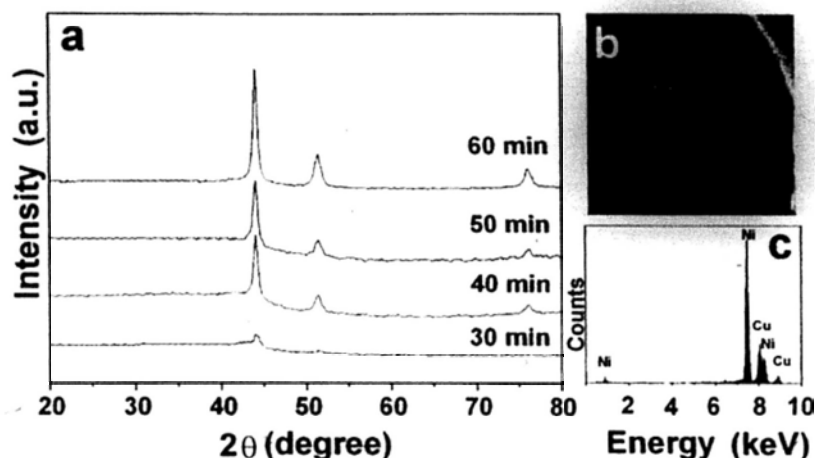


Figure 2.3 a) Powder XRD patterns of the samples prepared at 210 °C for different durations. b) HRTEM image and c) EDX pattern of the sample prepared at 210 °C for 60 min reaction.

2.3.3 Growth Process

In order to understand the growth process of Ni hierarchical crystals, the reaction temperature of a particular experiment was decreased from 210 °C to 200 °C with 1.0 g nickel acetate tetrahydrate as nickel precursor and other reaction conditions fixed. Fig. 2.4 shows the XRD results of the samples prepared at 200 °C for different reaction times. All XRD patterns from samples with < 6 hrs reaction show three well resolved diffraction peaks located at 37.25°, 43.27° and 62.88°. These can be indexed to the (111), (200) and (220) Bragg reflections of the fcc structure of NiO (Joint Committee on Powder Diffraction Standards (JCPDS) file No. 47-1049). For samples with > 7 hrs reaction time, the NiO nanoparticles were reduced to Ni as revealed by the XRD patterns (Fig. 2.4). The morphologies of the resulting NiO/Ni

samples obtained at different stages were further investigated by TEM. From Fig. 2.5a and b, we can see that a large-area of the monodispersed flower-shaped NiO clusters (ca. 25 nm in diameter) obtained after 60 min at 200 °C. The secondary structure of the as-formed NiO clusters can be observed more clearly in Fig. 2.5c for isolated clusters. Obviously, these clusters are composed of small primary crystals with a size of 2-3 nm and the same crystal orientation. The distance between two adjacent planes is 2.41 Å, which corresponds to the lattice spacing of {111} planes of cubic NiO. The selected-area electron diffraction (SAED) pattern recorded on an isolated cluster inset reveals single-crystal-like diffraction (inset of Fig. 2.5c). The formation of NiO clusters with a single-crystal-like feature could be explained by the well-known growth mechanism of “oriented attachment”.²¹⁻²³ The growth of these NiO clusters follows the well-documented two-step growth model in which primary nanocrystals nucleate first in a supersaturated solution and then aggregate into larger secondary particles due to high surface energy.^{21,24} This aggregation process led to monodispersed NiO clusters in which the primary nanocrystals monomers assemble through the same crystallographic orientation. As shown in Fig. 2.5a-e, the size of NiO clusters could be tuned from about 25 to 40 nm by simply increasing the reaction time while keeping all other parameters constant. It is more interesting that all of the NiO clusters were quickly reduced to metallic Ni clusters with an average

size of about 40 nm upon 7 h of reaction, as shown in Fig. 2.5f. The reducing ability of alkylamine has been reported in the synthesis of metallic copper nanowires by using octadecylamine as the reducing agent.²² With further increase of the reaction time, these freshly formed Ni clusters have a great tendency to aggregate rapidly due to their strong magnetism. Fig. 2.5g shows that a close-packed core of metallic nickel surrounded with lots of Ni clusters had been formed after 12 h. These Ni clusters were further confirmed by the HRTEM images (Fig. 2.5h). It shows the {111} atomic planes of Ni phase with a lattice spacing of 0.20 nm. During the thermal-induced aggregation process, the introduction of capping agents (HDA) promotes the anisotropic growth of Ni nanostructures, probably driven by the “oriented attachment” mechanism associate with Ostwald ripening.²⁵ Upon 18 hrs of reaction, the aggregation of these Ni clusters was completed to form monodispersed hierarchical crystals with an average size of about 2 μm , as shown in Fig. 2.5i. The formation process of Ni hierarchical nanocrystals was illustrated in Scheme 2.1.

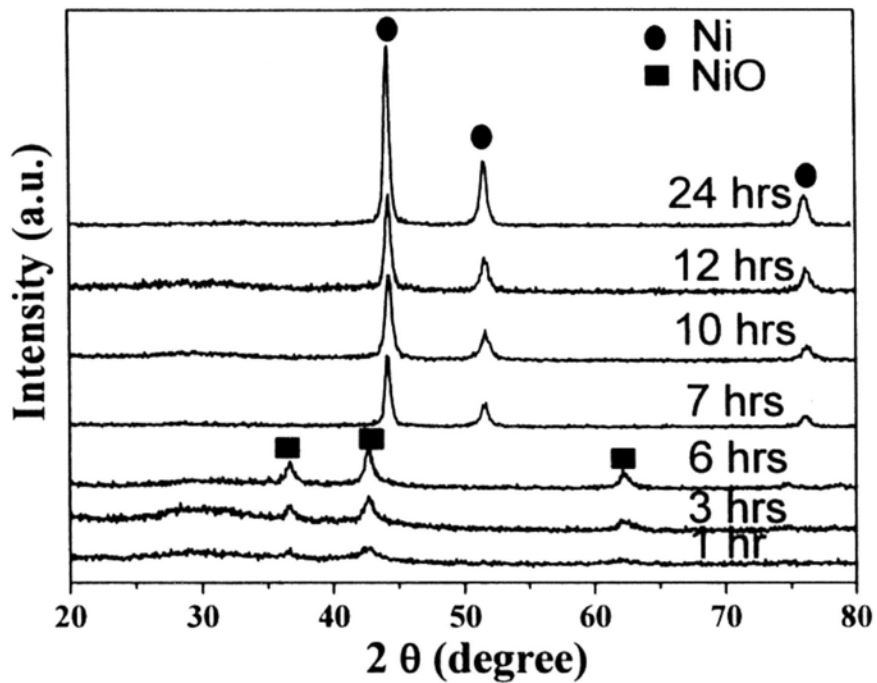
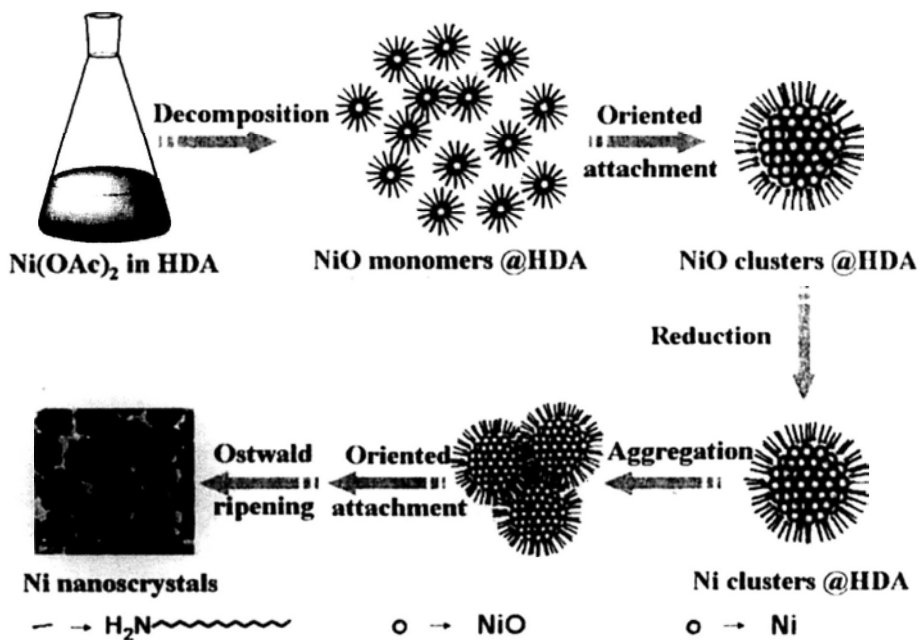


Figure 2.4 Powder XRD patterns of Ni nanocrystals prepared at 200 °C for different durations using 1 g nickel acetate tetrahydrate.



Scheme 2.1 Illustration of a proposed mechanism for the formation of Ni nanocrystals.

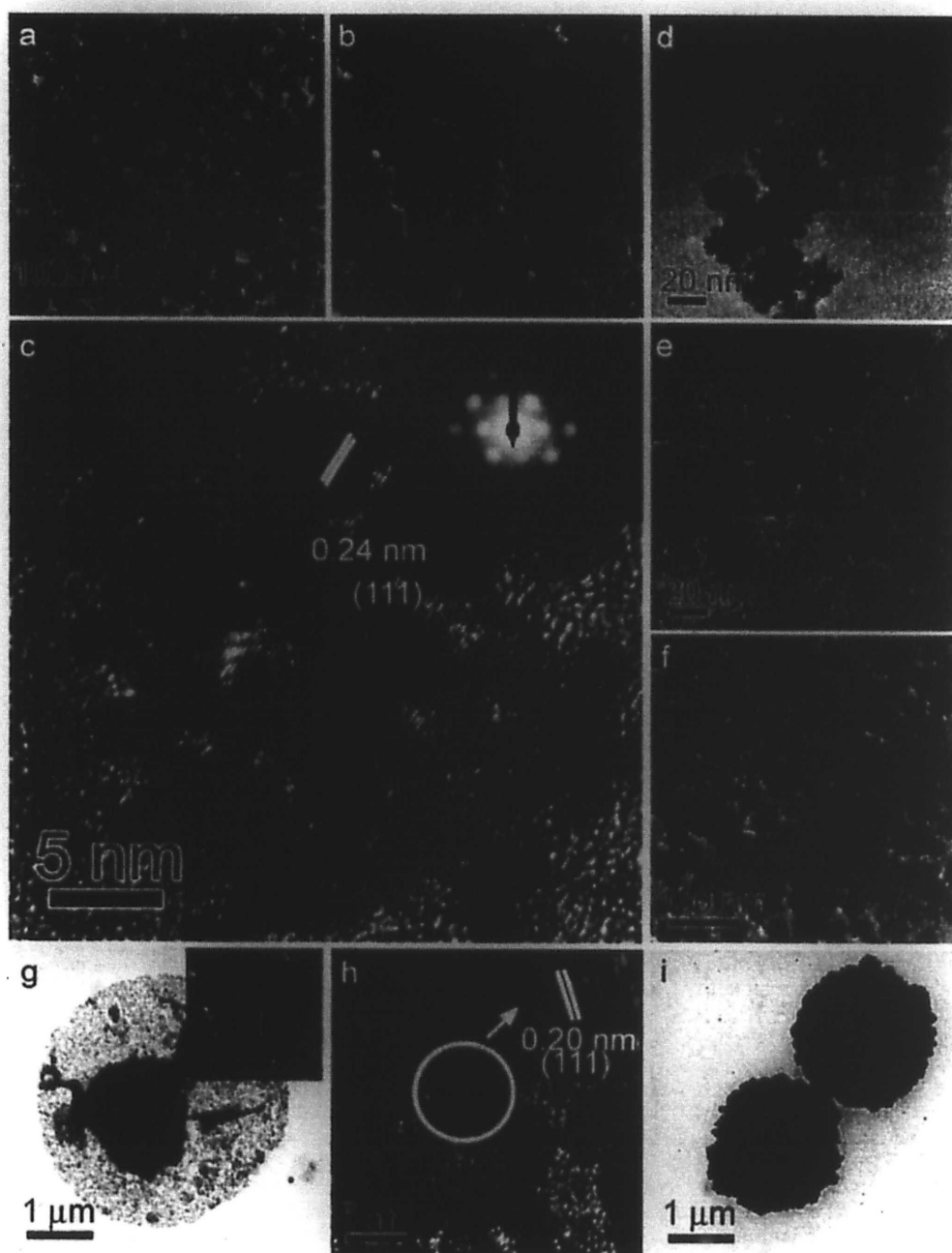


Figure 2.5 TEM images of the samples prepared at 200 °C for different durations. a-c) 1 hr, d) 3 hrs, e) 6 hrs, f) 7 hrs, g,h) 12 hrs, and i) 18 hrs.

2.3.4 Magnetic property

Fig. 2.6a displays the hysteresis loops measured at room temperature for the Ni nanocrystals prepared at 210 °C with various reaction times. Fig. 2.6b illustrates the relationship between the particle size and the magnetic properties. The coercivity value ranges from 106.1 Oe to 152.9 Oe as the particle size increases from 58 nm to 190 nm. Fig. 2.1f and Fig. 2.1i clearly show a drastic increase in anisotropy between 40-50 min of reaction time. Since the coercivity of magnetic material depends strongly on the shape anisotropy, a sharp increase in the coercivity occurs. Compared to the corresponding H_c value for bulk Ni (0.7 Oe), great enhancement occurs in the coercivities of all the Ni nanocrystals. This observation is consistent with previous reports.¹⁷ This enhancement may be attributed to the reduced size and presence of a hierarchical structure which causes a change in the magnetization reversal mechanism.²⁶ An increase in coercivity of a magnetic material has been considered to have resulted from an increase in the magnetic anisotropy, since an applied field at a given temperature can change the orientation of magnetization.²⁷ The saturation magnetization (M_s) for the as-prepared Ni nanocrystals increased from 38.7, 39.88, 41.12 to 46.3 emu g^{-1} with the increasing particle size. The same trend was recorded for the remanence to saturation ratio (M_r/M_s). The results confirm that the coercivity and remanence are mainly governed by the particle size. Alongside this, shape

anisotropy also affects the coercivity and remanence because of the hierarchical surfaces in the Ni sample. This is because when a particle is not perfectly spherical the demagnetizing field will not be equal for all directions. Understanding the relationship between the size, hierarchical surfaces and magnetic properties is important both for fundamental research and for the development of potential applications in electronics and information technologies.

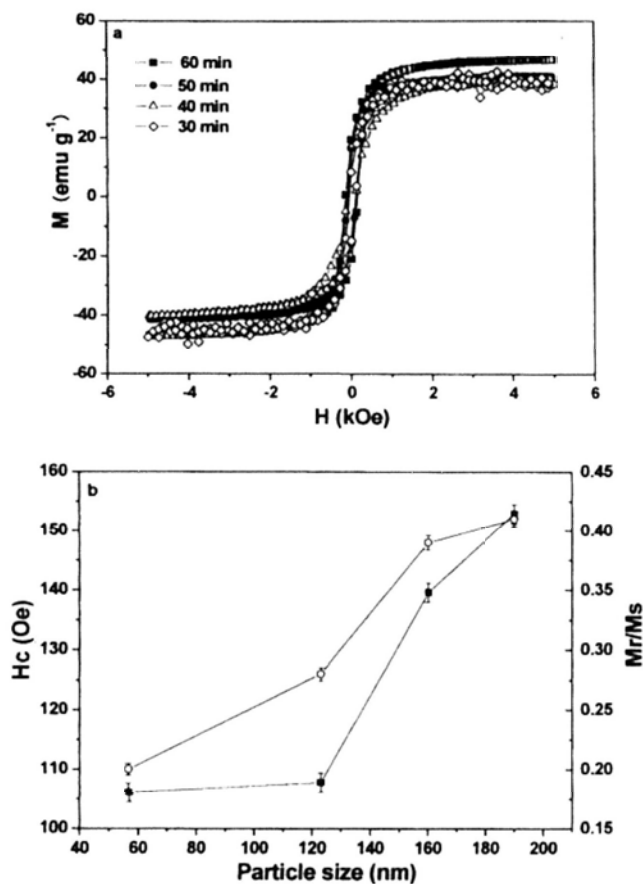


Figure 2.6 a) Magnetization loops of (a) Ni nanocrystals prepared at 210 °C for different reaction times using 0.2 g nickel acetate tetrahydrate. i) 30 min (-◇-), ii) 40 min (-△-), iii) 50 min (-●-), iv) 60 min (-■-). b) coercivity, H_c (-■-), and remanence to saturation ratio, M_r/M_s (-◇-) vs particle sizes of Ni nanocrystals prepared at 210 °C for different reaction time.

2.4 Conclusion

A new method was developed for the synthesis of magnetic nickel nanocrystals with uniform and tunable particle sizes ranging from 58 nm to 190 nm, by using hexadecylamine as a reducing agent and solvent, and nickel acetate tetrahydrate as a nickel precursor. These synthesized Ni nanocrystals exhibit room-temperature enhanced magnetic properties. Such a facile one-pot approach may also be applied

for the synthesis of other low valence state functional nanomaterials such as Cu_2O , and Fe_3O_4 . Detailed work is underway.

2.5 References

- [1] Yin, M.; Wu, C. K.; Lou, Y. B.; Burda, C.; Koberstein, J. T.; Zhu, Y. M.; O'Brien, S. *J. Am. Chem. Soc.* **2005**, *127*, 9506.
- [2] Peng, X. G.; Wickham, J.; Alivisatos, A. P. *J. Am. Chem. Soc.* **1998**, *120*, 5343.
- [3] Tang, Z. Y.; Kotov, N. A.; Giersig, M. *Science* **2002**, *297*, 237.
- [4] Leslie-Pelecky, D. L.; Rieke, R. D. *Chem. Mater.* **1996**, *8*, 1770.
- [5] Jordan, A.; Scholz, R.; Wust, P.; Föhling, H.; Felix, R. *J. Magn. Magn. Mater.* **1999**, *201*, 413.
- [6] Sun, Y. P.; Rollins, H. W.; Guduru, R. *Chem. Mater.* **1999**, *11*, 7.
- [7] Wang, X. W.; Fei, G. T.; Xu, X. J.; Jin, Z.; Zhang, L. D. *J. Phys. Chem. B* **2005**, *109*, 24326.
- [8] Ni, X. M.; Zhao, Q. B.; Zhang, D. E.; Zhang, X. J.; Zheng, H. G. *J. Phys. Chem. C* **2007**, *111*, 601.
- [9] Hou, Y. L.; Gao, S. *J. Mater. Chem.* **2003**, *13*, 1510.

- [10] Park, J.; Kang, E.; Son, S. U.; Park, H. M.; Lee, M. K.; Kim, J.; Kim, K. W.; Noh, H. J.; Park, J. H.; Bae, C. J.; Park, J. G.; Hyeon, T. *Adv. Mater.* **2005**, *17*, 429.
- [11] Leng, Y. H.; Li, Y.; Li, X. G.; Takahashi, S. *J. Phys. Chem. C* **2007**, *111*, 6630.
- [12] Winnischofer, H.; Rocha, T. C. R.; Nunes, W. C.; Socolovsky, L. M.; Knobel, M.; Zanchet, D. *ACS Nano* **2008**, *2*, 1313.
- [13] Jeon, Y. T.; Lee, G. H.; Park, J. H.; Kim, B. S.; Chang, Y. M. *J. Phys. Chem. B* **2005**, *109*, 12257.
- [14] Hou, Y.; Kondoh, H.; Ohta, T.; Gao, S. *Appl. Surf. Sci.* **2005**, *241*, 218.
- [15] Chen, D. H.; Hsieh, C. H. *J. Mater. Chem.* **2002**, *12*, 2412.
- [16] Jeon, Y. T.; Moon, J. Y.; Lee, G. H.; Park, J. H.; Chang, Y. M. *J. Phys. Chem. B* **2006**, *110*, 1187.
- [17] Jia, F. L.; Zhang, L. Z.; Shang, X. Y.; Yang, Y. *Adv. Mater.* **2008**, *20*, 1050.
- [18] Puentes, V. F.; Krishnan, K. M.; Alivisatos, A. P. *Science* **2001**, *291*, 2115.[†]
- [19] Liu, Z.; Li, S.; Yang, Y.; Peng, S.; Hu, Z.; Qian, Y. *Adv. Mater.* **2003**, *15*, 1946.
- [20] Lu, L. R.; Ai, Z. H.; Li, J. P.; Zheng, Z.; Li, Q.; Zhang, L. Z. *Cryst. Growth Des.* **2007**, *7*, 459.

- [21] Ge, J. P.; Hu, Y. X.; Biasini, M.; Beyermann, W. P.; Yin, Y. D. *Angew. Chem. Int. Ed.* **2007**, *46*, 4342.
- [22] Narayanaswamy, A.; Xu, H. F.; Pradhan, N.; Peng, X. G. *Angew. Chem. Int. Ed.* **2006**, *45*, 5361.
- [23] Hu, X. L.; Gong, J. M.; Zhang, L. Z.; Yu, J. C. *Adv. Mater.* **2008**, *20*, 4845.
- [24] Libert, S.; Gorshkov, V.; Goia, D.; Matijević, E.; Privman, V. *Langmuir* **2003**, *19*, 10679.
- [25] Murphy, C. J.; Jana, N. R. *Adv. Mater.* **2002**, *14*, 80.
- [26] Hwang, J. H.; Dravid, V. P.; Teng, M. H.; Host, J. J.; Elliott, B. R.; Johnson, D. L.; Mason, T. O. *J. Mater. Res.* **1997**, *12*, 1076.
- [27] Zhao, F.; Sun, H. L.; Su, G.; Gao, S. *Small* **2006**, *2*, 244.

Chapter Three

Ionic Liquids-Assisted Synthesis of 3D BiOX (X=Br, Cl) Ternary Compounds Mesocrystals

3.1 Introduction

Bismuth oxyhalides belong to V-VI-VII ternary compound with tetragonal crystal structure. They are layered structures consist of a halide ion layer and a metal-oxygen (Bi-O) layer. Their high stability against photocorrosion is advantageous for applications in photocatalysis and photoelectrochemical cells.¹⁻³ Several synthesis methods for micro- and nanostructures of BiOX materials have been reported in the literature. The size controllable synthesis of spherical BiOX nanoparticles with diameters of 3-22 nm was reported by Henle et al. using an effective reverse microemulsions route.⁴ Deng et al. reported the synthesis of one-dimensional (1D) bismuth oxyhalide nanowires and nanotubes using a cationic surfactant cetyltrimethylammonium bromide (CTAB) as the bromine source.⁵ Geng et al. reported a procedure for one-step selective synthesis of two-dimensional (2D) BiOCl lamellae materials via a sonochemical method.⁶ 2D single-crystalline BiOX

(X = Cl, Br) nanoplates, nanosheets, and microsheets were obtained by hydrogen peroxide oxidation of bulk metal Bi particles in a surfactant-mediated solution.⁷ To date, the methods for fabrication of three-dimensional (3D) BiOX materials are less developed. One approach is to use bismuth nitrate and inorganic halide salts as the starting material through a coprecipitation process.^{1,8} This method is rather time- and also energy-consuming due to the long reaction time in a high-temperature environment. Therefore, new effective and reproducible route to large-scale fabrication of 3D BiOX with uniform shapes is highly desirable.

Ionic liquids (ILs) are non-volatile and non-flammable organic salts with low melting point. The use of ILs is well documented in important fields such as synthetic-organic chemistry, separation and electrochemistry.⁹⁻¹¹ The value of ILs in the field of inorganic nanosynthesis has gradually been realized. In 2000, Dai's group first reported the synthesis of SiO₂ aerogel using an ionic liquid, 1-ethyl-3-methylimidazolium bis(trifluoromethylsulfonyl)imide ([EMim][NTf₂]), instead of water as the solvent.¹² Among the main advantages of using ILs as solvents or additives in inorganic synthesis is their superior capability for the solvation and stabilization of metal cations. This is why ILs are often used as capping agents or surfactants. These properties have been exploited to prepare nanoparticles of different compositions including pure metals,¹³⁻¹⁹ metal oxides,²⁰⁻²³ metal

chalcogenides,^{24,25} silicas and organosilicas,²⁶⁻³¹ metal salts³²⁻³⁶, and carbon material.^{37,38} Nevertheless, the full potential of ILs as the reagents in the controllable synthesis of inorganic nanostructures remains to be further explored.

Herein, we report that ionic liquids act as a unique soft material capable of promoting the nucleation and in situ growth of 3D bismuth oxyhalide (BiOBr, BiOCl) mesocrystals. To the best of our knowledge, this is the first example of ternary compound mesocrystal grown from ionic liquids. The BiOX products prepared by the new method have low band gap energy, high surface to bulk ratio, facile species transportation, as well as easy recovery and regeneration. These properties make the materials ideal photocatalysts for generating hydrogen, degrading organic pollutants and killing bacteria.

Our strategy for preparing BiOX is based on the solvothermal reaction involving bismuth nitrate and an imidazolium-based ionic liquid in triethylene glycol. The key in this method is the use of the 1-butyl-3-methyl-imidazolium IL which forms an ionic-liquid-bismuth complex which evolves into the final 3D superstructure. By selecting an appropriate anion for the ionic liquid, bismuth oxybromide and oxychloride can be synthesized. The chemical structures of the ionic liquids used in this work are shown below.



1-butyl-3-methyl-imidazolium bromide



1-butyl-3-methyl-imidazolium chloride

3.2 Experimental Section

3.2.1 Preparation of BiOBr Sample

In a typical synthesis of BiOBr, 0.485 g of bismuth nitrate (ACROS) was dissolved in 10 mL of triethylene glycol (Panreac) in an ultrasonic bath. Then ionic liquid, 0.5 mL of 1-butyl-3-methyl-imidazolium-bromide (IL) was added into it under stirring. Then the mixture was put into a 25 mL Teflon-lined stainless autoclave. The autoclave was heated to 200 °C and maintained for 1 hour. The resulting precipitates were collected and washed with ethanol and deionised water thoroughly and dried at 80 °C in air. BiOCl was fabricated by replacing 1-butyl-3-methyl-imidazolium-bromide with 1-butyl-3-methyl-imidazolium-chloride (IL) while keeping the other conditions the same.

3.2.2 Characterization

The products were characterized by X-ray diffraction measurements which was carried out in a parallel mode ($\omega = 0.5^\circ$, 2θ varied from 20° to 80°) using a Bruker D8 Advance X-ray diffractometer (Cu K α radiation, $\lambda = 1.5406 \text{ \AA}$). The morphology and the microstructures of the products were investigated by transmission electron microscope (TEM) and selected area electron diffraction (SAED) with a JEM-200CX (JEOL, 200 kV) TEM, and a high-resolution transmission electron microscope (HRTEM, JEOL-2010). The electron microscopy samples were recorded prepared by grinding and dispersing the powder in acetone with ultrasonication for 20 seconds. Carbon-coated copper grids were used as sample holders. The scanning electron microscopy images were recorded on a FEI Quanta 400 FEG microscope.

3.2.3 Measurements of Photocatalytic Activity

In the hydrogen generation reaction, 100 mg photocatalyst were added into an aqueous solution containing 100 mL H₂O, 20 mL methanol and 0.1 mL 1g/L H₂PtCl₆. The reaction cell was sealed with a rubber septum and irradiated using a 300 W xenon lamp with a 400 nm optical filter. The platinum precursor was reduced to platinum particles by photoexcited electrons and deposited on the surface of photocatalysts at the initial stage of photoirradiation. Methanol acts as an electron

donor. The reaction system was cooled by the flowing water to minimize the temperature rise. The amount of the hydrogen generated was determined by using a gas chromatograph system (Techcomp, GC-7900) equipped with a molecular sieve column (TDX-01, 60-80 mesh).

The photocatalytic degradation of methylene blue was carried out in an aqueous solution at ambient temperature. Briefly, in a 100 mL beaker, 0.03 g of BiOBr photocatalyst was suspended in 80 ml aqueous solution containing 40 ppm methylene blue. The aqueous suspension was stirred for 2 h to reach an adsorption/desorption equilibrium. The photocatalytic degradation of methylene blue was initiated by irradiating the reaction mixture with a commercial 300 W tungsten halogen spotlight surrounded with a filter that restricted the illumination to the 400–660 nm range. The light source was located at 8 cm from the reaction solution. The photodegradation rate was monitored by measuring the absorbance of the solution of 664 nm. Preliminary tests demonstrated a good linear relationship between the light absorbance and the methylene blue concentration. Only less than 2.0% methylene blue decomposed after reaction for 3 h in the absence of either the photocatalyst or the light irradiation and, thus, could be neglected in comparison with the methylene blue degraded via photocatalysis.

3.2.4 Measurements of Bactericidal Activity

Micrococcus lylae, a Gram positive bacterium, was used as a model bacterium in the experiment. It was incubated in 10 % Trypticase soy broth (TSB) at 30°C and agitated at 200 rpm for 24 h. The culture was washed with 0.9 % saline by centrifugation at 21,000 rpm for 5 min at 25°C and the pellet was resuspended in saline. The cell suspension was adjusted in centrifuged tube to the required cell concentration ($1-2 \times 10^8$ cfu ml⁻¹). The photocatalyst BiOBr was added to 0.9 % saline in a conical flask and homogenized by sonication. The suspension was then sterilized by autoclaving at 121 °C for 20 min, allowed to cool, and mixed with the prepared cell suspension. The final photocatalyst concentration was adjusted to 100 mg/L and the final bacterial cell concentration was $1-2 \times 10^7$ cfu ml⁻¹. The photocatalytic reaction was started by irradiating the mixture with fluorescent light and stopped by switching off the light. The light source used was four 15 W fluorescent lamps mounted closely on the top of the flask. The reaction mixture was stirred with a magnetic stirrer to prevent settling of the photocatalyst. Before and during the light irradiation, an aliquot of the reaction mixture was immediately diluted with 0.9 % saline and plated on TSB agar. The colonies were counted after incubation at 37 °C for 48 h. The inactivation of bacterial population during PCO was calculated by the equation:

$$\text{Bacterial inactivation (\%)} = [(P_1 - P_T) / P_1] \times 100 \%$$

where P_1 represented the initial population and P_T represented the population after irradiation time (T).

3.3 Results and Discussion

3.3.1 TEM and XRD Analysis

Fig. 3.1a-d shows the field-emission scanning electron microscopy (FESEM) images of the ternary BiOBr powders with different magnifications. The samples were obtained under the solvothermal condition at 200 °C for 1 hour. The low-magnification FESEM images (Fig. 3.1a and b) show the high-yield synthesis of mesocrystals with an average diameter of 4.5 μm. The particles are uniformly dispersed without obvious aggregation. Close inspection (Fig. 3.1c and d) shows an interesting 3D marigold-like morphology. The flower-like superstructures are composed of nanosheets with thickness of 15 nm, forming an open porous structure.

The results of transmission electron microscopy (TEM) images give more detailed information regarding the interior structure of the flower-like architectures. Fig. 3.1e reveals that the entire structure is built from several dozens of nanosheets with smooth surface. As shown in Fig. 3.1f, clear lattice fringes can be observed and the single crystalline nature of the nanosheet is revealed. The lattice spacing is about

0.276 nm as shown in the inset of Fig. 3.1f, which is consistent with the d-spacing of the (110) reflection for BiOBr. The selected area electron diffraction (SAED) analysis (Fig. 3.1g) confirms the high polycrystalline nature of BiOBr. Results of the energy dispersive X-ray (EDX) analysis (Fig. 3.1h) show the molar ratio of Bi:F to be 1.1:1. Carbon and copper are from the conducting tape and the sample holder. Besides, all the diffraction peaks of the product, shown in Fig. 3.2, match well with those of tetragonal-phase BiOBr (JCPDS File No. 09-0393). In this work, only an hour of reaction time is needed for the formation of highly crystallized BiOBr products. Prolonging the reaction time is not advised since the same products were obtained after 24 hrs of reaction. The high reaction efficiency is partly due to the hydrophilic characteristics and high dielectric constant ($\epsilon=11.7$) of the ionic liquid which can well support the dissolution of bismuth nitrate,³⁹ facilitating the nucleation of crystal growth and promote the formation of crystalline products. This is a significant improvement over the conventional solvothermal process which often requires very long reaction time (>12 h) due to the slow reaction kinetics.⁴⁰ This solution-based approach should be easily extended to large scale production of BiOBr mesocrystals.

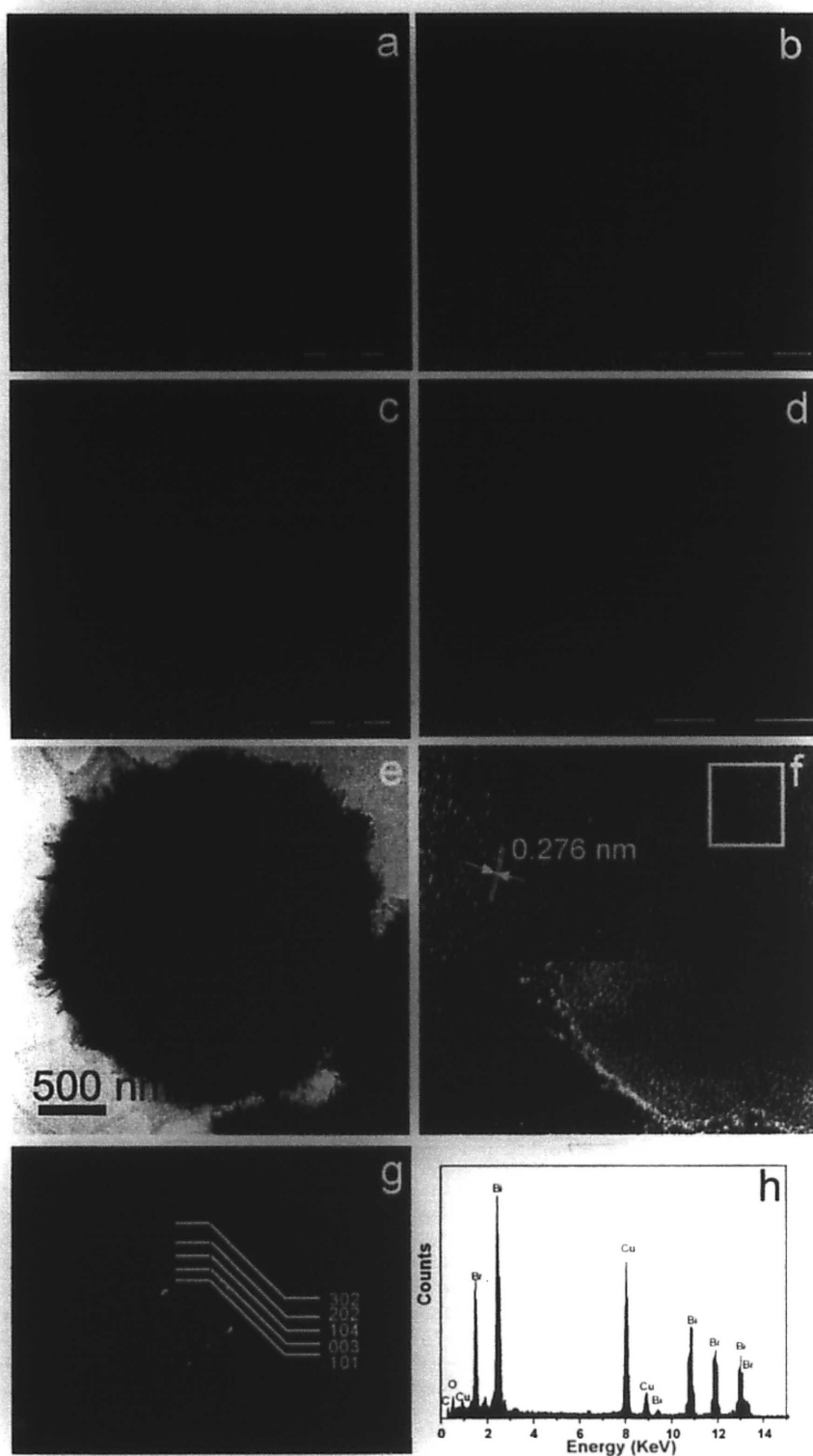


Figure 3.1 SEM images (a-d), TEM (e) and HTTEM (f) images, SAED (g) and EDX pattern (h) of BiOBr.

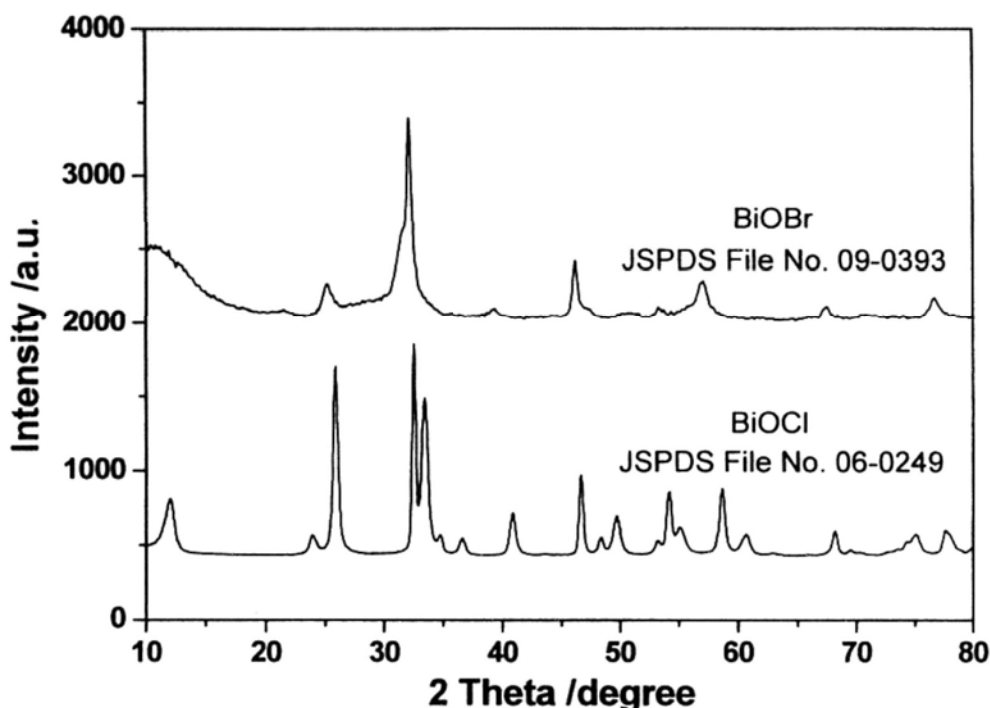


Figure 3.2 XRD patterns of as-prepared BiOX (X=Cl, Br) powders.

Ionic liquids are often considered “designer solvents” due to the unique variability of the ions. By changing the anion of 1-butyl-3-methyl-imidazolium from bromide to chloride, ternary bismuth oxide chloride can be prepared. Fig. 3.2 shows the XRD pattern of the BiOCl product. The diffraction peaks can be well indexed to the standard tetragonal phase of BiOCl (JSPDS File No. 06-0249). FESEM images and TEM image of the products (Fig. 3.3a, b and c) show the 3D marigold-like morphology similar to that of BiOBr. The open framework is also composed of interweaved nanosheets. The lattice spacing observed in the HRTEM image (Fig. 3.3d) is about 0.344 nm, which is consistent with the d-spacing of the (101) reflection.

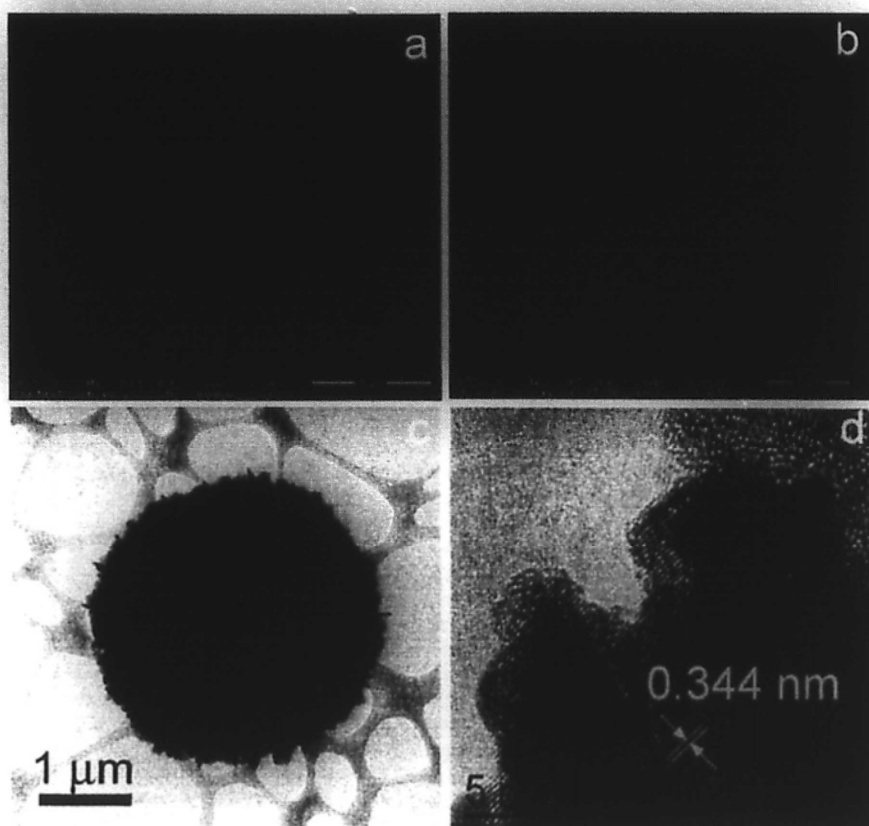


Figure 3.3 FESEM images (a, b) and TEM (c) and HRTEM images of BiOCl.

It is quite probable that imidazolium-based ILs form a complex with bismuth at an early stage of the reaction. The assumption is based on the mesocrystal transformation features in recent reports.⁴¹⁻⁴⁴ They indicate that primary nanoparticles are the building units that assemble into larger structures, forming mesocrystals by oriented attachment and fusion. We believe that the ILs distributed over the nanosheets surface play an important role in the determination of inter-nanosheet interaction leading a 3D assembly process to reduce the surface energy and transforming into a marigold-like 3D structure. Our results are consistent

with the previous work, where 1-butyl-3-methyl-imidazolium bromide (or chloride) supports three-dimensional (3D) alignment of silver nanoparticles.⁴⁴

3.3.2 N₂ Adsorption-Desorption Analysis

The specific surface area and porosity of the marigold-like BiOBr and BiOCl powders were measured from the nitrogen adsorption and desorption isotherms. The samples exhibit type-IV isotherms (Fig. 3.4, inset) which is typical for mesoporous solids. The BET specific surface area of the BiOBr and BiOCl samples calculated by the Brunauer–Emmett–Teller (BET) method are 14 and 10 m²/g. The samples contain small and large mesopores as shown in Fig. 3.4a and b, and the pore diameters are estimated by using the desorption branch of the isotherm. The small pores are from the nanosheets, while the large pores may be attributed to the open space from interweaving. The 3D BiOX mesocrystals possess both micro- and nano-structures, and can be a promising candidate for various applications in the field of environmental remediation.

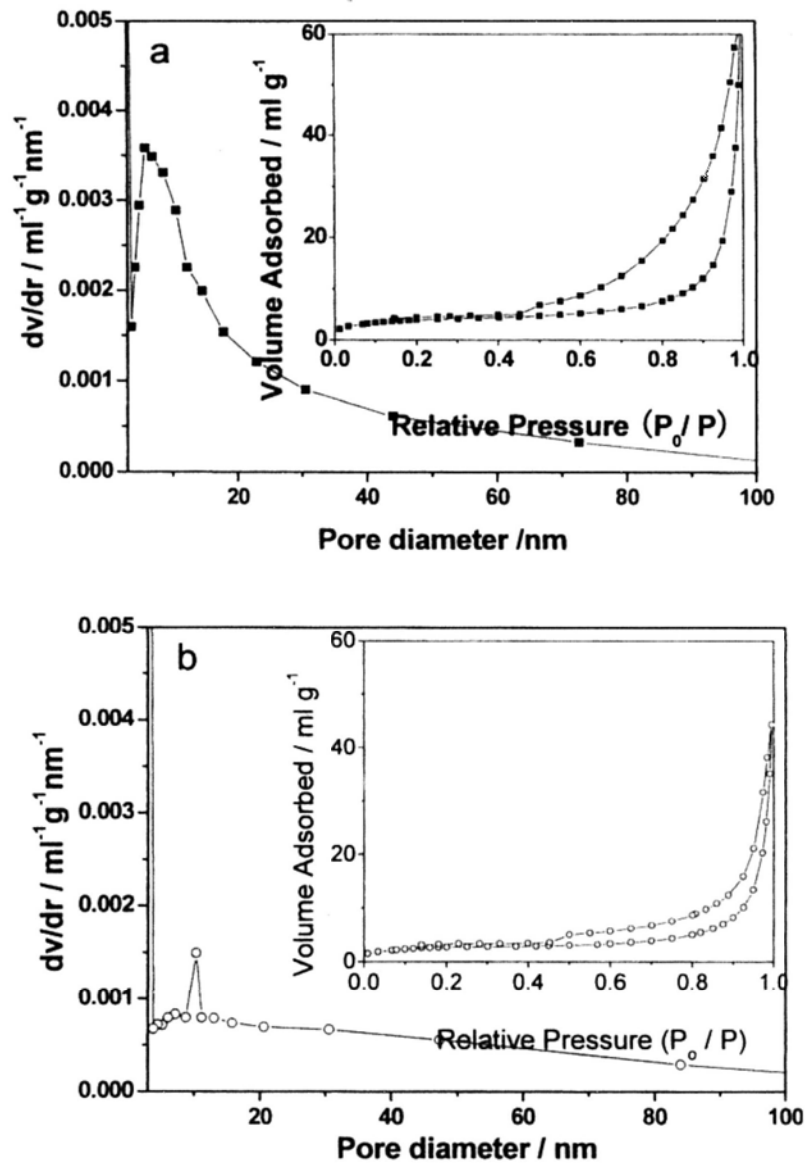


Figure 3.4 Pore-size distributions and N_2 adsorption and desorption isotherms (inset) for the BiOBr powders (a, \blacksquare -) and BiOCl (b, $-\circ-$) powders.

3.3.3 Photocatalytic Activity

The photocatalytic activity of the BiOBr powders was evaluated by the reaction of hydrogen (H_2) evolution from an aqueous solution of methanol. Commercial TiO_2 powder, P25 (Degussa), was used as a reference. A suspension of the photocatalyst powders and a small amount of hydrogen hexachloroplatinate (IV) (H_2PtCl_6) was

irradiated by a 300 W Xenon lamp with a 400 nm cut-off filter. Fig. 3.5a shows the photocatalytic H₂ evolution against time. The rate of H₂ evolution by BiOBr powders is higher than that of P25. The photocatalytic oxidative decomposition of organic dyes is also of fundamental importance in water treatment. Fig. 3.5b shows the changes in the methylene blue (MB) concentration versus reaction time under visible light irradiation. Prior to irradiation, the suspensions were stirred in the dark for 2 h to reach adsorption-desorption equilibrium. As a comparison, direct photocatalysis of MB was performed under identical conditions. We observed that direct photocatalysis of MB was negligible under visible light irradiation. The P25 photocatalyst is ineffective but the BiOBr product shows a high decomposition rate for methylene blue. The degradation of MB on 3D marigold-like BiOBr is about 61 % after 2 hrs.

3.3.4 Bactericidal Activity

The bactericidal activity of the BiOBr sample was evaluated by killing *M. lylae* in water under fluorescent light (commonly used for householding lighting, visible light intensity = 7.48 mW/cm²) irradiation on the basis of the decrease in the colony number of *M. lylae* formed on an agar plate. The fluorescent light photocatalytic disinfection is safe and cost effective as compared to disinfection using UV and

chlorine since the latter ones use hazardous irradiation and produce disinfection by-products in the process.⁴⁵ According to Fig. 3.5c, 50 % of *M. lylae* are killed in 180 min and only 10 % would survive after 360 min. However, BiOBr powder in the dark shows no bactericidal effects on *M. lylae*, indicating that the photocatalyst itself is not toxic to *M. lylae*. Thus, the bactericidal effect is ascribed to the photocatalytic reaction of BiOBr. Oxygen species such as hydroxyl radicals oxidized the cell membrane and damaged the microbial structure, causing various damages to living organism.^{46,47}

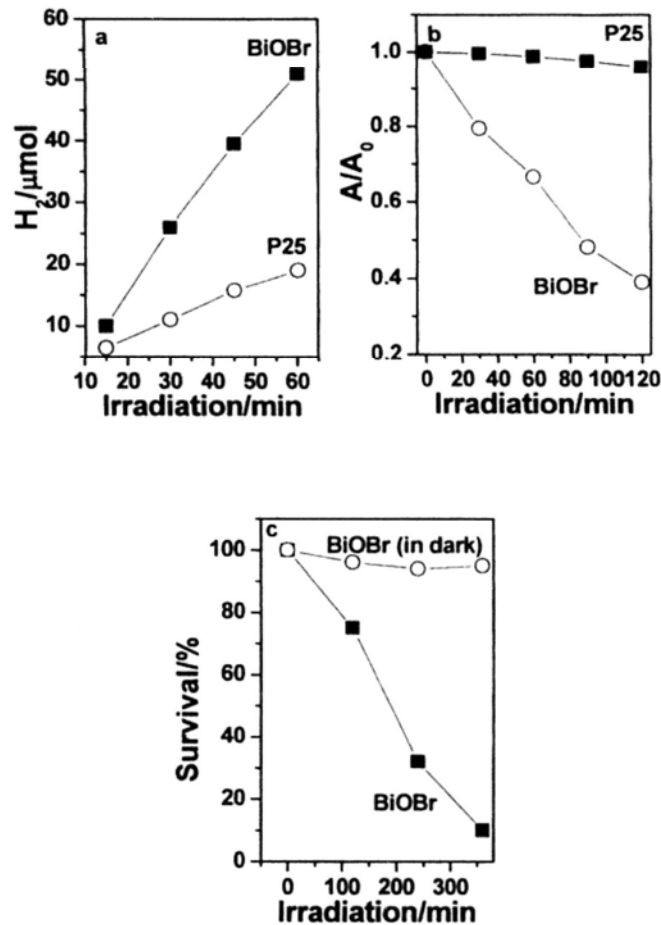


Figure 3.5 (a) Photocatalytic H₂ evolution from an aqueous solution of 20 vol % methanol containing BiOBr and P25 in the presence of H₂PtCl₆. (b) Photocatalytic oxidative decomposition of MB aqueous solution containing BiOBr and P25. (c) Survival ratio of *M. lylae* vs irradiation time for BiOBr powders.

The excellent photocatalytic performance in both water splitting and oxidative reactions for 3D BiOBr can be mainly attributed to its special physicochemical properties, such as a low band gap energy of 2.64 eV, a high surface to bulk ratio and open hierarchical structure.⁸ The low band gap energy makes it a promising photocatalyst for solar-driven applications. The high surface to bulk ratio will not only supply more active sites for the photocatalytic reaction, but also effectively

promote the separation efficiency of the electron-hole pairs.⁴⁸ Meanwhile, the light harvesting is also enhanced due to the open hierarchical structure and multiple scattering.⁴⁹ Chemical reactions are most effective when the transport paths through which molecules move into or out of the nanostructured materials are included as an integral part of the architectural design.⁵⁰ The 3D marigold-like BiOBr could be recycled easily after the reaction due to its relatively large size. SEM and XRD investigation showed that structure and the chemical composition were well maintained, indicating very good stability.

3.4 Conclusion

In a conclusion, imidazolium-based ionic liquids are efficient reagents for the fabrication of 3D marigold-like BiOBr and BiOCl mesocrystals. Owing to the high surface to bulk ratio, hierarchical structures and narrow band gap, the photocatalytic performance can be significantly improved compared to the P25. The details of the interplay between the ILs and the formation of BiOX materials remain to be determined, but our results raise the possibility of controlling the morphology by careful selection of ILs. This facile method may allow us to produce other metal halide plasmonic photocatalysts with 3D architectures, such as Ag/AgBr and Ag/AgCl.

3.5 References

- [1] Zhang, J.; Shi, F. J.; Lin, J.; Chen, D. F.; Gao, J. M.; Huang, Z. X.; Ding, X. X.; Tang, C. C. *Chem. Mater.* **2008**, *20*, 2937.
- [2] Zhang, K. L.; Liu, C. M.; Huang, F. Q.; Zheng, C.; Wang, W. D. *Appl. Catal. B* **2006**, *68*, 125.
- [3] Poznyak, S. K. *Electrochim. Acta* **1990**, *35*, 1941.
- [4] Henle, J.; Simon, P.; Frenzel, A.; Scholz, S.; Kaskel, S. *Chem. Mater.* **2007**, *19*, 366.
- [5] Wang, J. W.; Li, Y. D. *Chem. Commun.* **2003**, 2320.
- [6] Geng, J.; Hou, W. H.; Lv, Y. N.; Zhu, J. J.; Chen, H. Y. *Inorg. Chem.* **2005**, *44*, 8503.
- [7] Deng, Z. T.; Chen, D.; Peng, B.; Tang, F. Q. *Cryst. Growth. Des.* **2008**, *8*, 2995.
- [8] Zhang, X.; Zhang, Z. H.; Jia, F. L.; Zhang, L. Z. *J. Phys. Chem. C* **2008**, *112*, 747.
- [9] Earle, M. J.; McCormac, P. B.; Seddon, K. R. *Green Chem.* **1999**, *1*, 23.
- [10] Cole-Hamilton, D. J. *Science* **2003**, *299*, 1702.
- [11] Endres, F.; Bukowski, M.; Hempelmann, R.; Natter, H. *Angew. Chem. Inter. Ed.* **2003**, *42*, 3428.

- [12] Dai, S.; Ju, Y. H.; Gao, H. J.; Lin, J. S.; Pennycook, S. J.; Barnes, C. E. *Chem. Commun.* **2000**, 243.
- [13] Wang, Y.; Yang, H. *J. Am. Chem. Soc.* **2005**, *127*, 5316.
- [14] Zhao, D. B.; Fei, Z. F.; Ang, W. H.; Dyson, P. J. *Small* **2006**, *2*, 879.
- [15] Trewyn, B. G.; Whitman, C. M.; Lin, V. S. Y. *Nano Lett.* **2004**, *4*, 2139.
- [16] Antonietti, M.; Kuang, D.; Smarsly, B.; Zhou, Y. *Angew. Chem. Inter. Ed.* **2004**, *43*, 4988.
- [17] Qin, Y.; Song, Y.; Sun, N. J.; Zhao, N. N.; Li, M. X.; Qi, L. M. *Chem. Mater.* **2008**, *20*, 3965.
- [18] Ryu, H. J.; Sanchez, L.; Keul, H. A.; Raj, A.; Bockstaller, M. R. *Angew. Chem. Inter. Ed.* **2008**, *47*, 7639.
- [19] Scariot, M.; Silva, D. O.; Scholten, J. D.; Machado, G.; Teixeira, S. R.; Novak, M. A.; Ebeling, G.; Dupont, J. *Angew. Chem. Inter. Ed.* **2008**, *47*, 9075.
- [20] Ding, K. L.; Miao, Z. J.; Liu, Z. M.; Zhang, Z. F.; Han, B. X.; An, G. M.; Miao, S. D.; Xie, Y. *J. Am. Chem. Soc.* **2007**, *129*, 6362.
- [21] Nakashima, T.; Kimizuka, N. *J. Am. Chem. Soc.* **2003**, *125*, 6386.
- [22] Zhou, Y.; Antonietti, M. *J. Am. Chem. Soc.* **2003**, *125*, 14960.
- [23] Yang, L. X.; Zhu, Y. J.; Wang, W. W.; Tong, H.; Ruan, M. L. *J. Phys. Chem. B*, **2006**, *110*, 6609.

- [24] Jiang, J.; Yu, S. H.; Yao, W. T.; Ge, H.; Zhang, G. Z. *Chem. Mater.* **2005**, *17*, 6094.
- [25] Biswas, K.; Rao, C. N. R. *Chem. Eur. J.* **2007**, *13*, 6123.
- [26] Dattelbaum, A. M.; Baker, S. N.; Baker, G. A. *Chem. Commun.* **2005**, 939.
- [27] Attard, G. S.; Glyde, J. C.; Goltner, C. G. *Nature* **1995**, *378*, 366.
- [28] Zhou, Y.; Antonietti, M. *Adv. Mater.* **2003**, *15*, 1452.
- [29] Trewyn, B. G.; Whitman, C. M.; Lin, V. S. *Nano. Lett.* **2004**, *4*, 2139.
- [30] Lee, B.; Luo, H. M.; Yuan, C. Y.; Lin, J. S.; Dai, S. *Chem. Commun.* **2004**, 240.
- [31] Lee, B.; Im, H. J.; Luo, H. M.; Hagaman, E. W.; Dai, S. *Langmuir* **2005**, *21*, 5372.
- [32] Wang, W. W.; Zhu, Y. J. *Mater. Res. Bull.* **2005**, *40*, 1929.
- [33] Zhang, C.; Chen, J.; Zhou, Y. C.; Li, D. Q. *J. Phys. Chem. C* **2008**, *122*, 10083.
- [34] Du, J. M.; Liu, Z. M.; Li, Z. H.; Han, B. X.; Huang, Y.; Zhang, J. L. *Micropor. Mesopor. Mater.* **2005**, *83*, 145.
- [35] Recham, N.; Dupont, L.; Courty, M.; Djellab, K.; Larcher, D.; Armand, M.; Tarascon, J. M. *Chem. Mater.* **2009**, *21*, 1096.
- [36] Bühler, G.; Feldmann, C. *Angew. Chem. Inter. Ed.* **2006**, *45*, 4864.
- [37] Lee, J. S.; Wang, X. Q.; Luo, H. M.; Dai, S. *Adv. Mater.* **2010**, *22*, 1004.

- [38] Paraknowitsch, J. P.; Zhang, J.; Su, D. S.; Thomas, A.; Antonietti, M. *Adv. Mater.* **2010**, *22*, 87.
- [39] Weingärtner, H. *Angew. Chem. Inter. Ed.* **2008**, *47*, 654.
- [40] Hu, X. L.; Yu, J. C. *Adv. Funct. Mater.* **2008**, *18*, 880.
- [41] Cölfen, H.; Antonietti, M. *Angew. Chem. Int. Ed.* **2005**, *44*, 5576.
- [42] Wohlrab, S.; Pinna, N.; Antonietti, M.; Cölfen, H. *Chem. Eur. J.* **2005**, *11*, 2903.
- [43] Niederberger, M.; Cölfen, H. *Phys. Chem. Chem. Phys.* **2006**, *8*, 3271.
- [44] Kim, T. Y.; Kim, W. J.; Hong, S. H.; Kim, J. E.; Suh, K. S. *Angew. Chem. Int. Ed.* **2009**, *48*, 3806.
- [45] Shannon, M. A.; Bohn, P. W.; Elimelech, M.; Georgiadis, J. G.; Marinas, B. J.; Mayes, A. M. *Nature* **2008**, *452*, 301.
- [46] Leung, T. Y.; Chan, C. Y.; Hu, C.; Yu, J. C.; Wong, P. K. *Water Res.* **2008**, *42*, 4827.
- [47] Yu, J. C.; Ho, W. K.; Yu, J. G.; Yip, H. Y.; Wong, P. K.; Zhao, J. C. *Environ. Sci. Technol.* **2005**, *39*, 1175.
- [48] Li, S.; Zhang, D. Q.; Yu, J. C. *Chem. Mater.* **2008**, *20*, 3983.
- [49] Yu, J. C.; Wang, X. C.; Fu, X. Z. *Chem. Mater.* **2004**, *16*, 1523.
- [50] Bell, A. T. *Science* **2003**, *299*, 1688.

Chapter Four

Microwave-Assisted Architectural Control Synthesis of 3D CdS Structures

4.1 Introduction

The formation of patterns and shapes in the natural world has long been a source of fascination. Materials with various architectures attract much attention due to their unique physical and chemical properties. Remarkable progress has been made in the fabrication of nanomaterials such as 0 D nanoparticles, 1 D rods (wires, cables, tubes and belts) and 2 D/3 D dendrites (disks, flowers, mesopores).¹ Compared with the low-dimensional nanomaterials, complex 3D structures will offer the possibilities to probe potentially new phenomena arising from their 3D organization.^{2,3} As an important type II-VI semiconductor, with a room temperature bulk band gap of 2.4 eV, CdS is a promising functional material for photoelectric conversion in solar cells, in light-emitting diodes for flat-panel displays, lasers, thin film transistors, and in other optical devices based on its nonlinear properties.⁴ Over the past few years, tremendous effort has been made to control the shape of CdS nanocrystals.⁵⁻⁸ Those

synthetic methods usually give 1D CdS nanostructures. Only few approaches can lead to 3D CdS micropatterns.⁹ The shapes are restricted to sphere-based structures. They are important for understanding the formation of spherical CdS crystals and their potential applications of microelectronic devices. However, the successful synthesis of complex architectures of anisotropic 3D CdS with multiple secondary structures is difficult and remains a great challenge.

The application of microwave heating in synthetic chemistry has been a fast-growing area of research since the first report of microwave-assisted synthesis appeared in 1986.¹⁰ Microwave allows rapid volumetric heating, often reducing the reaction time by orders of magnitude. This opens up the possibility of realizing the reactions in a very short time with higher selectivity, yield, and energy efficiency compared to the conventional heating. Based on the one-pot solution-phase microwave-assisted hydrothermal route, we have reported the synthesis of alpha-Fe₂O₃ nanorings, hierarchically porous ZnIn₂S₄ submicrospheres, coaxial Ag/C nanocables and monodisperse alpha-Fe₂O₃ nanocrystals.¹¹ In this work, we describe a fast and economical microwave-assisted solvothermal process for fabricating novel 3D CdS structures (dendrites, stars, popcorns and spheres). To the best of our knowledge, this kind of hierarchically self-assembled growth of CdS with well-defined 3D shapes by a microwave-assisted process has never been reported.

The CdS products exhibit interesting shape-dependent UV-vis, PL and Raman properties and photocatalytic activities.

4.2 Experimental Section

4.2.1 Chemicals

Cadmium nitrate ($\text{Cd}(\text{NO}_3)_2 \cdot 4\text{H}_2\text{O}$), ethylene glycol ($\text{HOCH}_2\text{CH}_2\text{OH}$) and thiourea ($\text{CH}_4\text{N}_2\text{S}$) were purchased from Aldrich. Triblock copolymer F108 ($\text{EO}_{132}\text{PO}_{50}\text{EO}_{132}$) was purchased from Fluka.

4.2.2 Preparation

For the synthesis of dendrite-like CdS, $\text{Cd}(\text{NO}_3)_2 \cdot 4\text{H}_2\text{O}$ (0.62 g, 2 mmol), $\text{CH}_4\text{N}_2\text{S}$ (0.4 g, 5 mmol) and triblock copolymer F108 (3 g, 0.2 mmol) were dissolved in distilled water (15 mL) at 60 °C under vigorous stirring until homogeneous. The mixture was sealed in a Teflon-lined double-walled digestion vessel. The mixture was treated at a certain temperature for 30 min in a microwave digestion system (Ethos TC, Milestone). The reaction vessel was fitted with a temperature probe that was housed in a sturdy thermowell. The desired time and temperature were programmed by using Milestone's EasyControl software. The temperature of the bulk reaction solution was monitored, and the preset profile was followed automatically by continuously adjusting

the applied power. After the reaction the product was collected through centrifugation. Then the yellow precipitates were washed by ethanol and water eight times in order to wash out triblock copolymer and then dried in vacuum at 60 °C for 4 h.

For other morphologies of CdS crystals, a similar synthetic procedure was deployed except that the conditions were varied, such as adding a co-solvent (ethylene glycol) and changing the reaction temperatures and duration. The detailed conditions for preparing some typical samples are listed in Table 4.1.

Table 4.1 Summaries of the experimental results indicating the influence of the composition of a mixed solution on the shape of the product.

| Sample ^a | T (°C) | V _{EG} /V _{WATER} | Time (min) | Morphology |
|---------------------|--------|-------------------------------------|------------|---------------|
| 1 | 190 | 0:1 | 30 | Dendritic |
| 2 | 190 | 1:1 | 30 | star-like |
| 3 | 190 | 9:1 | 30 | popcorn-like |
| 4 | 160 | 0:1 | 30 | Sphere-like |
| 5 | 160 | 1:1 | 30 | Sphere-like |
| 6 | 160 | 9:1 | 30 | popcorn-like |
| 7 | 130 | 0:1 | 30 | Sphere-like |
| 8 | 130 | 1:1 | 30 | Sphere-like |
| 9 | 130 | 9:1 | 30 | popcorn-like |
| 10 | 190 | 0:1 | 1 | Nanoparticles |
| 11 | 190 | 0:1 | 10 | Sphere-like |
| 12 | 190 | 0:1 | 20 | Dendritic |

^a reagents: 2 mmol Cd(NO₃)₂·4H₂O, 5 mmol CH₄N₂S, 0.2 mmol F 108, 15 mL H₂O.

4.2.3 Photocatalytic Activity Test

The photocatalytic degradation of aqueous methylene blue was carried out in an aqueous solution at ambient temperature. Briefly, the reaction system containing methylene blue (Sigma-Aldrich Chemical Co.; 5×10^{-5} M, 20 mL) and the CdS crystals (10 mg) was magnetically stirred in the dark for 1 hr to reach the adsorption/desorption equilibrium and then exposed to a commercial high-pressure Hg lamp (125 W, Philips). Commercial TiO₂ (Degussa P25) was used as the reference to compare the activities under the same experimental conditions.

4.2.4 Characterization

X-ray diffraction measurements (XRD) were carried out in a parallel mode ($\omega = 0.5^\circ$, 2θ from 20° to 80°) at a scanning rate of $0.02^\circ \cdot \text{s}^{-1}$ using a Bruker D8 Advance X-ray diffractometer (Cu K α radiation, $\lambda = 1.5406 \text{ \AA}$). The general morphology of the products was characterized by scanning electron microscopy (SEM, LEO, 1450VP). The products were conductively coated with gold by sputtering for 45 s to minimize charging effects using SEM image conditions. FESEM imaging was performed on a FEI Quanta 400 FEG microscope. Standard transmission electron microscopy (TEM) images were recorded using a CM-120 microscope (Philips, 120 kV) coupled with an energy-dispersive X-ray (EDX)

spectrometer (Oxford Instrument). High-resolution transmission electron microscopy (HRTEM) was recorded by a JEOL-2010F microscope at 200 kV. The electron microscopy samples were recorded prepared by grinding and dispersing the powder in acetone with ultrasonication for 20 seconds. Carbon-coated copper grids were used as sample holders. X-ray photoelectron spectroscopy (XPS) measurement was done with a PHI Quantum 2000 XPS system with a monochromatic Al-K α source and a charge neutralizer. All the binding energies were referenced to the C1s peak at 284.8 eV of the surface adventitious carbon. Raman spectra were detected by a RenishawRM3000 Micro-Raman system. Photoluminescence (PL) spectra were recorded with a Hitachi F-4500 spectrophotometer equipment with a 150 W xenon lamp as the excitation source. The operation parameters of PL test are the followings: scan speed = 240 nm/min, delay = 0 s, EX slit = 2.5 nm, EM slit = 2.5 nm, and the PMT voltage = 700 V. All the measurements were performed at room temperature. UV-vis diffuse reflectance spectra (DRS) were recorded by a Varian Cary 100 Scan UV-vis system equipped with a Labsphere diffuse reflectance accessory.

4.3 Results and Discussion

4.3.1 XRD and XPS Analysis

The wide-angle powder X-ray diffraction (XRD) pattern of sample 1 was shown in Fig. 4.1a. All the diffraction peaks can be indexed to pure hexagonal structure CdS with lattice constants of $a = 4.14 \text{ \AA}$ and $c = 6.72 \text{ \AA}$, which are consistent with the data in the standard card (JSPDS Card No.41-1049). The significant sharp and narrowed (002) peak at 26.5° (2θ) clearly supports the extended c-axis stacking domain of the wurtzite lattice.^{12, 13} The composition and the purity of the product were examined by XPS. The typical survey spectrum (Fig. 4.1b) of sample 1 shows clearly the presence of Cd and S elements. The C peak and O peak are due to the absorbed impurity gas molecules. Higher resolution spectra were taken in the Cd and S regions as shown in Fig. 4.1c and d. The strong peaks at 405.3, 412.5 and 161.6 eV are attributed to the binding energy of the Cd 3d electrons and S 2p electrons of the CdS crystals. The ratio of integral area for Cd 3d to S 2p is about 1.00:1.06, which was close to stoichiometric ratio of CdS. These results are similar to those previously reported.¹⁴

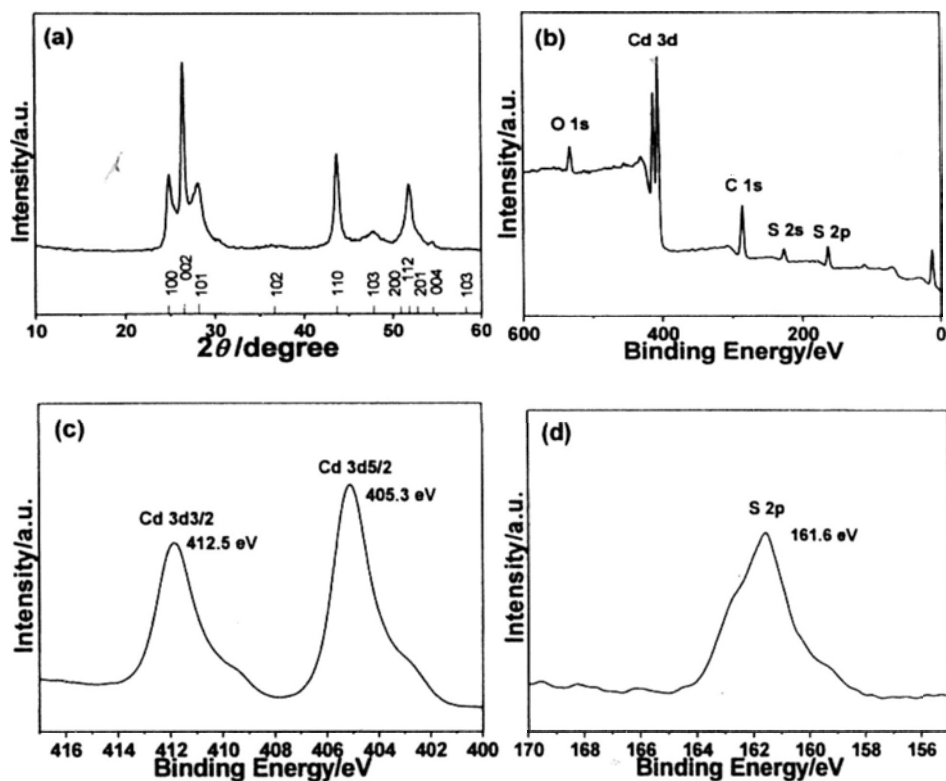


Figure 4.1 XRD pattern (a), Survey XPS spectrum (b), High-resolution XPS Cd 3d spectrum (c) and S 2p spectrum (d) of sample 1.

4.3.2 SEM, TEM and EDX Analysis

It is composed of a large quantity of dendritic CdS microcrystals with lengths up to 4 μm . Fig. 4.2b shows the morphology of the product at a higher magnification, indicating these CdS dendritic crystals with asymmetric trunks and branches. Many nanorods growing from the trunks with particular angles constitute the multiple branch arrays. TEM and HRTEM images provide further insight into the microstructure of the product. Fig. 4.2c displays the representative bright-field TEM images of sample 1, showing a well defined dendritic morphology. The high-resolution TEM image (Fig. 4.2d) recorded on the tip of the nanorod confirms the single-crystal nature and the

preferential [001] direction growth, which is similar to the results reported by Qian et al.¹⁵ The measured interplanar distance is in agreement with the typical hexagonal CdS (002) fringe (0.67 nm),¹⁶ which further indicates that the CdS dendrites grow along the direction of c-axis. The EDX analysis (Fig. 4.2e) shows the products are composed of Cd and S elements without other impurities. The average atomic ratio of Cd to S is 1.00:1.05, which is in good agreement with the XPS results.

It is well known that the shape of the crystals is determined by both thermodynamic and kinetic factors. The equilibrium morphology always has the lowest surface energy from the thermodynamic view. However, by tuning the kinetic factors, the equilibrium morphology can be changed.¹⁷

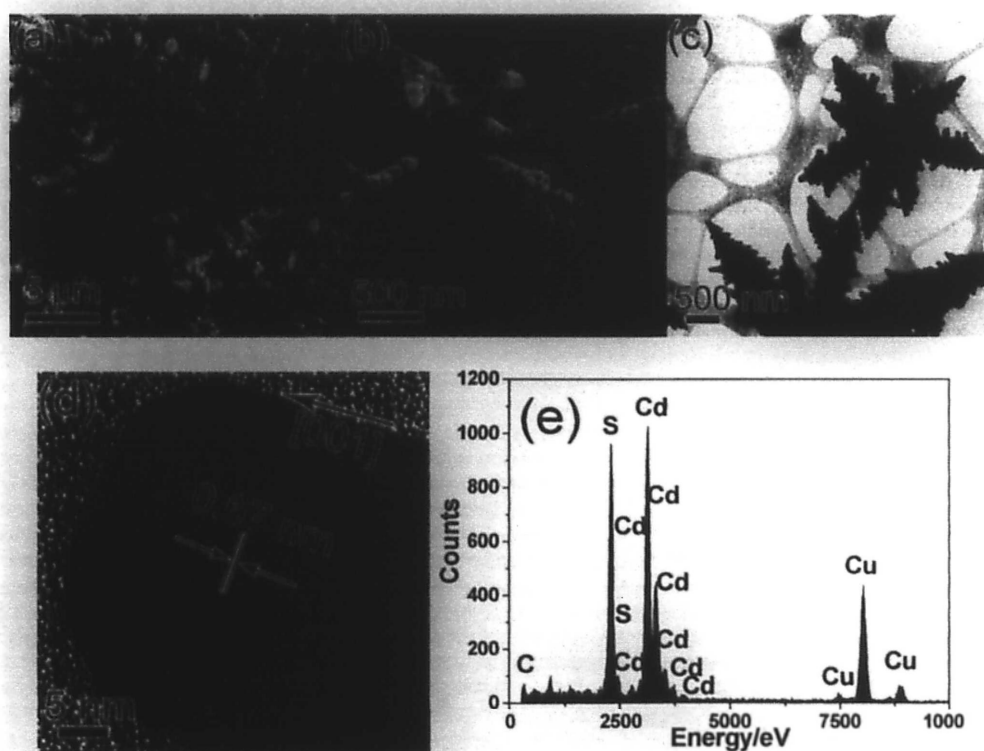


Figure 4.2 FESEM images (a and b) and TEM image (c) of sample 1. HRTEM image (d) recorded on the tip of the nanorod. EDX spectrum (e) of sample 1. The signal of Cu is generated from the Cu grids.

4.3.3 Solvent-Induced Morphology Variation

EG was selected as the co-solvent based on its high permanent dipole (2.45 GHz) and higher boiling point (197 °C), and it served as an excellent susceptor of the microwave radiation.^{17b} After adding EG into the reaction system the morphology of the products varied as the volume ratio of EG/water changed from 0:1, 1:1 to 9:1 while keeping the other parameters constant. The detailed conditions for preparing the following materials are listed in Table 4.1. At a volume ratio of 1:1 (EG/water), the products (sample 2) are 3D star-like CdS crystals as shown by the SEM image (Fig. 4.3a). The fine structure information was further revealed by the TEM image (Fig. 4.3b). Unlike with the dendritic CdS, the individual star-like CdS with smaller crystal size has many petals without secondary or tertiary side-branches. The petals grow from the centre of the CdS crystals, like a blossoming flower. By further increasing the ratio of EG/water to 9:1 with the other parameters kept unchanged, popcorn-like 3D CdS crystals (sample 3) were formed (shown by Fig. 4.3c, 4.3d). A lot of small tubers exist on the surface without many branches or petals. This method provides an efficient way for selectively fabrication of 3D hierarchical CdS crystals with different morphologies. The novel morphologies demonstrate that the solvent has a great influence on the shape of the products. Similar results of solvent-dependent effect on the morphology formation have been reported by Qian et al.¹⁵

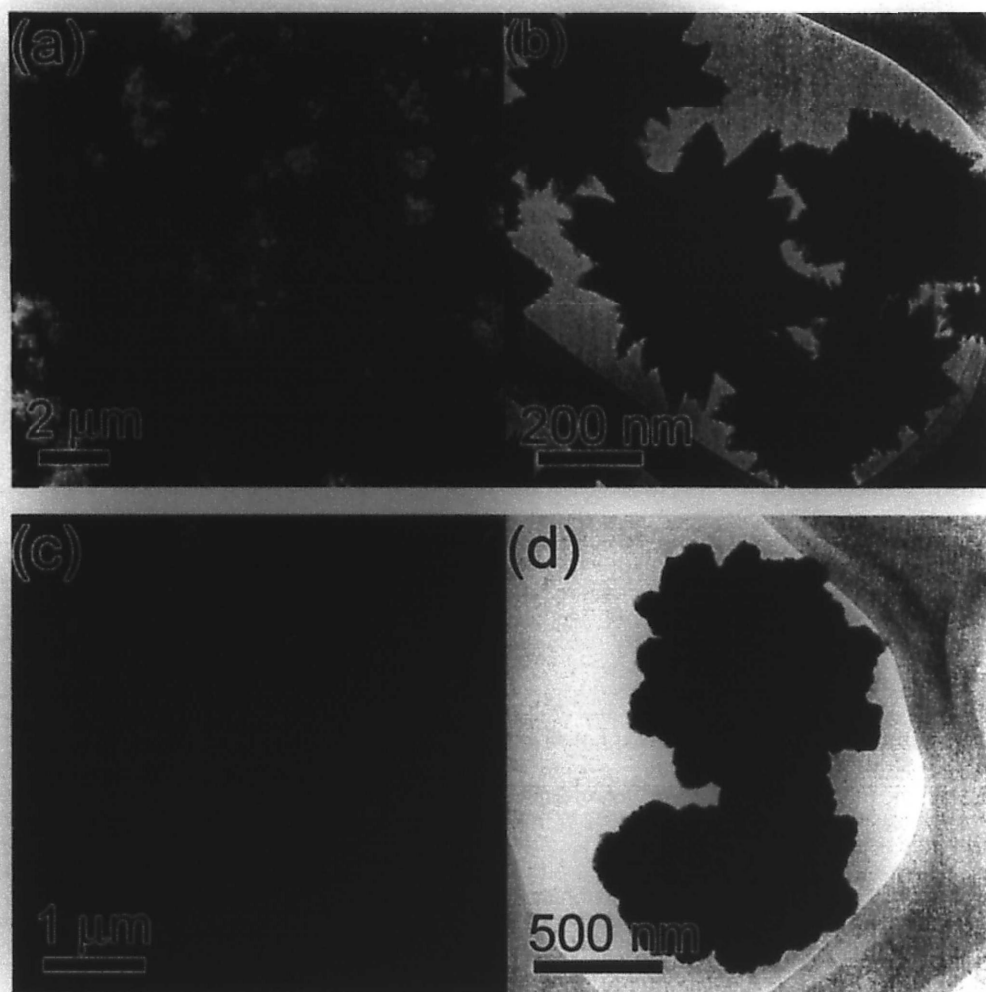


Figure 4.3 FESEM and TEM images of sample 2 (a and b) and sample 3 (c and d).

4.3.4 Reaction Temperature-Induced Morphology Variation

As known, the reaction temperature plays an important role in the formation of crystal structure, shape and size.¹⁸ For systematic study, different samples were prepared under 160 °C and 130 °C microwave irradiation using various volume ratios of EG/water (listed in Table 4.1). It can be seen from the SEM images (Fig. 4.4) that most of the particles are spherical in shape (sample 4, 5, 7, 8). Under high concentration of EG (sample 6 and 9), popcorn-like particles with rough surfaces were

obtained (Fig. 4.4c, f). The FESEM image (Fig. 4.5a) of sample 8 obtained at 130 °C (EG/water = 1:1) shows a large quantity of monodisperse sphere-like CdS nanocrystals with smaller particle size (ca. 200-250 nm). The TEM image (Fig. 4.5b) reveals that these spheres are hollow in its interior. These results suggest that it is possible to control the architecture of the CdS crystals by choosing different reaction temperatures.

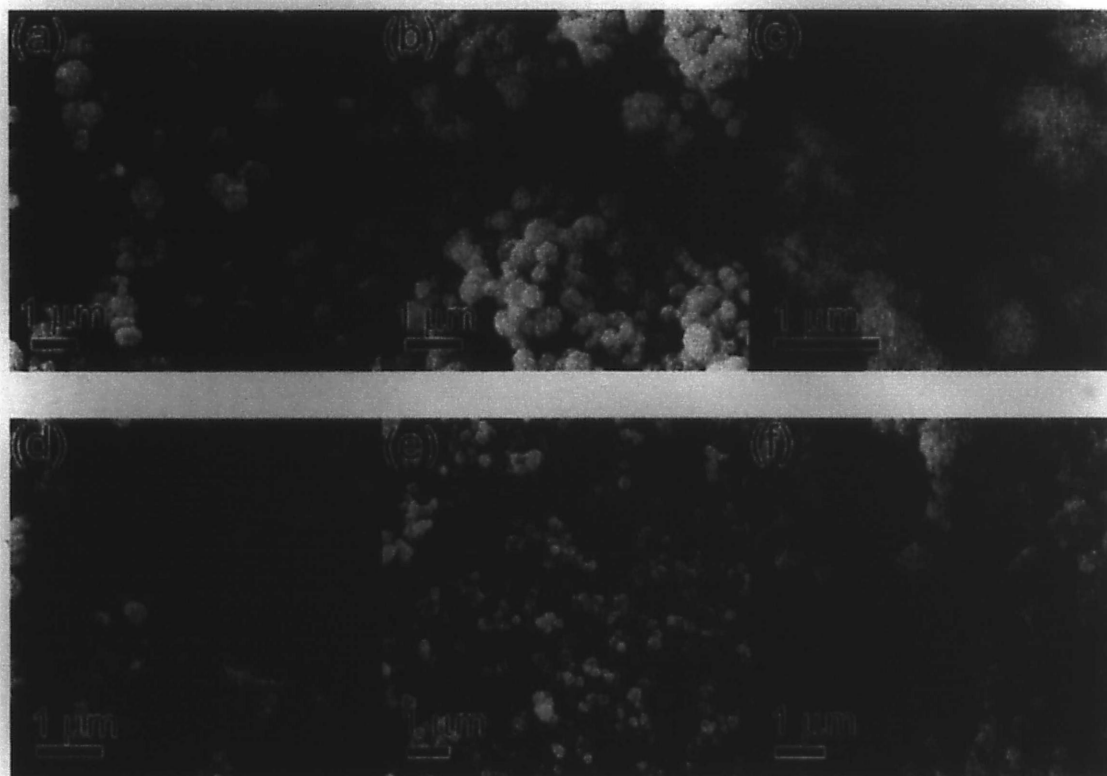


Figure 4.4 SEM images of the samples obtained by different volume ratios of EG/water at different temperature: (a) 0:1, 160 °C (sample 4), (b) 1:1, 160 °C (sample 5), (c) 9:1, 160 °C (sample 6), (d) 0:1, 130 °C (sample 7), (e) 1:1, 130 °C (sample 8), (f) 9:1, 130 °C (sample 9).

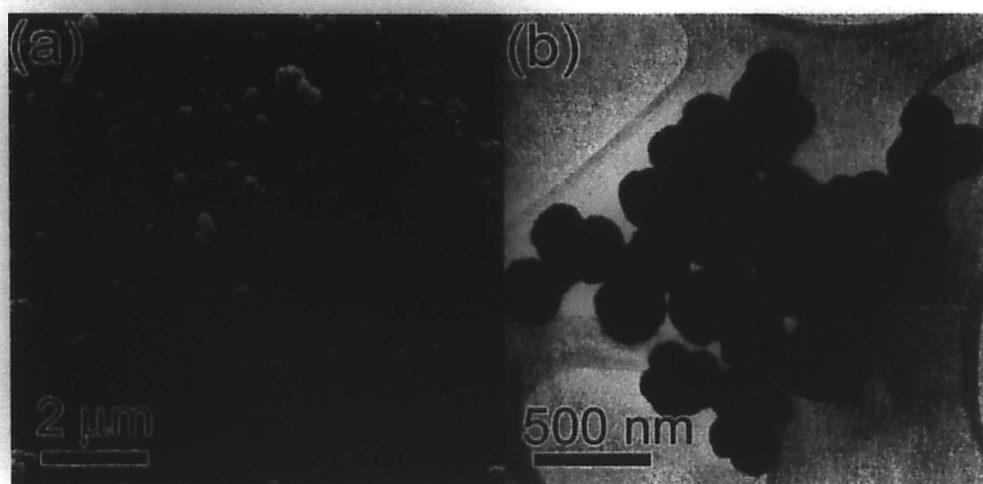


Figure 4.5 FESEM (a) and TEM images (b) of sample 8.

4.3.5 Reaction Time-Induced Morphology Variation

To explore the shape evolution of CdS crystals with the microwave irradiation time, the dendrite-like CdS growth process was studied. Under microwave irradiation at 190 °C for 1, 10, 20, and 30 min, respectively, different morphologies of CdS crystals were obtained. For 1 min a great number of uniform nanocrystals (shown by Fig. 4.6a, sample 10) with small particle size (300-400 nm) were formed. By prolonging the heating time to 10 min, the sphere-like crystals with some bulges on the surface appeared (shown by Fig. 4.6b, sample 11). The particle size continued to increase with longer reaction time. The more perfect crystal with side-branches appeared after 20 min irradiation (shown by Fig. 4.6c, sample 12). The hierarchical dendrite-like CdS crystals with superstructures were finally obtained (Fig. 4.6d, sample 1) after 30 min reaction. The efficiency of the shape control in the reaction system was further

supported by the XRD results (Fig. 4.7). Even for 1 min irradiation, the wurtzite CdS crystals could be obtained. Upon prolonging the irradiation time, the crystallinity was quickly enhanced within 30 min.

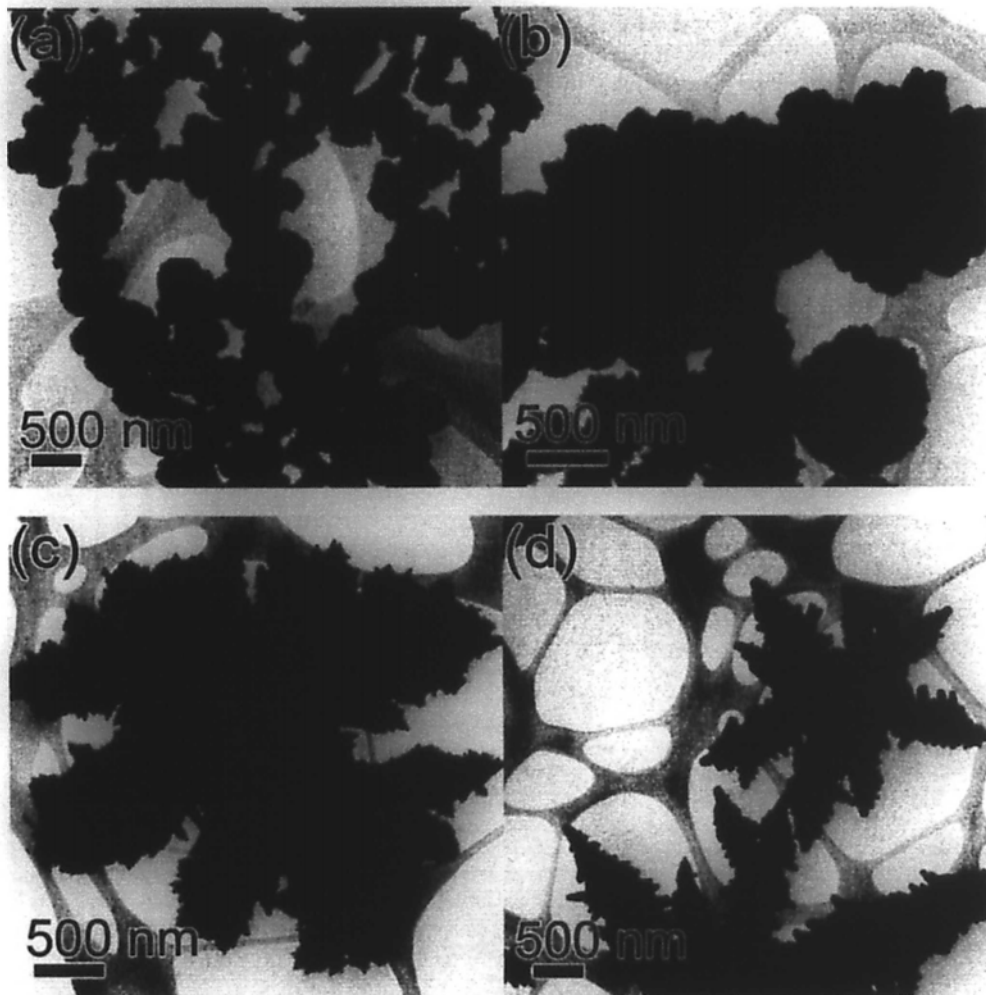


Figure 4.6 TEM images of the products prepared at 190 °C with various microwave irradiation time: (a) 1 min (sample 10), (b) 10 min (sample 11), (c) 20 min (sample 12), (d) 30 min (sample 1).

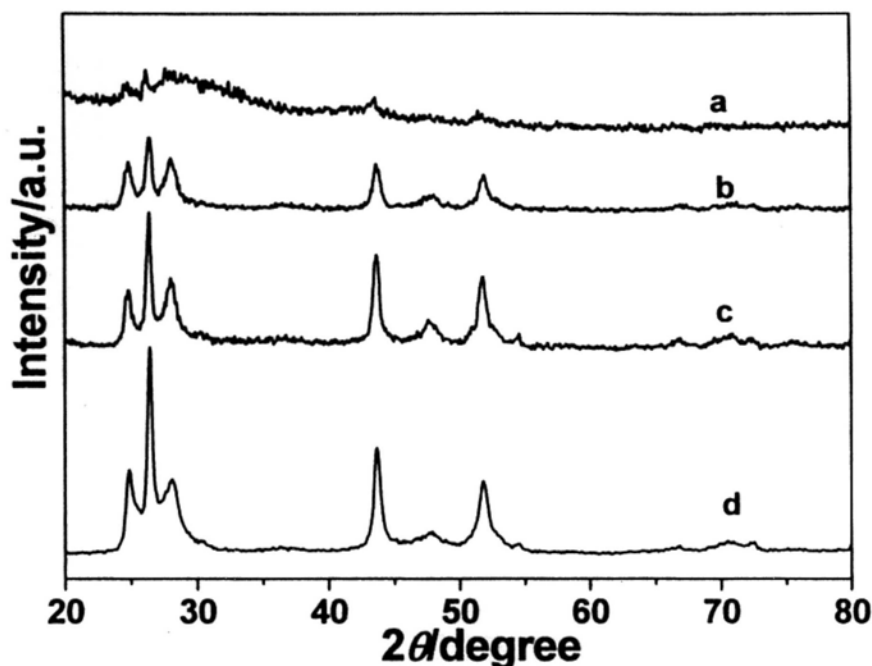


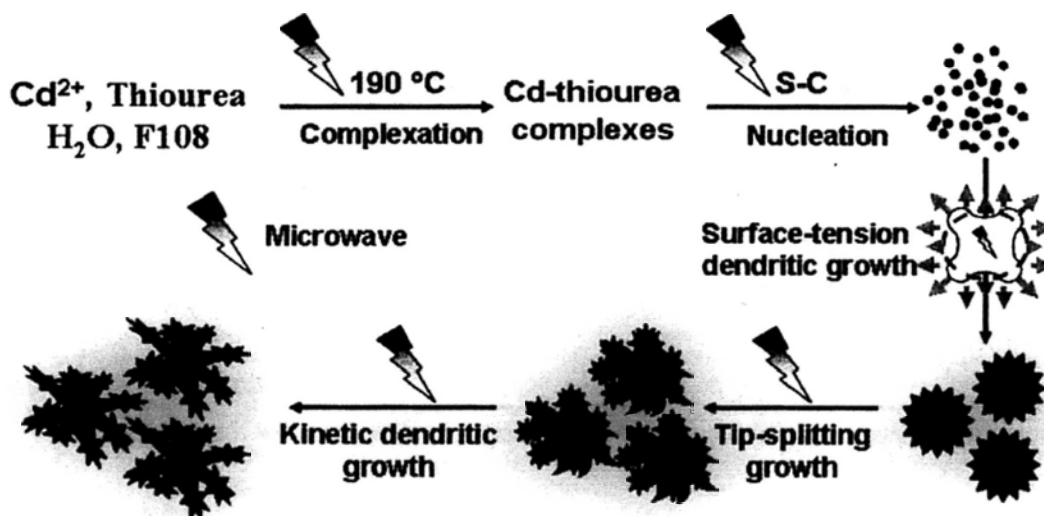
Figure 4.7 XRD patterns of CdS crystals obtained at 190 °C for (a) 1 min (sample 10), (b) 10 min (sample 11), (c) 20 min (sample 12) and (d) 30 min (sample 1).

4.3.6 Growth Mechanism

On the basis of the experimental results, a possible growth process of dendritic CdS crystals was illustrated in Scheme 4.1. Thiourea serves as both a sulfur source and a bidentate ligand to form a relatively stable Cd-thiourea complex.^{9b} The S-C bond of thiourea can be broken at a high temperature and pressure in the microwave process. The resulting sulfide ions will further react with cadmium ions to produce the CdS nuclei. Subsequently, these free nuclei in the solution will aggregate together to form sphere-like nanocrystals (Fig. 4.6a), driven by minimization of surface energy and H-bond interaction. Such phenomenon is similar to that reported by Zhang et al.¹⁹ It is well known that fractal and dendritic growths are diffusion-controlled growths.

Nonequilibrium growth and molecular anisotropy are the prerequisites for the formation of the dendritic structure.²⁰ In the current close reaction system, H₂S gas can be continuously generated due to the decomposition of the excess thiourea. The pressure in the close reaction system will be increased by prolonging the reaction time. It is well known that a key macroscopic effect of the pressure field at the interface is the diffusive instability,²¹ illustrated in Scheme 4.1. An interface is initially circular but developed into a bulge. The pressure gradient along the surface is the greatest at the tip of the bulge because it is the closest point on the interface to the outer boundary. Since the velocity of a point on the interface is proportional to the local pressure gradient, the bulge grows faster than other parts of the interface. Furthermore, for the highly anisotropic wurtzite CdS structure, the growth rate is generally faster along the c-axis [001] direction due to the intrinsic structure of CdS. As a result, an oriented growth along the [001] direction takes place on the surface of the sphere-like particles (Fig. 4.6b). This process can be considered as the surface-tension dendritic growth. It can be explained by the diffuse instability resulted from a key macroscopic effect of the pressure field at the interface.²⁰ Meanwhile, the microwave in the diffusion field causes the interface to break up into many growing bulges (Fig 4.6c). Such process can be considered as the tip-splitting growth. However, when excess thermal energy is supplied to the reaction system by microwave heating over 30 min, the growth process

appears to shift into the thermodynamic regime, the dendrite-like CdS with secondary or tertiary side-branches on its trunks appears. This step can be called a kinetic dendritic growth. The growth process was shown in Scheme 4.1.



Scheme 4.1 Proposed growth process for dendritic CdS crystals (sample 1).

By changing the volume ratio of EG/ H_2O , the CdS morphology changed. For the shape evolution from dendrite-like to star- and popcorn-like CdS crystals, the microscopic dynamics occurring at the interface (determined by surface tension, surface kinetics and anisotropy) are associated with its morphology. Previous studies pointed out that the surface tension and surface kinetics were singular perturbations in the dynamical equation for interface evolution, in the sense that surface tension may totally alter the character of the solutions.²² Comparing the surface tension of water (72.8 mN/m, 20 °C), EG has a relatively low value of 47.7 mN/m. A plausible explanation for the morphology evolution can be attributed to the decrease of surface

tension in the reaction system. Furthermore, the viscosity increases with the higher EG concentration. The viscosity may cause the diffusion of ions more difficult and suppress the anisotropic growth of CdS crystals. From this point of view, we can conclude that adding EG will affect the surface-tension dendritic growth and lead to different morphologies. Such explanation is in agreement with the experimental observations.

A qualitative model that related growth habit and supersaturation for growing PbS single crystals has been established by Sunagawa in 1981.²³ High supersaturation causes the three-dimensional growth of preformed nuclei and results in the formation of dendritic structure. Decreasing the supersaturation favors the formation of thermodynamically preferred structure. Similar results have also been observed in the shape control of CdSe and other semiconductors by Peng et.al.²⁴ In the present work, dendritic CdS could be obtained upon increasing the temperature to 190 °C. This is because high temperature heating could accelerate the release of sulfide ions from thiourea into the reaction system, resulting a higher degree of CdS supersaturation due to an excess amount of dissolved cadmium ions in the system. However, at a lower temperature such as 160 °C or 130 °C, spherical CdS crystals were obtained owing to less available sulfide ions and the decreased supersaturation degree of CdS. Such

relationship between the supersaturation and morphologies can explain why various morphologies of CdS crystals can be fabricated under different reaction temperatures.

4.3.7 Spectroscopic Study

The optical properties of different CdS nanostructures have attracted significant attention recently.²⁵ UV-vis absorption spectrometry is a useful technique to probe shape-specific localized surface plasmas in the optical frequencies.²⁶ Yang et al. recorded the extinction spectra for colloidal suspensions of cubes, cuboctahedra and octahedral structures and found highly complex plasmon signatures as a result of their geometric anisotropy.²⁶ Thus, the CdS crystals with different morphologies offer a good opportunity to systematically study their optical properties. From the UV-vis spectra (Fig. 4.8a), the absorption peaks for dendrite-, star- and popcorn-like CdS crystals are located at 518 , 515 and 503 nm. The blue-shifts from the bulk band gap value of CdS (520 nm) are due to the quantum confinement effect.²⁷ Fig. 4.8b shows the room-temperature photoluminescence spectra of the different samples. Each curve exhibits two peaks. The one at 500-550 nm is the green emission component. The other at about 695 nm is the infrared band. These results are similar to those reported for CdS nanocrystals.¹⁵ The green luminescence is usually attributed to the near-band-edge (NBE) emission, where the latter (the infrared emission) can be

associated with structural defects that may result from the trap or surface states.¹⁵

The broad PL peak observed is commonly attributed to the recombination of charged carriers trapped in the surface states and is related to the size of the CdS crystals.²⁸

Blue-shifted by about 15 nm from dendrite-like sample to popcorn-like sample may be

relevant to the diversity of 3D morphologies, which is similar to that of previous reported.¹⁵ These results suggest that the shape can affect the peak frequencies and

widths. Raman spectroscopy of semiconductors is a fast and non-destructive tool to reveal the quality of crystalline materials, including surface conditions and homogeneity.²⁹ The CdS samples with different morphologies exhibit similar Raman

spectra, showing the two typical LO (longitudinal optical phonon) modes (Fig. 4.8c).

The Raman peaks of dendrite-like CdS appear at 297 cm^{-1} , attributed to the A₁ (LO) mode with a full width at half maximum (FWHM) of ca. 20.3 cm^{-1} and its overtone at

596 cm^{-1} .³⁰ The Raman peaks are blue-shifted to 301 cm^{-1} , 602 cm^{-1} and 302 cm^{-1} , 607 cm^{-1} for the flower-like and popcorn-like CdS, respectively. We know that in a

crystalline semiconductor or insulator the observed Raman shifts usually correspond to

the LOs, whereas other modes such as the transverse optical and surface phonon

modes are not observable because of symmetry restrictions and their low intensities.³¹

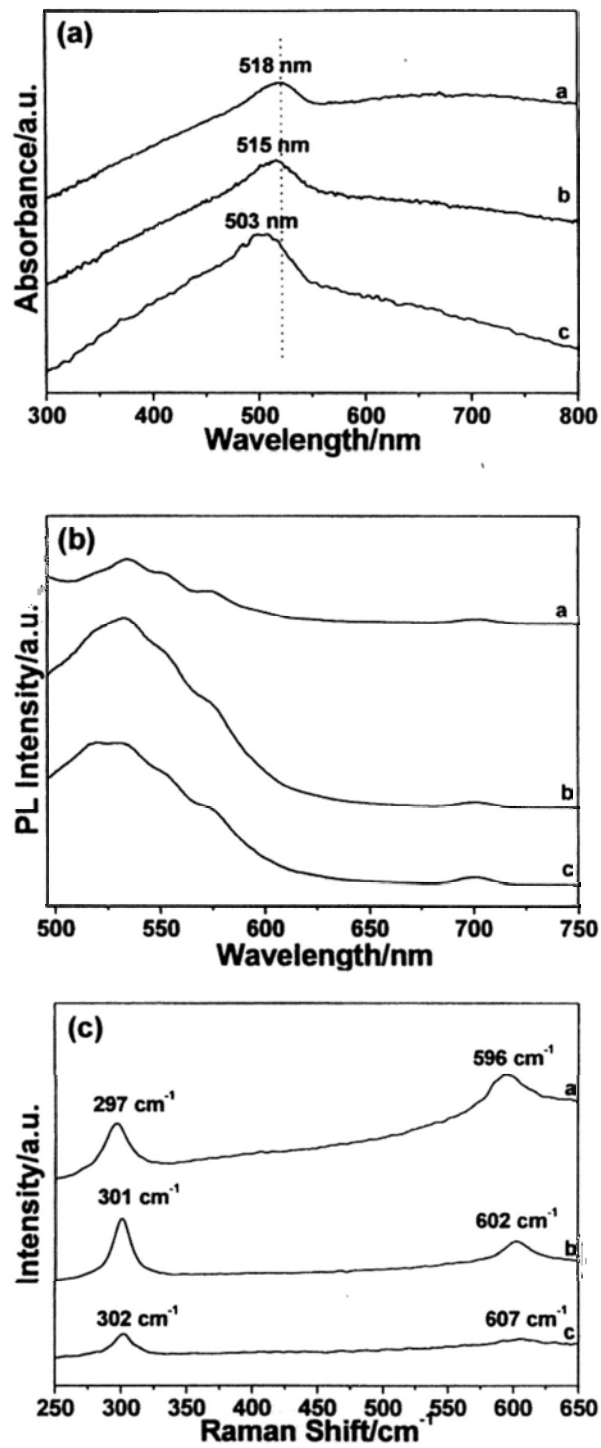


Figure 4.8 UV-vis (a), PL (b) and Raman spectra (c) of sample 1, 2, 3 (line a, b, c).

4.3.8 Photocatalytic Activity

Further experiments were performed to compare the photocatalytic activity of the dendrite-, star-, popcorn-, sphere-like CdS crystals and the commercial P25 (Degussa).

The photocatalytic activities were measured in the liquid phase. The decomposition of methylene blue (5×10^{-5} M, 20 mL) in an aqueous solution was chosen as a photoreaction probe. Fig. 4.9 shows the degradation rates of both dendrite- and star-like CdS products are higher than that of commercial P25 (Degussa), popcorn- and sphere-like CdS crystals under the irradiation of UV light. The photocatalytic degradation velocity of the P25 is slow at first, and gradually increases with the reaction time. However, the photocatalytic degradation rate of both dendrite- and star-like CdS is fast at first. This is because the hierarchical structures may be favorable for the fast adsorption of methylene blue on the surface of dendrite- and star-like CdS crystals. As a result, the hierarchical structure can provide more reactive adsorption/desorption sites for photocatalytic reaction.

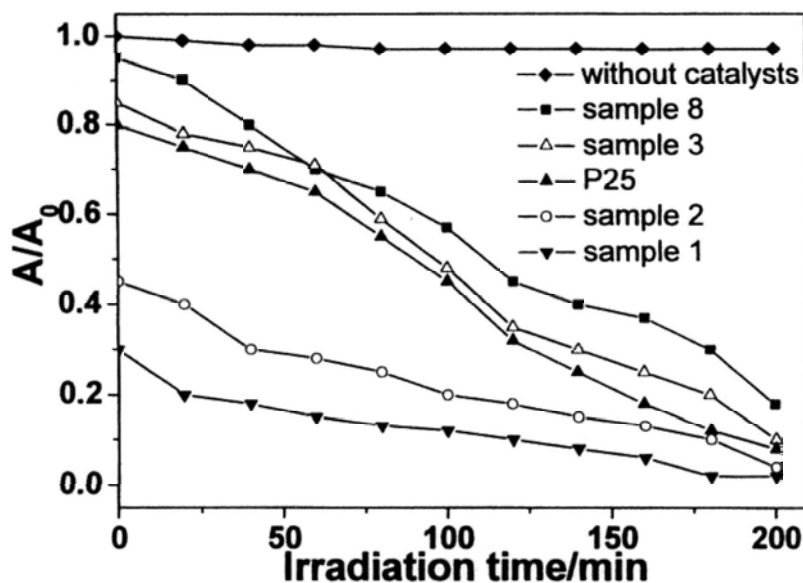


Figure 4.9 A comparison of the photoactivities of dendrite-like (sample 1, \blacktriangledown), star-like (sample 2, \circ), popcorn-like (sample 3, \triangle), sphere-like (sample 8, \blacksquare), P25 (Degussa, \blacktriangle) and without photocatalysts (\blacklozenge). A is the absorbance of methylene blue ($\lambda_{\max} = 664$ nm) and A_0 is the initial absorbance.

4.4 Conclusions

Hierarchical dendrite-, star-, popcorn-, sphere-like CdS micro- or nanostructures were synthesized via a programmed microwave-assisted solvothermal process. The time-dependent growth process mainly involved four steps: (1) nuclei formation, (2) surface-tension dendritic growth, (3) tip-splitting growth and (4) kinetic dendritic growth. The shape controlled synthesis of CdS crystals with various morphologies was realized by tuning the reaction conditions, such as the solvent, reaction temperature and time. The as-formed CdS crystals exhibit shape-dependent optical properties and photocatalytic activities. The dendrite-like CdS shows an enhanced photocatalytic activity due to the hierarchical structure with multiple branch arrays. They should be

ideal candidates for better understanding the shape-dependent properties in optical, photocatalytic, nanoelectronic and photovoltaic devices. Compared to the conventional hydrothermal method, the programmed microwave approach is more facile and more suitable for large-scale industrial production. This versatile closed-vessel microwave heating technique will provide a novel methodology for the synthesis of other nanomaterials with controlled shapes and unique properties.

4.5 References

- [1] (a) Alivisatos, A. P. *Science* **1996**, *271*, 933; (b) Hu, J. T.; Odom, T. W.; Lieber, C. M. *Acc. Chem. Res.* **1999**, *32*, 435; (c) Wang, X.; Zhuang, J.; Peng, Q.; Li, Y. D. *Nature* **2005**, *437*, 121; (d) Yu, J. C.; Li, G. S.; Wang, X. C.; Hu, X. L.; Leung, C. W.; Zhang, Z. D. *Chem. Commun.* **2006**, 2717; (e) Lei, Z. B.; Li, J. M.; Ke, Y. X.; Zhang, Y.; Wang, H.; He, G. F. *J. Mater. Chem.* **2001**, *7*, 1778.
- [2] Jun, Y. W.; Lee, S. M.; Kang, N. J.; Cheon, J. *J. Am. Chem. Soc.* **2001**, *123*, 5150.
- [3] Manna, L.; Scher, E. C.; Alivisatos, A. P. *J. Am. Chem. Soc.* **2000**, *122*, 12700.
- [4] (a) Xie, R. H.; Bryant, G. W.; Lee, S.; Jaskolski, W. *Phys. Rev. B* **2002**, *65*, 235306/1; (b) Morkel, M.; Weinhardt, L.; Lohmüller, B.; Heske, C.; Umbach, E.; Riedl, W.; Zweigart, S.; Karg, F. *Appl. Phys. Lett.* **2001**, *79*, 4482; (c)

- Schlamp, M. C.; Peng, X. G.; Alivisatos, A. P. *J. Appl. Phys.* **1997**, *82*, 5837; (d) Peng, X. G.; Schlamp, M. C.; Kadavanich, A. V.; Alivisatos, A. P. *J. Am. Chem. Soc.* **1997**, *119*, 7019; (e) Wang, Z. L. *Adv. Mater.* **2000**, *12*, 1295; (f) Zhang, J.; Jiang, F. H.; Zhang, L. D. *J. Phys. Chem. B* **2004**, *108*, 7002.
- [5] (a) Liang, H. J.; Angelini, T. E.; Braun, P. V.; Wong, G. C. L. *J. Am. Chem. Soc.* **2004**, *126*, 14157; (b) Yang, C. S.; Awschalom, D. D.; Stucky, G. D. *Chem. Mater.* **2002**, *14*, 1277; (c) Yao, Q. Z.; Jin, G.; Zhou, G. T.; Wang, X. C.; Yu, J. *C. J. Nanosci. Nanotechnol.* **2008**, *8*, 3112.
- [6] (a) Duan, X. F.; Huang, Y.; Agarwal, R.; Lieber, C. M. *Nature* **2003**, *421*, 241; (b) Ge, J. P.; Li, Y. D. *Adv. Funct. Mater.* **2004**, *14*, 157; (c) Kang, C. C.; Lai, C. W.; Peng, H. C.; Shyue, J. J.; Chou, P. T. *Small* **2007**, *3*, 1882.
- [7] (a) Gao, T.; Wang, T. H. *J. Phys. Chem. B* **2004**, *108*, 20045; (b) Ip, K. M.; Wang, C. R.; Li, Q.; Hark, S. K. *Appl. Phys. Lett.* **2004**, *84*, 795.
- [8] Chu, H. B.; Li, X. M.; Chen, G. D.; Zhou, W. W.; Zhang, Y.; Jin, Z.; Xu, J. J.; Li, Y. *Cryst. Growth Des.* **2005**, *5*, 1801.
- [9] (a) Zhang, Y. H.; Guo, L.; Yin, P. G.; Zhang, R.; Zhang, Q.; Yang, S. H. *Chem. Eur. J.* **2007**, *13*, 2903; (b) Zhao, P. T.; Huang, K. X. *Cryst. Growth Des.* **2008**, *8*, 717.

- [10] (a) Gedye, R.; Smith, F.; Westaway, K.; Ali, H.; Baldisera, L.; Laberge, L.; Rousell, L. *Tetrahedron Lett.* **1986**, *27*, 279; (b) Giguere, R. J.; Bray, T. L.; Duncan, S. M.; Majetich, G. *Tetrahedron Lett.* **1986**, *27*, 4945.
- [11] (a) Hu, X. L.; Yu, J. C.; Gong, J. M.; Li, Q.; Li, G. S. *Adv. Mater.* **2007**, *19*, 2324; (b) Hu, X. L.; Yu, J. C.; Gong, J. M.; Li, Q. *Cryst. Growth Des.* **2007**, *7*, 2444; (c) Yu, J. C.; Hu, X. L.; Li, Q.; Zhang, L. Z. *Chem. Commun.* **2005**, 2704; (d) Hu, X. L.; Yu, J. C. *Adv. Funct. Mater.* **2008**, *18*, 1.
- [12] Kundu, S.; Liang, H. *Adv. Mater.* **2008**, *20*, 826.
- [13] Yang, P.; Xie, Y.; Qian, Y. T.; Liu, X. M. *Chem. Commun.* **1999**, 1293.
- [14] Li, Y. D.; Liao, H. W.; Ding, Y.; Fan, Y.; Zhang, Y.; Qian, Y. T. *Inorg. Chem.* **1999**, *38*, 1382.
- [15] (a) Xiong, S. L.; Xi, B. J.; Wang, C. M.; Zou, G. F.; Fei, L. F.; Wang, W. Z.; Qian, Y. T. *Chem. Eur. J.* **2007**, *13*, 3076.
- [16] Jang, J. S.; Joshi, U. A.; Lee, J. S. *J. Phys. Chem. C* **2007**, *111*, 13280.
- [17] (a) Barnard, A. S.; Curtiss, L. A. *Nano Lett.* **2005**, *5*, 1261; (b) Cao, H.; Gong, Q.; Qian, X.; Wang, H.; Zai, J.; Zhu, Z. *Cryst. Growth Des.* **2007**, *7*, 425.
- [18] Xu, D.; Liu, Z. P.; Liang, J. B.; Qian, Y. T. *J. Phys. Chem. B* **2005**, *109*, 14344.
- [19] Zhang, B.; Ye, X. C.; Hou, W. Y.; Zhao, Y.; Xie, Y. *J. Phys. Chem. B* **2006**, *110*, 8978.

- [20] (a) Dick, K. A.; Depper, K.; Larsson, M. W.; Wallenberg, L. R.; Samuelson, L. *Nat. Mater.* **2004**, *3*, 380; (b) Fleury, V. *Nature* **1997**, *390*, 145.
- [21] (a) Mullins, W. W.; Sekerka, R. F. *J. Appl. Phys.* **1963**, *34*, 323; (b) Li, S. W.; Lowengrub, J. S.; Leo, P. H.; Cristini, V. *J. Cryst. Growth* **2005**, *277*, 578.
- [22] Ben-Jacob, E.; Garik, P. *Nature* **1990**, *343*, 523.
- [23] Sunagawa, I. *Bull. Mineral* **1981**, *104*, 81.
- [24] (a) Peng, Z. A.; Peng, X. G. *J. Am. Chem. Soc.* **2001**, *123*, 1389; (b) Peng, X. G. *Adv. Mater.* **2003**, *15*, 459.
- [25] Cheng, Y.; Wang, Y. S.; Bao, F.; Chen, D. Q. *J. Phys. Chem. B* **2006**, *110*, 9448.
- [26] Tao, A.; Sinsermsuksakul, P.; Yang, P. D. *Angew. Chem. Int. Ed.* **2006**, *45*, 4597.
- [27] Pinna, N.; Weiss, K.; Urban, J.; Pileni, M. P. *Adv. Mater.* **2001**, *13*, 261.
- [28] Wang, F.; Xu, G. Y.; Zhang, Z. Q.; Xin, X. *Eur. J. Inorg. Chem.* **2006**, *1*, 109.
- [29] Nandakumar, P.; Vijayan, C.; Rajakshmi, M.; Arora, A. K.; Murti, Y. V. G. S. *Phys. E* **2001**, *11*, 377.
- [30] Donahue, E. J.; Roxburgh, A.; Yurchenko, M. *Mater. Res. Bull.* **1998**, *33*, 323.
- [31] Nanda, K. K.; Sarangi, S. N.; Sahu, S. N.; Deb, S. K.; Behera, S. N. *Phys. B* **1999**, *262*, 31.

Chapter Five

Biocompatible Anatase Single-Crystal Photocatalysts with Tunable Percentage of Reactive Facets

5.1 Introduction

Since the report of Fujishima and Honda in 1972,¹ TiO₂ has become the most widely used semiconductor in photocatalysis due to their environmental and energy applications. Research aimed at enhancing the photocatalytic efficiency has intensified over the years.² Among the TiO₂ found in nature, anatase exhibits a higher activity than other polymorphs.^{3,4} Because of the ability of anatase (001) to dissociatively adsorb water molecules, TiO₂ with well-defined {001} facets is particularly useful for solar energy applications.³ However, the most stable and frequently observed surface on anatase has a (101) orientation.^{5,6} The (001) is only a minority surface due to its high surface energy (0.90 J/m²) comparing to that of the (101) surface (0.44 J/m²).^{7,8} Up to now, surface science investigations have yielded an amazing degree of atomic-scale structural and chemical information on rutile TiO₂ (110), whereas work on anatase is scarce,^{5,9-11} mainly because of the difficulty in

growing large anatase single-crystals. Although there are general and qualitative rules that can assess the stability of oxide surfaces according to first-principles calculations, controlling the shape of TiO₂ single-crystals exposed with reactive {001} facets is still a great challenge. Most available experimental information on the structure surface chemistry of anatase single-crystals is still based on studies of dispersed samples. Moreover, the use of different preparation techniques has led to samples with various morphologies and impurity contents. It may be responsible for the different or sometimes conflicting experimental results reported in the literature.^{12,13} Therefore, a flexible and simple system to fabricate large anatase TiO₂ single-crystals with a continuously tunable percentage of reactive facets by simply changing one parameter is highly desirable. These single-crystals with controlled exposed reactive facets are expected to possess the same morphology and physical properties, such as surface area and particle size. They should be very useful as model single-crystals for fundamental studies in surface science.

Lately, Lu and co-workers made an important breakthrough in the fabrication of anatase single-crystals with 47 % of the highly reactive {001} facets by using hydrofluoric acid as a capping agent under hydrothermal conditions.¹⁴ Soon after, they developed new solvothermal method using 2-propanol as a synergistic capping agent and reaction medium together with hydrofluoric acid to obtain anatase TiO₂

nanosheets with 64 % of the {001} facets.¹⁵ Beside, Xie and co-workers used a similar strategy to obtain anatase TiO₂ nanosheets with 89 % exposed {001} facets.¹⁶ All these available approaches require the use of an extremely corrosive and toxic hydrofluoric acid as the shape controlling agent. This is against the principle of “green chemistry”. Recently, Xia and co-workers reported a novel hydrofluoric acid-free method to anatase TiO₂ nanocrystals with 9.6 % chemically active {001} facets.¹⁷ The nanocrystals were prepared by digesting electrospun nanofibers in acetic acid solution, following by hydrothermal treatment at 150 °C for 20 h. Very recently, Ohtani and co-workers have prepared single-crystalline anatase with relatively high yield of decahedral particles through a gas-phase reaction using TiCl₄ as a titanium source.¹⁸ However, very harsh conditions including high temperature (>1500 K) are needed.

Although the hydrothermal/solvothermal or gas reaction approaches have shown their advantages in the fabrication of TiO₂ with reactive facets, they are not an energy-efficient process due to the long reaction time involved. Fortunately, such issue can be solved by using an efficient microwave-assisted method. Microwave-enhanced chemistry is based on the interaction of molecules in a reaction mixture with electromagnetic waves generated by a “microwave dielectric effect”.¹⁹ Such a process mainly depends on the specific polarity of molecules. Solvents which

are polar in nature have good potential to adsorb microwaves and convert them to thermal energy, thus accelerating the reactions as compared to results obtained using conventional heating.²⁰ To date, some studies have reported the preparation of TiO₂ powders, films and colloids by microwave hydrothermal processing.²¹⁻³⁰ Ionic liquids (ILs), known for their nonvolatile, nonflammable, and thermally stable properties, have been utilized as a green solvent for fabricating inorganic nanomaterial.³¹⁻³⁵ They have been proven to be good media for adsorbing microwaves,³⁶⁻³⁷ so it is logical to combine the “green” solvent aspect of ionic liquids with the “green” chemistry aspect of microwave irradiation. Liu and co-workers have reported a facile synthesis of high quality TiO₂ nanocrystals in ionic liquids via a microwave-assisted process.³⁸ However, using such method to fabricate of large micro-sized anatase TiO₂ single-crystals is difficult. Recently, our group has reported an efficient microwave-enhanced ionothermal approach for fabricating micrometer-sized TiO₂ with 80 % {001} reactive facets.³⁹ Nevertheless, how to subtly adjust the level of the reactive facets still remains a strenuous task.

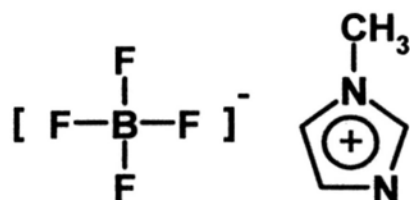
Herein, we report on the preparation and characterization of micrometer-sized TiO₂ single-crystals with continuously tunable percentage of reactive {001} facets via a microwave-enhanced ionothermal approach. The products show excellent photocatalytic efficiency for both oxidation of NO gas in air and degradation of

organic compounds in aqueous solution under UV light irradiation. Furthermore, the biocompatibility of the anatase TiO₂ single-crystals was studied by using Zebrafish (*D. rerio*) as a model. To the best of our knowledge, biocompatible TiO₂ single-crystals with reactive facets have never been reported.

5.2 Experimental Section

5.2.1 Preparation of TiO₂ with Tunable Percentage of Reactive Facets

In a typical synthesis, 0.04 mol/L titanium tetrafluoride (ACROS) aqueous solution was prepared by dissolving 1.24 g titanium tetrafluoride in 250.0 mL D.I. water which contains 0.2 mL hydrochloric acid (37 %, (MERCK)). Then 0.5 mL ionic liquid 1-methyl-imidazolium tetrafluoroborate, synthesized according to literature,⁴⁰ was added to 30.0 mL 0.04 mol/L titanium tetrafluoride aqueous solution while stirring. The chemical structure of the ionic liquid is shown schematically below.



The mixture was sealed in a Teflon-lined double-walled digestion vessel. After treating at a controllable temperature of 210 °C for 90 minutes using a microwave digestion system (Ethos TC, Milestone), the vessel was then cooled down to room

temperature. The products (Sample 1) were collected by centrifugation, washed with deionized water and absolute ethanol, and dried in a vacuum at 80 °C for 4 h. Samples 2-3 were prepared by changing the amount of ionic liquid to 1.0 mL and 2.0 mL while keeping other conditions unchanged. The experimental conditions of different samples are summarized in Table 5.1.

5.2.2 Characterization

X-ray diffraction (XRD) patterns were recorded using a Bruker D8 Advance diffractometer with high-intensity CuK α irradiation ($\lambda = 1.5406 \text{ \AA}$). Transmission electron microscopy (TEM) observations were carried out on a Tecnai F20 microscope (FEI, 200 kV). The general morphology of the products was characterized by scanning electron microscopy (FEI Quanta 400 FEG microscopes). X-ray photoelectron spectroscopy (XPS) measurement was done with a PHI Quantum 2000 XPS system with a monochromatic Al-K α source and a charge neutralizer. All the binding energies were referenced to the C_{1s} peak at 284.8 eV of the surface adventitious carbon.

5.2.3 Photoactivity Test

The photocatalytic oxidation of NO gas in air was performed at ambient temperature in continuous flow ion reactor with a volume of 4.5 L (10×30×15 cm (H×L×W)). Four UV-A fluorescent lamps (TL 8W/08 BLB, Philips, Holland) were vertically placed outside the reactor above the sample dish. The wavelength of the lamps ranges from 300 to 400 nm with a maximum intensity at 365 nm. Four minifans were fixed around the lamps to cool the system. For the activity test, the TiO₂ surfaces were firstly cleaned by simple heat treatment at 600 °C for 90 min to remove the surface F element. Then 0.2 g products dispersed in D. I. water were coated onto a dish with a diameter of 12.0 cm. Finally, the samples were dried at 70 °C and then cooled to room temperature. The stock NO gas had a concentration of 48 ppm (N₂ balance, BOC gas) that was traceable to the National Institute of Standards and Technology (NIST) standard. The initial concentration of NO was diluted to about 400 ppb by the air stream supplied by a zero air generator (Thermo Environmental Inc. Model 111). The humidity level of the NO flow was maintained at 70 % (2100 ppmv) by passing the zero air streams through a humidification chamber. The gas streams were pre-mixed thoroughly by a gas blender and the flow rate was controlled at 4 L/min by a mass flow controller. Upon adsorption-desorption equilibrium, the lamp was turned on. The concentration of NO was continuously

monitored by a chemiluminescence NO analyzer (Thermo Environmental Instruments Inc. Model 42c) at a sampling rate of 0.7 L/min.⁴¹ The removal rate (%) of NO was calculated based on the following equation:

$$\text{NO removal rate (\%)} = ([\text{NO}]_{\text{in}} - [\text{NO}]_{\text{out}}) / [\text{NO}]_{\text{in}} \times 100\%$$

The photocatalytic treatment of aqueous organic pollutants of these anatase TiO₂ single-crystals was measured by the degradation of 4-chlorophenol in an aqueous solution. The experiments were performed at 25 °C in a self-designed 150 ml reactor containing 0.08 g catalyst calcined at 600 °C for 90 min and 60 ml of 10 ppm 4-chlorophenol aqueous solution. A 300 W high-pressure mercury vapor lamp was used as the UV light source, which was mounted at 5 cm around the solution. Vigorous stirring (900 rpm) was employed to ensure the adsorption equilibrium and to eliminate any diffusion effect. The equilibrium 4-chlorophenol concentration was used as the initial concentration of 4-chlorophenol. The photocatalysis was started by irradiating the reaction mixture with UV light. The reaction time was 2 h. The concentrations of 4-chlorophenol and its degradation products were measured with a HPLC system (Waters Baseline 810) with a Waters 486 tunable UV absorbance detector. A Supelco LC-18-DB column (250 mm×4.6 mm) was applied. The eluent consisted of methanol : water (40:60) mixture, and the flow rate was 1 mL/min. The aromatic compounds were detected at 220 nm. Millipore discs were used to separate

the catalysts before analysis of the solution.⁴² The blank experiment shows the 4-chlorophenol degradation was less than 2 %. Conventional anatase TiO₂ single-crystals were chosen as a reference under the same experimental conditions.

Conventional anatase TiO₂ single-crystals were prepared by adding 5 mL TiCl₄ (ACROS) into a conical flask which contains 40 ml N₂ (l) and 15 mL H₂O. After evaporation of N₂ (l), the clear colorless TiCl₄ solution was used as the stock solution. Then 2 mL stock solution and 2 mL 1-methyl-imidazolium tetrafluoroborate were added into 48 mL D.I. water under stirring. After treating at a controllable temperature of 210 °C for 90 min using a microwave digestion system (Ethos TC, Milestone), the solution was then cooled down to room temperature. Finally, the product was collected by centrifugation, washed with deionized water and absolute ethanol, and dried in a vacuum at 80 °C for 4 h.

5.2.4 Toxicity Study

Zebrafish (*D. rerio*) adults were obtained from local pet shops in Hong Kong. They were kept in a glass aquarium of filtered tap water with following conditions: 26±1 °C, dissolved oxygen content between 90.2 % and 95.1 %, 14:10 h light:dark period, and live brine shrimp fed twice a day.

The fishes with male:female ratio of 2:1 were put into a specific spawning aquarium with a mesh bottom to protect the eggs from being eaten at about 7:30 p.m. The fertilized eggs were collected the next morning as spawning and fertilization took place within 30 minutes when the light is switched on. The eggs were rinsed several times and raised at 28 °C till 96-hour Post-fertilization larvae, and then divided to 28 beakers with each beaker 20 larvae for toxicity assessment of TiO₂ single-crystals (calcined at 600 °C for 90 min) aqueous solution (50, 100, 250, 500, and 1000 ppb, prepared under ultrasonication).

The larvae were then exposed in 3 beakers for the control experiment and 25 beakers with solution of 5 different concentrations (50, 100, 250, 500, and 1000 ppb, 5 beakers for each concentration) for exposure treatment. The number of surviving larvae was recorded after 24, 72 and 96 h exposure and the survival rate was evaluated for the three time periods.

Table 5.1 Summary of experimental conditions and physical properties of different samples.

| Sample | Ti precursor ^[a] | Ionic liquid ^[b] | Degree of truncation | % _{001} |
|--------|-----------------------------|-----------------------------|----------------------|--------------------|
| 1 | 30 mL | 0.5 mL | 0.71 | 27 |
| 2 | 30 mL | 1.0 mL | 0.80 | 39 |
| 3 | 30 mL | 2.0 mL | 0.86 | 50 |

^[a]0.04 M TiF₄ aqueous solution, ^[b]1-methyl-imidazolium tetrafluoroborate.

5.3 Results and Discussion

5.3.1 XRD and SEM Analysis

Fig. 5.1a shows a typical X-ray diffraction (XRD) pattern of a sample prepared with 30 mL 0.04 M TiF₄ and 0.5 mL ionic liquid at 210 °C for 90 min. The diffraction peaks can be indexed to pure anatase phase TiO₂ (tetragonal, *I*4₁/amd, JCPDS No. 21-1272). There are no observable diffraction peaks at 27 ° or 31 °, indicating that the as-prepared samples are free of rutile or brookite impurities phases.

Fig. 5.1b-d show the representative field emission scanning electron microscope (FESEM) images of Sample 1. From Fig. 5.1b, we can see that the as-prepared anatase TiO₂ single-crystals are monodispersed with a relatively narrow average particle size distribution (about 2.2 μm). From the symmetries of the well-faceted crystal structure, the two flat square surfaces are identified as {001} facets (shown in Fig. 5.1c) while the other eight isosceles trapezoidal surfaces are {101} facets (shown in Fig. 5.1d).

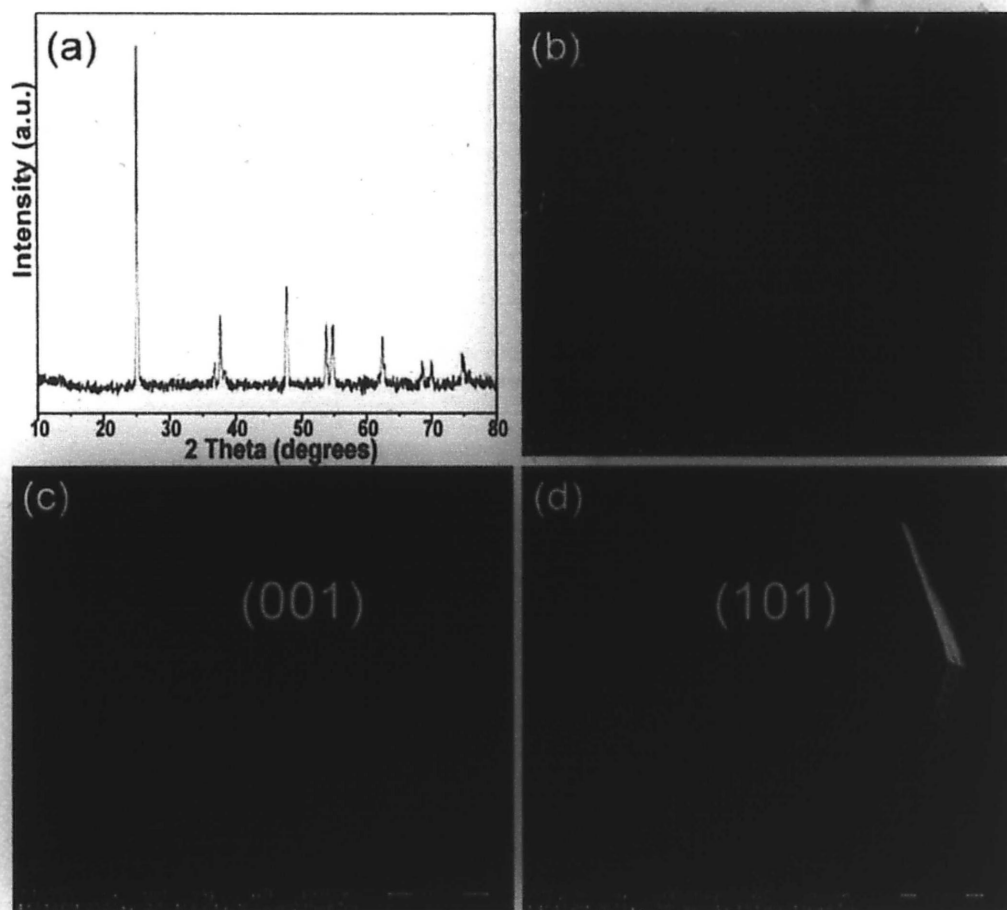


Figure 5.1 Typical XRD pattern (a), low-magnification FESEM image (b) and side view FESEM image (c, d) of Sample 1 prepared with 30 mL 0.04 M TiF₄ and 0.5 mL ionic liquid at 210 °C for 90 min.

The morphology of anatase TiO₂ single-crystals can be defined in terms of two independent length parameters. The side of the bipyramidal is denoted A. The side of the “truncation” facets is denoted B. The degree of truncation may therefore be described by the size of B with respect to A (where $0 \leq B \leq A$).⁴³ The ratio of reactive {001} facets to the total surface area may therefore be described by $S_{\{001\}}/S_{\text{total}}$ or the value of B/A. Therefore, we estimate the degree of truncation for Sample 1 to be 0.71 (relative standard deviation $\sigma \leq 5\%$). The percentage of reactive

{001} facets is up to 27 %. Generally, anatase crystals often exhibit a closed tetragonal bipyramidal form or a truncated bipyramids with only 6 % reactive {001} facets.⁴⁴ The average size of the anatase single-crystals for Sample 1 is 2.2 μm with a thickness of 1.7 μm .

5.3.2 TEM Analysis

Transmission electron microscope (TEM) images and high-resolution TEM (HRTEM) images provide further insight into the structural information on the anatase single-crystals (Sample 1). Fig. 5.2a shows a typical bright-field TEM image for an individual single-crystal of $\sim 2.2 \mu\text{m}$ in diameter. Its corresponding electron diffraction (ED) pattern is shown in Fig. 5.2b, indicating the single-crystal nature. It can be indexed into diffraction spots of [001] zone. The high-resolution TEM (HRTEM) image (Fig. 5.2c) further supports the claim of single crystallinity. A representative intensity profile (inset) covers the line scan (labeled by a line in Fig. 5.2c) across the lattice fringes. The periodic fringe spacing of $\sim 0.19 \text{ nm}$ corresponds to interplanar spacing between the (200) plane, which is in agreement with the previous report.⁴⁵

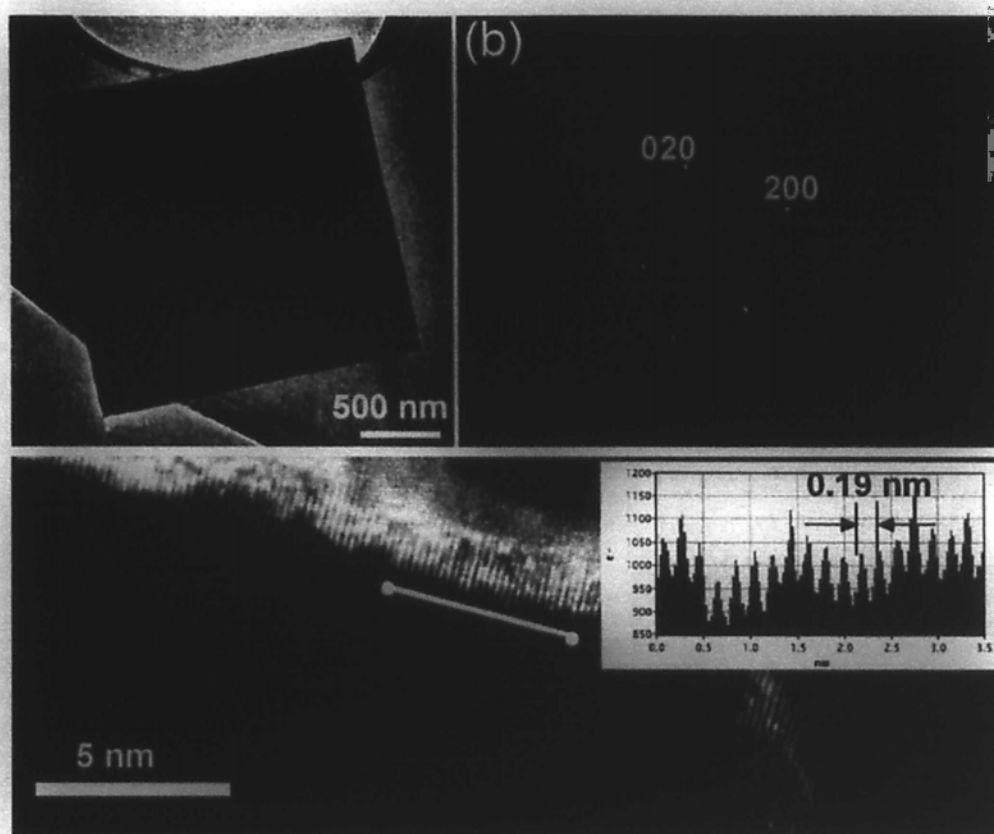


Figure 5.2 TEM image (a), ED pattern (b), HRTEM image (c) and corresponding intensity profile for the line scan across the lattice fringes (inset) of Sample 1 prepared with 30 mL 0.04 M TiF₄ and 0.5 mL ionic liquid at 210 °C for 90 min.

5.3.3 XPS Analysis

The X-ray photoelectron spectrum (shown in Fig. 5.3a) gives the surface composition of these crystals. Four characteristic peaks of Ti, O, F and C are observed. The binding energy of Ti 2p_{3/2} and Ti2p_{1/2} (Fig. 5.3b) is 458.8 and 464.3 eV, indicating the oxidation state of the Ti element is the same to that of bulk TiO₂.⁴⁶

The X-ray photoelectron spectrum of F 1s core electrons for Sample 1 is shown in Fig. 5.3c. The measured binding energy is only 684.5 eV, which is a typical value for fluorated TiO₂ system such as TiOF₂ or the surface Ti-F species.⁴⁷ However, for

atomic incorporation of F atoms or their substitution for O atoms, the binding energy of F 1s is 688.5 eV. Therefore, we conclude that the F element is present as surface atoms. Such fluorated surface, resulting from the F-riched molecule 1-methyl-imidazolium tetrafluoroborate, can significantly lower the surface energy of {001} facets due to the high binding energy of F-Ti (569.0 kJ mol⁻¹).^{14, 39} In order to illustrate the important role of F-riched environment, deeper evidence was supported by a controlled experiment in the absence of ionic liquid, in which only hollow anatase TiO₂ nanospheres were obtained in the absence of ionic liquid (see in Fig. 5.4a). These results demonstrate the F-riched environment, attributed to the ionic liquid, is a key determinant to form {001} facets exposed anatase TiO₂ single-crystals.

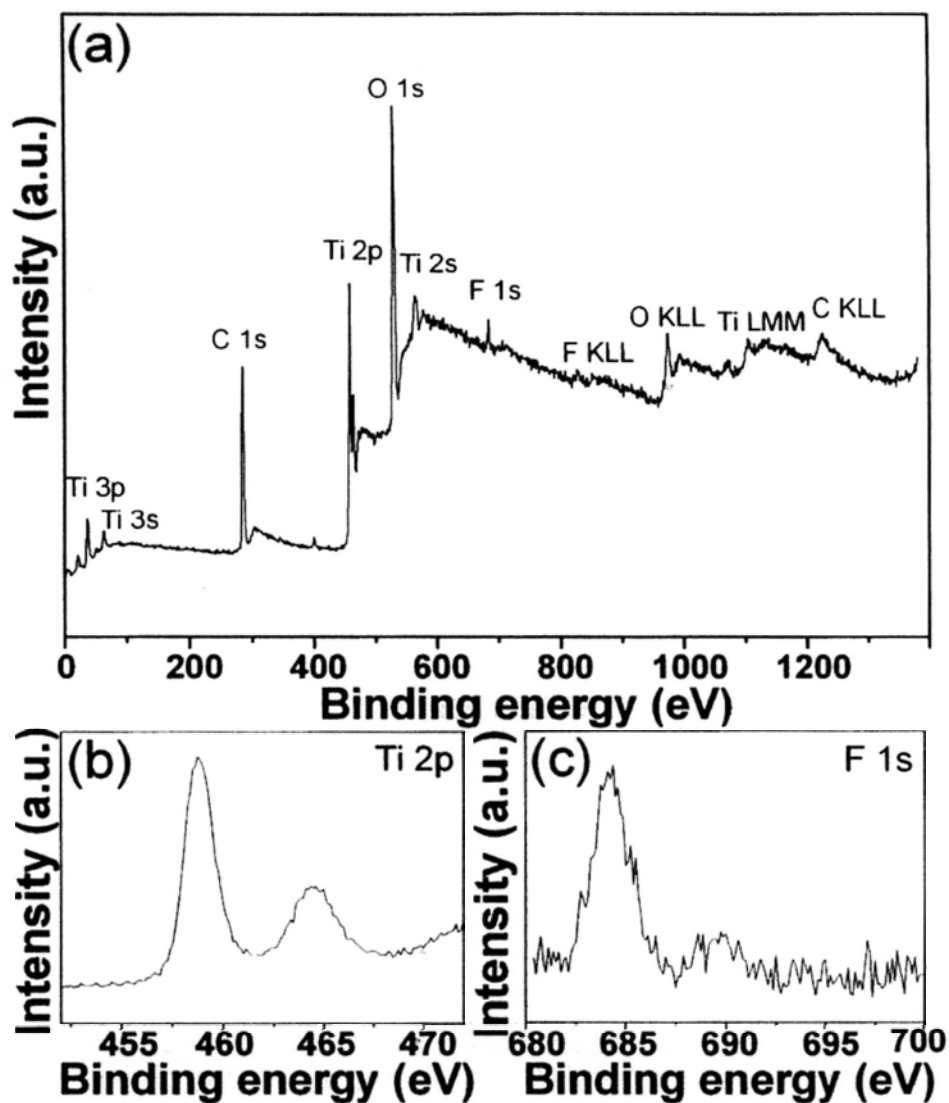


Figure 5.3 X-ray photoelectron survey spectra (a), fine scan of Ti 2p (b) and F 1s (c) of Sample 1 prepared with 30 mL 0.04 M TiF₄ and 0.5 mL ionic liquid at 210 °C for 90 min.

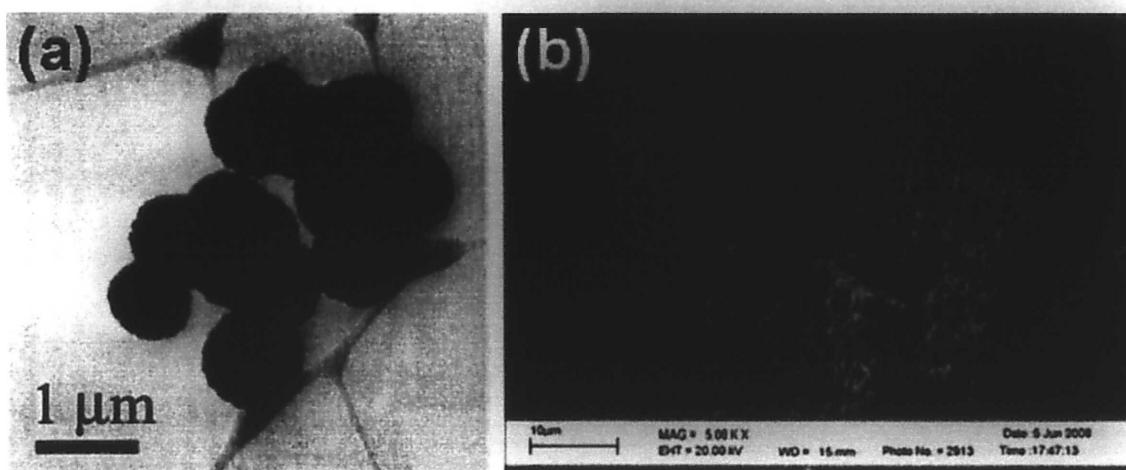
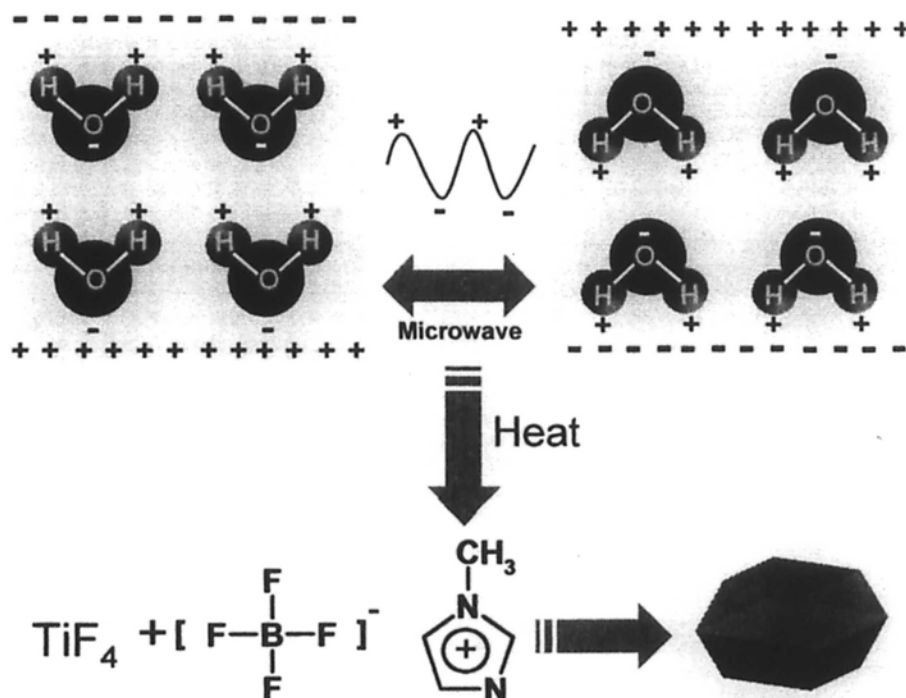


Figure 5.4 TEM image of hollow anatase TiO₂ nanospheres obtained in the absence of ionic liquid (a) and SEM image of anatase TiO₂ single-crystal aggregates obtained under conventional hydrothermal condition at 210 °C for 48 h (b).

5.3.4 The Mechanism for the Formation of {001} Facets Exposed TiO₂

The mechanism for the formation of anatase TiO₂ exposing with {001} facets in aqueous solution by microwave irradiation is shown in Scheme 5.1. In the microwave frequency range, polar molecules such as H₂O orientate with the electric field. When dipolar molecules re-orientate with respect to an alternating electric field, they lose energy in the form of heat by molecular friction. The ability of the solvent to heat in the microwave field is dependent on the dielectric loss constant. Water has high dielectric losses. Therefore, it is an ideal solvent for microwave rapid heating.⁴⁸ The ionic liquid in this reaction system provides a synergistic effect to adsorb the microwaves. This may explain why the current method is efficient in the synthesis of anatase single-crystals. A control experiment by using conventional hydrothermal

condition shows that at least 48 hours were required for the synthesis of TiO₂ single-crystals exposed with {001} facets. Furthermore, the SEM image (see in Fig. 5.4b) shows that these anatase TiO₂ single-crystals are highly aggregated sheets. These results indicate that microwaves can provide rapid and uniform heating of reagent and solvents. Fast heating accelerates the hydrolysis of TiF₄ and nucleation of the anatase cluster. The homogeneous microwave heating also provides uniform nucleation and growth conditions, leading to anatase TiO₂ with narrow size distribution. Furthermore, due to rapid and homogenous microwave heating, a better crystallinity can be obtained. Therefore, high-quality TiO₂ single-crystals exposed with {001} facets can be synthesized with a high yield.



Scheme 5.1 Formation mechanism of {001} facets exposed TiO₂ by microwave irradiation.

When the volume of ionic liquid was increased from 0.5 to 1.0 mL, the anatase TiO₂ single-crystals (Sample 2) exhibited a higher level of reactive {001} facets. As shown in Fig. 5.5a and 5.5b, the anatase TiO₂ single-crystals with a small thickness of ~1.0 μm exhibit a higher degree of truncation than that of Sample 1. The degree of truncation and the percentage of the reactive facets are estimated to be 0.80 and 39 % (shown in Table 5.1). Such enhancement of the degree of truncation can be attributed to the high concentration of the ionic liquid. The anion of the ionic liquid used in this work is [BF₄]⁻. It has four F atoms in one molecule. As known, the stronger stabilization effect of F atoms is in favor of the isotropic growth of {001} facets. Therefore, the more bulky [BF₄]⁻ groups can promote the preferred growth of the {001} facets. This explanation is further confirmed by Sample 3, prepared with 2.0 mL of ionic liquid. As shown in Fig. 5.5c and 5.5d, these single-crystals have the highest degree of truncation with a small thickness of ~500 nm. The ratio of surface area of reactive {001} facets to total surface area was increased to about 50 %. The models for the three samples shown in Fig. 5.6 demonstrate an increasing tendency of the percentage of exposed reactive {001} facets. These anatase TiO₂ single-crystals are expected to have great applications in environmental applications, such as air and water purification.

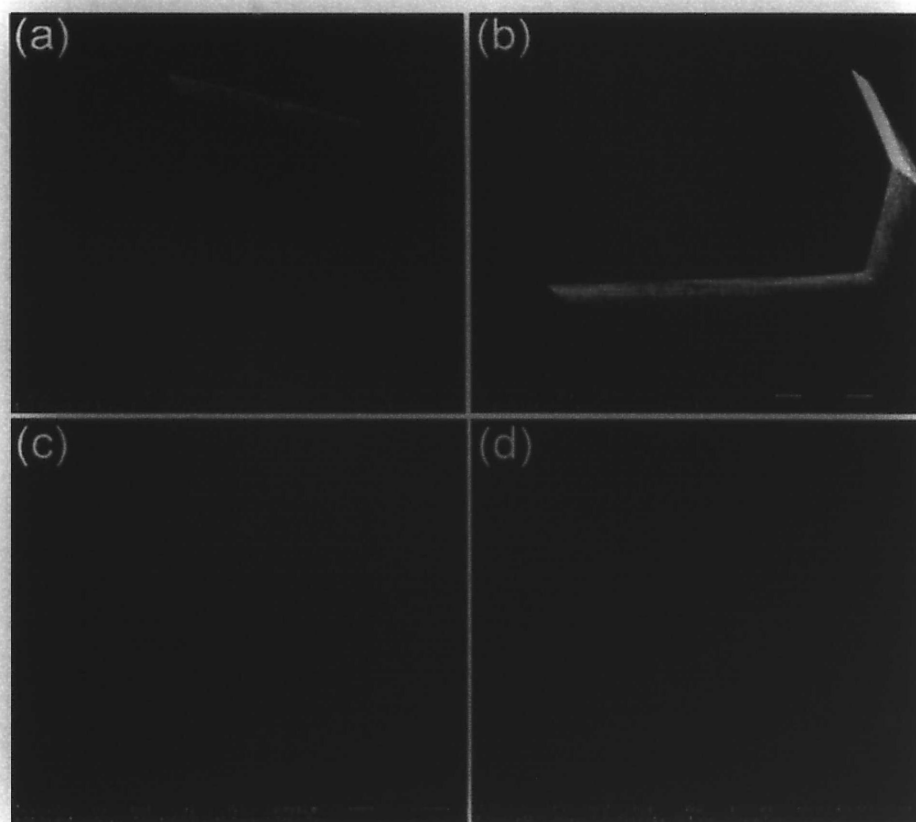


Figure 5.5 FESEM images of Sample 2 (a, b) and Sample 3 (c, d) prepared with 1 mL and 2 mL ionic liquid at 210 °C for 90 min.

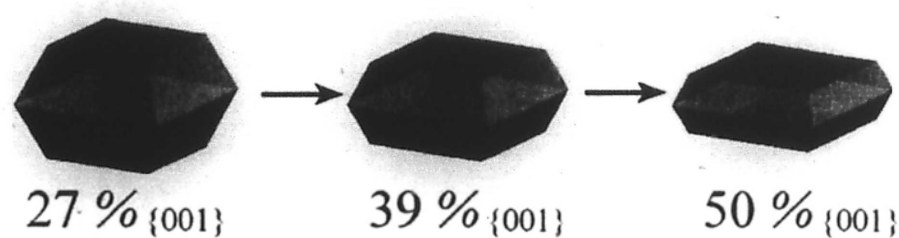


Figure 5.6 Simulated models for Samples 1-3, indicating increasing tendency of the percentage of {001} facets.

5.3.5 Photocatalytic Performance Study

Recently, more attentions have been paid to indoor air quality with increasing awareness of the public environment and health.⁴⁹ As an ambient temperature catalytic process, photocatalysis has attracted considerable attention in view of solar energy conversion and environmental cleaning.⁵⁰⁻⁵³ To evaluate the photocatalytic performance of the anatase single-crystal samples with different percentages of {001} facets, matching conventional TiO₂ crystals dominated by {101} facets were chosen as a reference. Results from XRD and SEM analyses (Fig. 5.7a and 5.7b) confirmed that the reference materials had virtually the same crystallinity and average particle size distribution as the samples. The removal rate of NO pollution at typical concentration levels in indoor air under UV irradiation was investigated. Fig. 5.8 shows the variation of NO concentration (C/C_0) with irradiation time under UV irradiation. The NO removal rate reaches 15 %, 24 %, 31 % and 38 % in 10 minutes for the conventional TiO₂ dominated by {101} facets and TiO₂ exposed with 27 %, 39 %, 50% {001} facets, respectively.

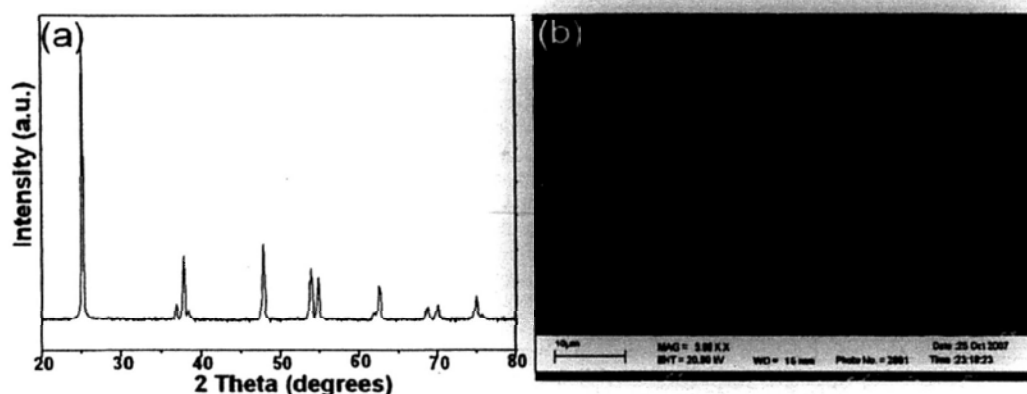


Figure 5.7 XRD pattern (a) and SEM image (b) of conventional TiO₂.

We use the Langmuir Hinshelwood model (L-H) to describe the initial rates of photocatalytic destruction of NO.⁵⁴ The initial photocatalytic degradation of NO was recognized to follow mass-transfer-controlled first-order-kinetics approximately as a result of low concentration target pollutants, as evidenced by the linear plot of $\ln(C/C_0)$ versus photocatalytic reaction time t (Fig. 5.8b). Fig. 5.8c shows the relationship between initial reaction rate constant and the percentage of {001} facets. The relationship of NO removal rate over different catalysts is also included in Fig. 5.8c. The initial rate constant of TiO₂ with 50 % reactive {001} facets is estimated to be 0.041 min⁻¹, faster than that over the other TiO₂ single-crystals with less exposed reactive facets. The initial rate constant over TiO₂ single-crystals with dominantly {101} facets is only 0.019 min⁻¹. The removal rate of NO also increases with the increasing percentage of {001} facets. The high level of photocatalytic activity of TiO₂ exposed with {001} facets might be related to the property of the exposed {001} surface, in addition to the high crystallinity with a low density of defects.¹⁸

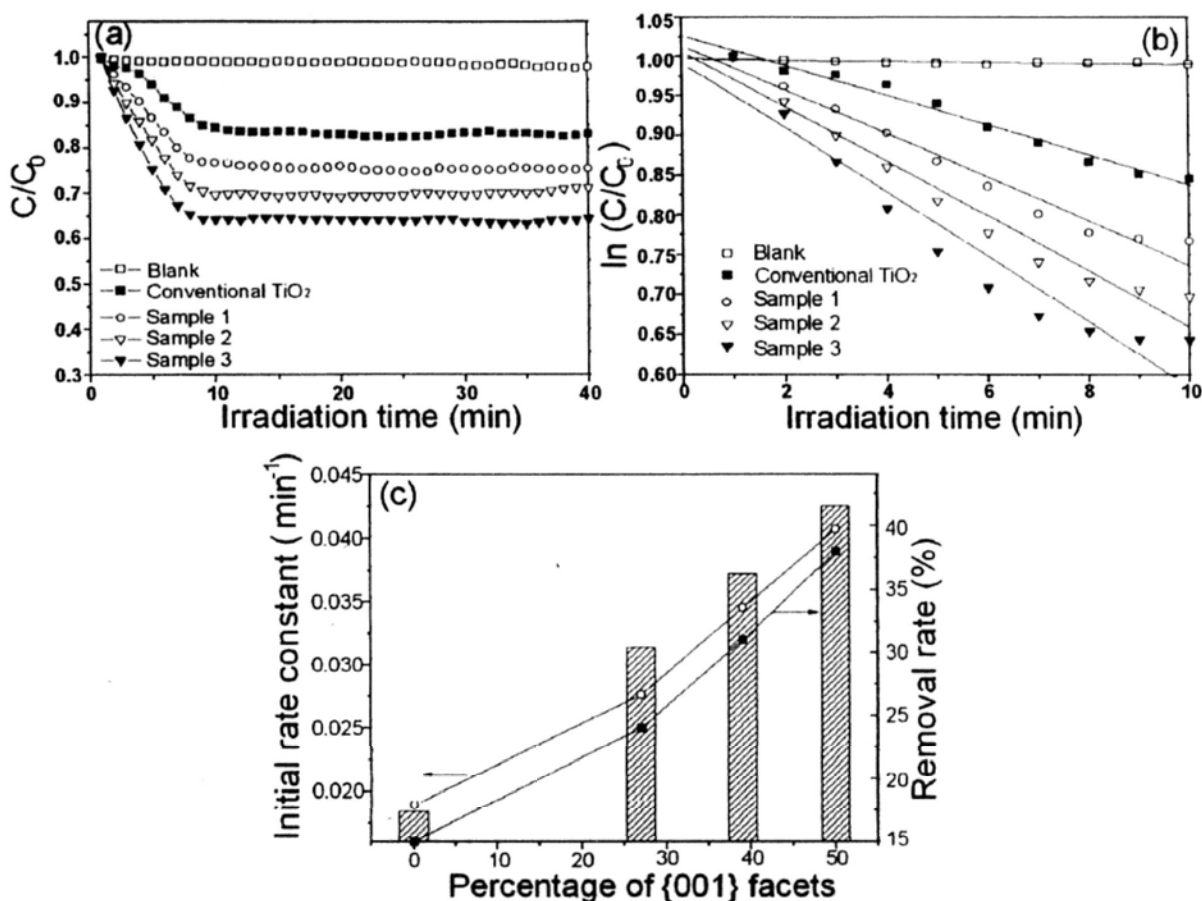


Figure 5.8 (a) Plots of the decrease in NO concentration vs irradiation time in the presence of different photocatalysts. (b) Dependence of $\ln(C/C_0)$ on irradiation time. (c) Initial rate constant (-○-) and removal rate (-■-) of NO for TiO₂ single-crystals with different percentage of {001} facets.

The photocatalytic performance of the prepared TiO₂ single-crystals was also measured in a liquid-phase reaction. The decomposition of aqueous 4-chlorophenol was used as a probe photocatalytic reaction. As shown in Fig. 5.9, all the truncated bipyramidal shape anatase single-crystals (Samples 1-3) exhibit much higher activities than that of the {001} unexposed TiO₂ single-crystals. The photoactivity enhances from 38.1 % to 66.3 % with increasing percentage of {001} facets from 0 % to 50 %. This indicates that the reactive {001} facets are important in the

photocatalytic reaction owing to their strong ability to dissociatively adsorb water to form hydroxyl radicals, which are key components in photocatalytic reactions.⁵⁵⁻⁵⁸

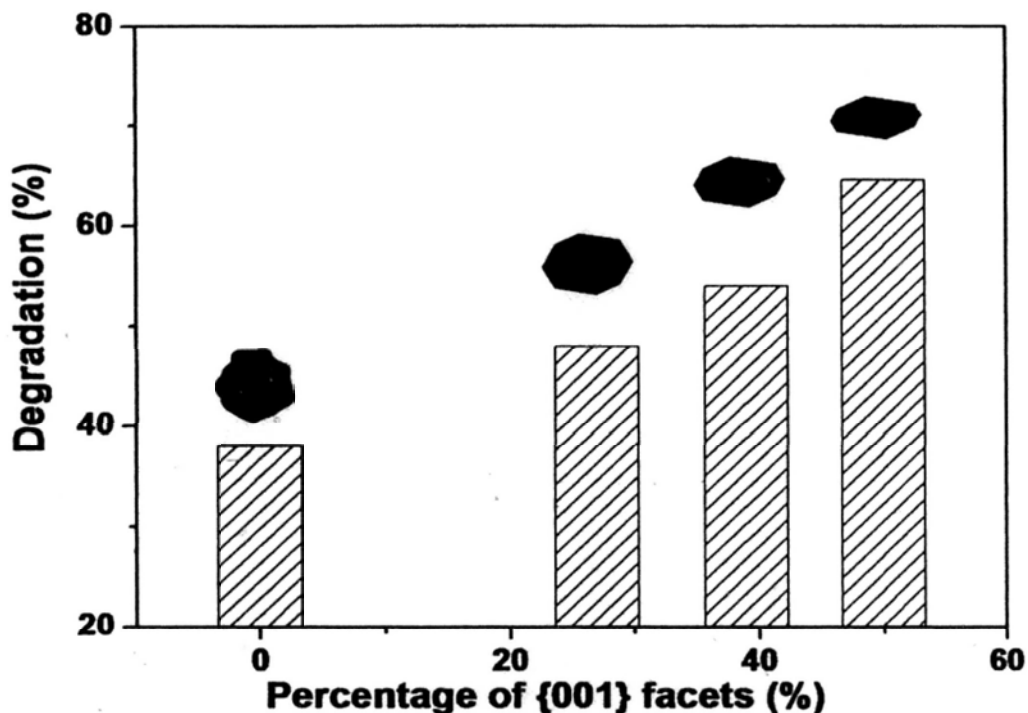


Figure 5.9 The effectiveness of the conventional TiO₂ single-crystal and Samples 1-3 on the degradation of 4-chlorophenol under UV irradiation.

5.3.6 Toxicity Study

While rapid development of nanomaterials will certainly continue, the application of these nanomaterials will be limited by their inherent toxicity.^{59, 60} The anatase TiO₂ crystals with high percentage of reactive {001} facets are promising photocatalysts, virus inhibitors and disinfectants. Massive quantities of this material need to be produced for these applications thereby increasing the potential risk of human exposure and raising additional concern about their short and long-term

toxicological effects. Therefore, the toxicity study of the anatase TiO₂ crystals is a necessary first step in assessing their safety. As known, the Zebrafish embryo (*Danio rerio*), possesses a high degree of homology to the human genome, offering an economically feasible platform for noninvasive real-time assessments of toxicity.⁶¹ The biocompatibility of the as-prepared anatase TiO₂ single-crystals were evaluated using Zebrafish (*D. rerio*) as a model. The survival rate after 24 h exposure was given in Fig. 5.10. These results illustrate a survival rate of virtually 100 % even under the highest concentration 1000 ppb, suggesting that the TiO₂ single-crystals are biocompatible. Interestingly, even after 72 h or 96 h exposure, the larvae livability was still as high as 100 %.

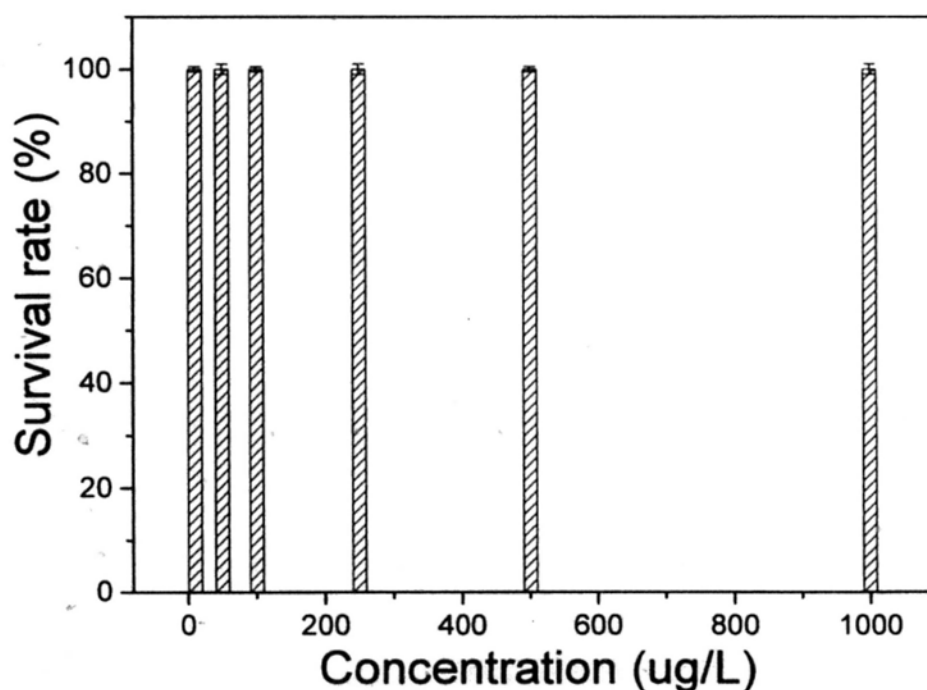


Figure 5.10 Livability of 4-day larvae after 24 h exposure to different concentrations of aqueous anatase TiO₂ single-crystals (Sample 3).

5.4 Conclusion

Biocompatible micrometer-sized anatase TiO₂ single-crystals with large and tunable percentage of reactive facets were synthesized in ionic liquid via a microwave-assisted process. The fluorine-rich ionic liquid (1-methyl-imidazolium tetrafluoroborate) serves as an essential structure-directing agent for the formation of the {001} reactive facets. These anatase TiO₂ single-crystals show good photocatalytic performance for oxidizing nitric oxide in air and degrading 4-chlorophenol in water. A strong correlation between the percentage of {001} facets and the photocatalytic activity was observed. The TiO₂ single-crystals with 50 % {001} facets were found to be nontoxic. This opens up many potential applications in environment, energy and biomedical fields.

5.5 References

- [1] Fujishima, A.; Honda, K. *Nature* **1972**, *238*, 37.
- [2] Thompson, T. L.; Yates, J. T. *Chem. Rev.* **2006**, *106*, 4428.
- [3] Hagfeldt, A.; Grätzel, M. *Chem. Rev.* **1995**, *95*, 49.
- [4] Li, G. S.; Yu, J. C.; Zhang, D. Q.; Hu, X. L.; Lau, W. M. *Sep. Purif. Technol.* **2009**, *67*, 152.
- [5] Diebold, U.; Ruzycki, N.; Herman, G. S.; Selloni, A. *Catal. Today* **2003**, *85*, 93.

- [6] Shklover, V.; Nazeeruddin, M. K.; Zakeeruddin, S. M.; Barbé, C.; Kay, A.; Haibach, T.; Steurer, W.; Hermann, R.; Nissen, H. U.; Grätzel, M. *Chem. Mater.* **1997**, *9*, 430.
- [7] Lazzeri, M.; Vittadini, A.; Selloni, A. *Phys. Rev. B* **2002**, *65*, 119901.
- [8] Diebold, U. *Surf. Sci. Rep.* **2003**, *48*, 53.
- [9] Hebenstreit, W.; Ruzycski, N.; Herman, G. S.; Gao, Y. F.; Diebold, U. *Phys. Rev. B* **2000**, *62*, R16334.
- [10] Liang, Y.; Gan, S.; Chambers, S. A.; Altman, E. I. *Phys. Rev. B* **2001**, *63*, 235402.
- [11] Herman, G. S.; Dohnálek, Z.; Ruzycski, N.; Diebold, U. *J. Phys. Chem. B* **2003**, *107*, 2788.
- [12] Morterra, C. J. *Chem. Soc. Faraday. Trans. 1* **1988**, *84*, 1617.
- [13] Beck, D. D.; White, J. M.; Ratcliffe, C. T. *J. Phys. Chem.* **1986**, *90*, 3123.
- [14] Yang, H. G.; Sun, C. H.; Qiao, S. Z.; Zou, J.; Liu, G.; Smith, S. C.; Cheng, H. M.; Lu, G. Q. *Nature* **2008**, *453*, 638.
- [15] Yang, H. G.; Liu, G.; Qiao, S. Z.; Sun, C. H.; Jin, Y. G.; Smith, S. C.; Zou, J.; Cheng, H. M.; Lu, G. Q. *J. Am. Chem. Soc.* **2009**, *131*, 4078.
- [16] Han, X. G.; Kuang, Q.; Jin, M. S.; Xie, Z. X.; Zheng, L. S. *J. Am. Chem. Soc.* **2009**, *131*, 3152.

- [17] Dai, Y. Q.; Cobley, C. M.; Zeng, J.; Sun, Y. M.; Xia, Y. N. *Nano. Lett.* **2009**, *9*, 2455.
- [18] Amano, F.; Prieto-Mahaney, O. O.; Terada, Y.; Yasumoto, T.; Shibayama, T.; Ohtani, B. *Chem. Mater.* **2009**, *21*, 2601.
- [19] Polshettiwar, V.; Varma, R. S. *Chem. Soc. Rev.* **2008**, *37*, 1546.
- [20] Loupy, A.; Varma, R. S. *Chim. Oggi.* **2006**, *24*, 36.
- [21] Hart, J. N.; Menzies, D.; Cheng, Y. B.; Simon, G. P.; Spiccia, L. *Sol. Energy Mater. Sol. Cells* **2007**, *91*, 6.
- [22] Komarneni, S.; Rajha, R. K.; Katsuki, H. *Mater. Chem. Phys.* **1999**, *61*, 50.
- [23] Hart, J. N.; Cervini, R.; Cheng, Y. B.; Simon, G. P.; Spiccia, L. *Sol. Energy Mater. Sol. Cells* **2004**, *84*, 135.
- [24] Wu, X.; Jing, Q. Z.; Ma, Z. F.; Fu, M.; Shangguan, W. F. *Solid State Commun.* **2005**, *136*, 513.
- [25] Addamo, M.; Bellardita, M.; Carriazo, D.; Paola, A. D.; Milioto, S.; Palmisano, L.; Rives, V. *Appl. Catal. B: Environ.* **2008**, *84*, 742.
- [26] Murugan, A. V.; Samuel, V.; Ravi, V. *Mater. Lett.* **2006**, *60*, 479.
- [27] Jaroenworarluck, A.; Panyathanmaporn, T.; Soontornworajit, B.; Supothina, S. *Surf. Interf. Anal.* **2006**, *38*, 765.

- [28] Jia, X.; He, W.; Zhang, X.; Zhao, H.; Li, Z.; Feng, Y. *Nanotechnology* **2007**, *18*, 075602.
- [29] Wilson, G. J.; Will, G. D.; Frost, R. L.; Montgomery, S. A. *J. Mater. Chem.* **2002**, *12*, 1787.
- [30] Wilson, G. J.; Matijasevich, A. S.; Mitchell, D. R. G.; Schulz, J. C.; Will, G. D. *Langmuir* **2006**, *22*, 2016.
- [31] Bonhote, P.; Dias, A. P.; Papageorgiou, N.; Kalyanasundaram, K.; Gratzel, M. *Inorg. Chem.* **1996**, *35*, 1168.
- [32] Huddleston, J. G.; Visser, A. E.; Reichert, W. M.; Willauer, H. D.; Broker, G. A.; Rogers, R. D. *Green Chem.* **2001**, *3*, 156.
- [33] Nakashima, T.; Kimizuka, N. *J. Am. Chem. Soc.* **2003**, *125*, 6386.
- [34] Kaper, H.; Endres, F.; Djerdj, I.; Antonietti, M.; Smarsly, B. M.; Maier, J.; Hu, Y. S. *Small* **2007**, *3*, 1753.
- [35] Zhou, Y.; Antonietti, M. *J. Am. Chem. Soc.* **2003**, *125*, 14960.
- [36] Hoffmann, J.; Nüchter, M.; Ondruschka, B.; Wasserscheid, P. *Green Chem.* **2003**, *5*, 296.
- [37] Leadbeater, N. E.; Torenius, H. M. *J. Org. Chem.* **2002**, *67*, 3145.
- [38] Ding, K. L.; Miao, Z. J.; Liu, Z. M.; Zhang, Z. F.; Han, B. X.; An, G. M.; Miao, S. D.; Xie, Y. *J. Am. Chem. Soc.* **2007**, *129*, 6362.

- [39] Zhang, D. Q.; Li, G. S.; Yang, X. F.; Yu, J. C. *Chem. Commun.* **2009**, 4381.
- [40] Holbrey, J. D.; Seddon, K. R. *Dalton Trans.* **1999**, 2133.
- [41] Huang, Y.; Ho, W. K.; Lee, S. C.; Zhang, L. Z.; Li, G. S.; Yu, J. C. *Langmuir* **2008**, *24*, 3510.
- [42] Ho, W. K.; Yu, J. C. *J. Mol. Catal. A: Chem.* **2006**, *247*, 268.
- [43] Barnard, A. S.; Zapol, P. *J. Phys. Chem. B* **2003**, *108*, 18435.
- [44] Lazzeri, M.; Vittadini, A.; Selloni, A. *Phys. Rev. B* **2001**, *63*, 155409.
- [45] Jun, Y.; Casula, M. F.; Sim, J. H.; Kim, S. Y.; Cheon, J. W.; Alivisatos, A. P. *J. Am. Chem. Soc.* **2003**, *125*, 15981.
- [46] Lou, X. W.; Zeng, H. C. *J. Am. Chem. Soc.* **2003**, *125*, 2697.
- [47] Yu, J. C.; Yu, J. G.; Ho, W. K.; Jiang, Z. T.; Zhang, L. Z. *Chem. Mater.* **2002**, *14*, 3808.
- [48] Tsuji, M.; Hashimoto, M.; Nishizawa, Y.; Kubokawa, M.; Tsuji, T. *Chem. Eur. J.* **2005**, *11*, 440.
- [49] Fischer, S. L.; Koshland, C. P. *Environ. Sci. Technol.* **2007**, *41*, 3121.
- [50] Li, G. S.; Zhang, D. Q.; Yu, J. C. *Phys. Chem. Chem. Phys.* **2009**, *11*, 3775.
- [51] Yu, J. C.; Li, G. S.; Wang, X. C.; Hu, X. L.; Leung, C. W.; Zhang, Z. D. *Chem. Commun.* **2006**, 2717.

- [52] Li, H. X.; Bian, Z. F.; Zhu, J.; Zhang, D. Q.; Li, G. S.; Huo, Y. N.; Li, H.; Lu, Y. *F. J. Am. Chem. Soc.* **2007**, *129*, 8406.
- [53] Li, G. S.; Zhang, D. Q.; Yu, J. C. *Chem. Mater.* **2008**, *20*, 3983.
- [54] Ai, Z. H.; Ho, W. K.; Lee, S. C.; Zhang, L. Z. *Environ. Sci. Technol.* **2009**, *43*, 4143.
- [55] Gong, X. Q.; Selloni, A. *J. Phys. Chem. B* **2005**, *109*, 19560.
- [56] Vittadini, A.; Selloni, A.; Rotzinger, F. P.; Gratzel, M. *Phys. Rev. Lett.* **1998**, *81*, 14.
- [57] Selloni, A. *Nat. Mater.* **2008**, *7*, 613.
- [58] Li, G. S.; Zhang, D. Q.; Yu, J. C. *Environ. Sci. Technol.* **2009**, *43*, 7079.
- [59] Grainger, D. W.; Castner, D. G. *Adv. Mater.* **2008**, *20*, 867.
- [60] Oberdorster, G.; Oberdorster, E.; Oberdorster, J. *Environ. Health. Perspect.* **2005**, *113*, 823.
- [61] King-Heiden, T. C.; Wicinski, P. N.; Mangham, A. N.; Metz, K. M.; Nesbit, D. Pedersen, J. A.; Hamers, R. J.; Heideman, W.; Peterson, R. E. *Environ. Sci. Technol.* **2009**, *43*, 1605.

Chapter Six

A Micrometer-Size TiO₂ Single Crystal Photocatalyst with Remarkable 80 % Reactive Facets

6.1 Introduction

Different facets of a single crystal exhibit distinctive physical and chemical properties.¹ Chemical properties of definite crystal planes by employing bulk single crystal have been widely studied over the past decades.² However, for TiO₂, a promising photocatalyst,³ most studies are focused on controlling the nanostructure or crystal phase for potential use.⁴ There are very few investigations on the relationship between definite facets of bulk anatase TiO₂ single crystal and chemical activities.⁵ This is due to the difficulty in synthesizing large anatase TiO₂ single crystals with well-defined ($\{101\}$ or $\{001\}$) facets. Up to now, most of the reported anatase TiO₂ single crystals had either no $\{001\}$ facets or the $\{101\}$ facets dominated the surface.^{6,7} This is because the average surface energy of anatase TiO₂ for $\{001\}$ facets (0.90 J m^{-2}) is double than that of $\{101\}$ facets (0.44 J m^{-2}). As a consequence, facets having high surface energy diminish quickly for minimization of surface

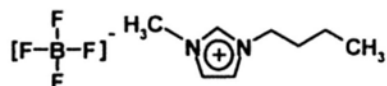
energy during a crystal growth process. Lu and co-workers overcame the technical difficulties and synthesized micro-sized anatase TiO₂ single crystals with reactive {001} facets.⁸ These relatively large TiO₂ single crystals should be very useful as model single crystals for fundamental studies in surface science. They also exhibited promising applications in solar cells, photonic and optoelectronic devices, sensors and photocatalysis. However, the percentage of {001} facets achieved was only 47 %. Further increasing the percentage of {001} facets proved difficult. Recently, anatase TiO₂ with more than 47 % reactive {001} facets was observed.⁹ However, these crystals were nano-sized particles (30-130 nm) instead of large single crystals. Very recently, Lu and co-workers improved their work by adding a synergistic capping agent to increase the percentage of {001} facets to 64 %.¹⁰ It should be noted that all the currently available approaches require the use of an extremely corrosive and toxic hydrofluoric acid. This is against the principle of “green chemistry”. Therefore, a novel and green synthetic method that realizes an even higher percentage of {001} facets is highly desirable.

Ionic liquids (ILs) have been actively investigated as an environmentally benign solvent media, especially for the synthesis of inorganic materials.¹¹ For example, Nakashima and Kimizuka found that ILs could provide an easy access to hollow TiO₂ microspheres.¹² Smarsly and colleagues used ILs for low-temperature synthesis

of both anatase and rutile TiO₂.¹³ Although the synthesis of small TiO₂ nanocrystals in ionic liquids has been reported,¹⁴ the fabrication of large micro-sized anatase single crystals is much more difficult. This is because anatase TiO₂ is a thermodynamically metastable phase and rutile TiO₂ is the most stable phase.¹⁵ To the best of our knowledge, large micro-sized (>1.5 μm) anatase TiO₂ single crystals with more than 64 % exposed {001} facets have never been synthesized.

Herein, we report a simple and novel green synthetic route for the preparation of a micro-sheet anatase TiO₂ single crystal photocatalyst with remarkable 80 % reactive {001} facets. The high reactivity of {001} facets make these single crystals highly photocatalytically active.⁹ They are easily recyclable and thermally stable up to 800 °C.

The products were prepared by a microwave-assisted method involving an aqueous solution of titanium tetrafluoride and a tetrafluoroborate-based ionic liquid (Experimental details are shown in Supporting Information). The chemical structure of the ionic liquid, 1-butyl-3-methyl-imidazolium-tetrafluoroborate, is shown below.



Microwave heating provides energy to the reactants by means of the molecular interaction with high frequency electromagnetic radiation, which is different from that of conventional thermal treatment.¹⁶ Microwave-assisted fabrication of TiO₂ can

reduce the time required for the synthesis and increase the crystallinity of the product.¹⁷

6.2 Experimental Section

6.2.1 Preparation of TiO₂ with Reactive Facets

In a typical synthesis, 0.02 mol/L titanium tetrafluoride (ACROS) aqueous solution was prepared by dissolving 0.62 g titanium tetrafluoride in 250 mL D.I. water which contains 0.2 mL hydrochloric acid (37 %, MERCK, Germany). Then 1 mL ionic liquid 1-butyl-3-methylimidazolium tetrafluoroborate ([bmin]⁺[BF₄]⁻), purchased from International Laboratory, USA, was added to 30 mL 0.02 mol/L titanium tetrafluoride aqueous solution under stirring. The mixture was sealed in a Teflon-lined double-walled digestion vessel. After treating at 210 °C for 90 min using a microwave digestion system (Ethos TC, Milestone), the vessel was then cooled down to room temperature. The product was collected by centrifugation, washed with deionised water and absolute ethanol, and dried in a vacuum at 80 °C for 4 h.

For comparison, ordinary anatase TiO₂ single-crystals were prepared by adding 5 mL TiCl₄ (ACROS) into a conical flask which contains 40 mL N₂ (l) and 15 mL H₂O. After evaporation of N₂ (l), the clear colourless TiCl₄ solution was used as the stock

solution. Then 2 mL stock solution and 2 mL 1-methylimidazolium tetrafluoroborate were added into 48 mL D.I. water under stirring. After treating at a controllable temperature of 210 °C for 90 min using a microwave digestion system (Ethos TC, Milestone), the solution was then cooled down to room temperature. Finally, the product was collected by centrifugation, washed with deionised water and absolute ethanol, and dried in a vacuum at 80 °C for 4 h.

6.2.2 Measurement of Photocatalytic Activity

The photocatalytic activities of the anatase TiO₂ single-crystals were measured by the degradation of 4-chlorophenol in an aqueous solution. The photodegradation experiments were carried out at 25 °C in a 150 ml reactor containing 0.08 g catalyst calcined at 600 °C for 90 min and 60 mL of 10 ppm 4-chlorophenol aqueous solution. A 300 W high-pressure mercury vapor lamp was used as the UV light source, which was mounted at 5 cm around the solution. Vigorous stirring (900 rpm) was employed to ensure the adsorption equilibrium and to eliminate any diffusion effect. The equilibrium 4-chlorophenol concentration was used as the initial concentration of 4-chlorophenol.

The photocatalysis was started by irradiating the reaction mixture with UV light. The reaction time was 2 h. The concentrations of 4-chlorophenol and its degradation

products were measured with a HPLC system (Waters Baseline 810) with a Waters 486 tunable UV absorbance detector. A Supelco LC-18-DB column (250 mm×4.6 mm) was applied. The eluent consisted of a 40:60 methanol:water mixture, and the flow rate was 1 mL/min. The aromatic compounds were detected at 220 nm. Millipore discs were used to separate the catalysts before analysis of the solution. The reproducibility was checked by repeating the runs at least three times and was found to be within acceptable limits ($\pm 5\%$). The blank experiment shows the 4-chlorophenol degradation was less than 2%. Conventional anatase TiO₂ single crystals were used as a reference to compare the activities under the same experimental conditions.

6.2.3 Characterization

X-ray diffraction (XRD) patterns were recorded using a Bruker D8 Advance diffractometer with high-intensity CuK α irradiation ($\lambda = 1.5406 \text{ \AA}$). Transmission electron microscopy (TEM) observations were carried out on a Tecnai F20 microscope (FEI, 200 kV). The general morphology of the products was characterized by scanning electron microscopy (FEI Quanta 400 FEG microscopes).

6.3 Results and Discussion:

6.3.1 FESEM, TEM and XRD Analysis

Field emission scanning electron microscopy (FESEM) images of the as-prepared sample are shown in Fig. 6.1a. Evidence from the side-view FESEM image (Fig. 6.2) gives us a simulated model (Fig. 6.1b) of these crystals. The products consist of well-defined sheet-shaped structure with a square outline, side length of 2 μm . They are highly truncated bipyramids in shape. The X-ray diffraction (XRD) pattern (Fig. 6.3) of the sample matches well with the standard pattern of anatase (JCPDS 21-1272). Moreover, there is no observable diffraction peaks at 27° or 31° , indicating that the single crystals are free of rutile or brookite impurities phases. The narrow peaks indicate a very good crystallinity. According to the symmetries of anatase TiO_2 , the two square surfaces are the $\{001\}$ facets and the eight isosceles trapezoidal surfaces are the $\{101\}$ facets of anatase TiO_2 . The ratio of the highly reactive $\{001\}$ facets to total surface area can be calculated from the degree of truncation⁸ (The detailed calculations can be found in Fig. 6.4). The degree of truncation is 0.95 with relative standard deviation of 3.2 %. We estimate the percentage of $\{001\}$ facets to be 80 %. Transmission electron microscopy (TEM) and selected-area electron diffraction (SAED) patterns (Fig. 6.1c and 6.1d) confirm that these anatase crystal

blocks have the representative single-crystal characteristics. The SAED patterns can be indexed into diffraction spots of the $[001]$ zone. The high-resolution TEM image (HRTEM) (Fig. 6.1e) shows the (200) and (020) atomic planes with a lattice spacing of 0.189 nm and an interfacial angle of 90° .⁸

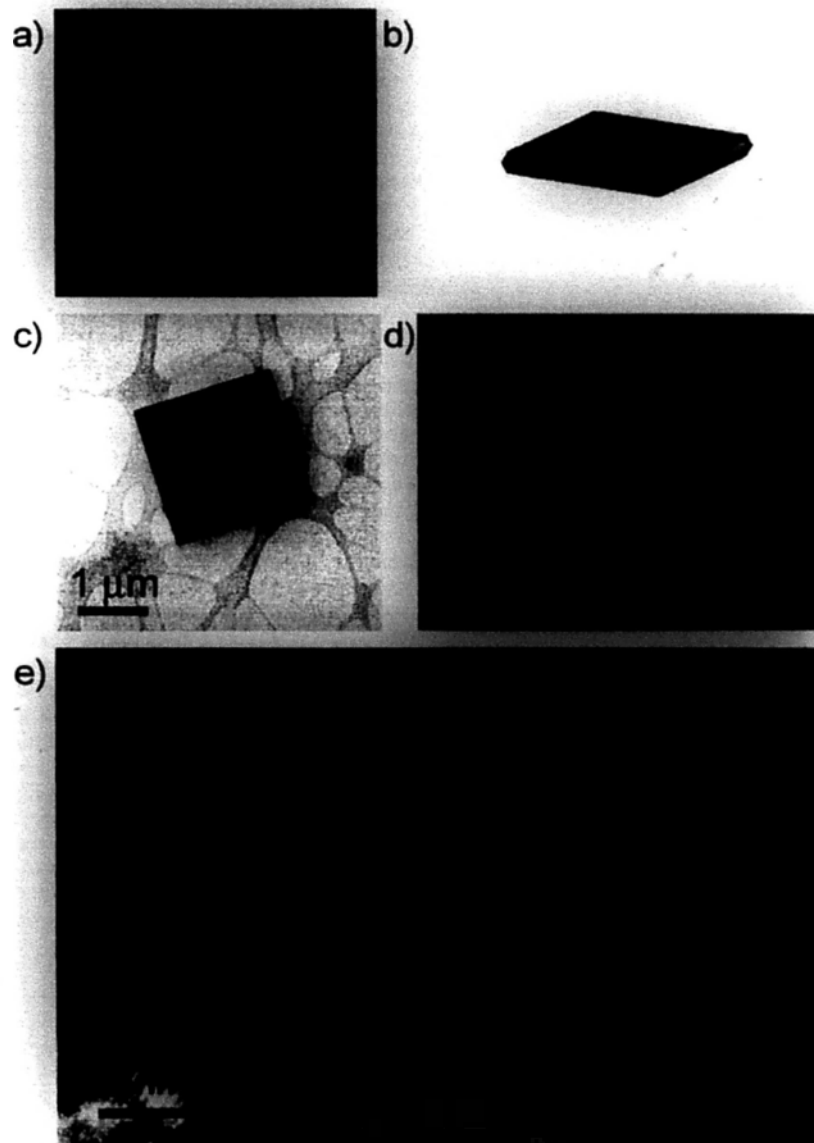


Figure 6.1 FESEM image a), Simulated model b), TEM image of a representative anatase single crystal recorded along the $[001]$ axis c), SAED pattern d) and HRTEM image e) of the anatase TiO_2 exposed with reactive $\{001\}$ facets.



Figure 6.2 Side-view FESEM images of the anatase single crystals exposed with {001} facets.

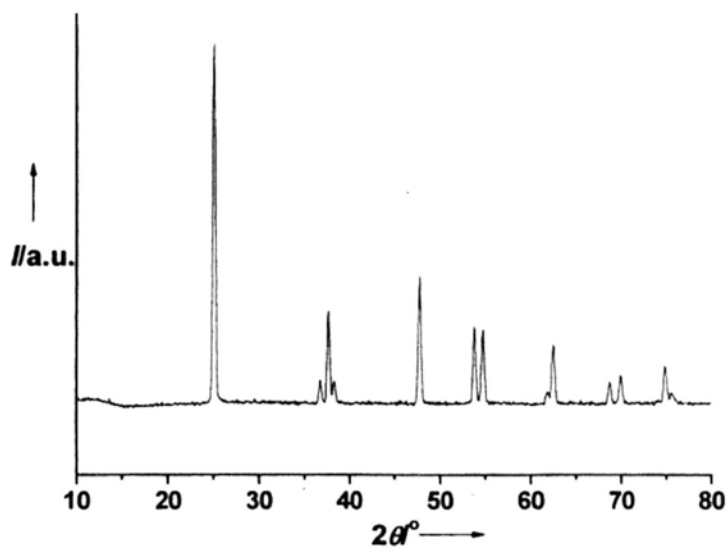


Figure 6.3 XRD pattern of the anatase single crystal exposed with {001} facets.

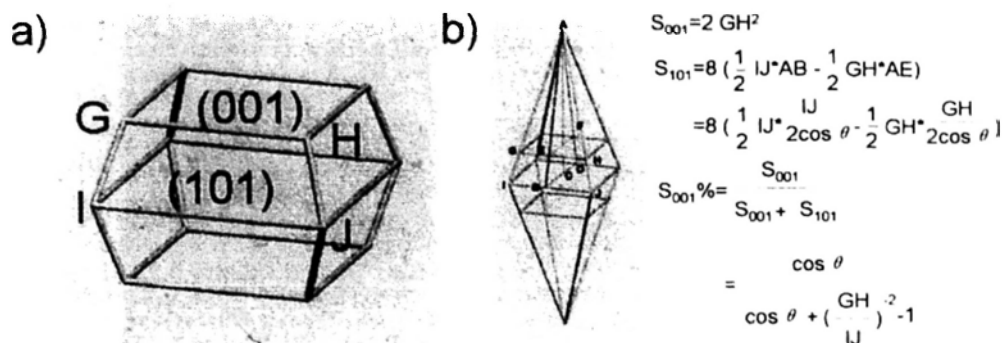


Figure 6.4 a) Simulated shape of the TiO₂ anatase single crystal samples. b) Equilibrium shape of anatase TiO₂ crystal. c) the calculation process of S₀₀₁ . is the theoretical value for the angle between the [001] and [101] facets of anatase, GH/IJ is the degree of truncation).

6.3.2 The role of Ionic Liquid

First-principles calculations indicate that fluorine ions can greatly reduce the surface energy of {001} facets, making them more stable than the {101} facets.⁸ This is due to the low F-F binding energy (158.8 kJ mol⁻¹) and high F-Ti binding energy (569.0 kJ mol⁻¹) that can significantly lower the energy of the (001) surfaces, making them more stable than the (101) surfaces. The anion of the ionic liquid used in this work is [BF₄]⁻. It has 4 fluorine atoms in one molecule. Such structure can create a fluorine rich environment on the crystal surface compared to the system in which HF is used as a fluorine source.⁸ As shown in Fig. 6.5, the more bulky [BF₄]⁻ groups protect and stabilize the (001) surface. Therefore, the preferred growth of the {001} facets is promoted.

Experiments were carried out to clarify the role of ionic liquid in forming {001} exposed single crystal TiO₂. Fig. 6.6a shows the TEM image of the sample synthesized without the ionic liquid. Only hollow anatase TiO₂ nanospheres were obtained. The XRD pattern indicates the low anatase crystallinity (Fig. 6.6c). Therefore, we can conclude that the ionic liquid 1-butyl-3-methylimidazolium tetrafluoroborate is not only favourable for improving anatase crystallinity, but also beneficial for exposing the {001} facets. Ionic liquid, as an excellent microwave-absorbent,^{18,19} can greatly enhance the microwave-absorbing efficiency of the reaction system to promote the crystallization of anatase TiO₂.

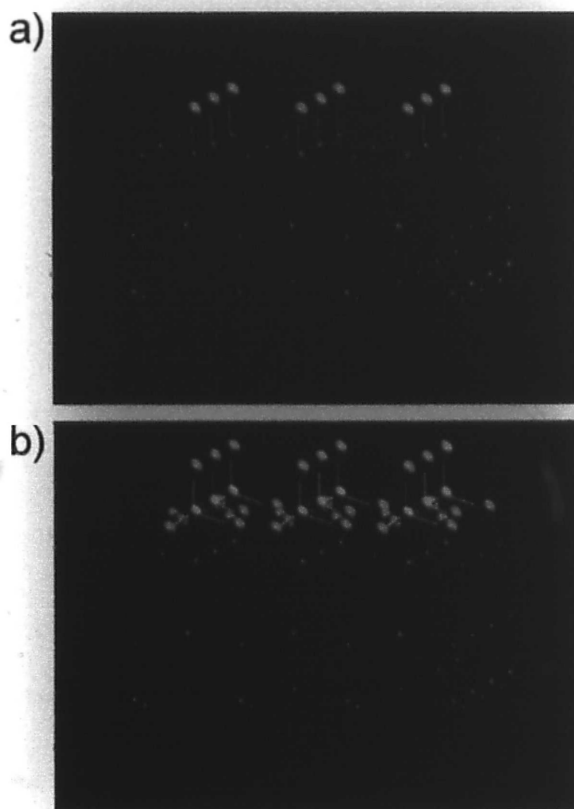


Figure 6.5 F-(001) surfaces of anatase single crystal using. a) HF and b) ionic liquid as the morphology controlling agent. The purple planes are the {001} facets. The elements O, Ti, F and B are shown in red, blue, yellow and white.

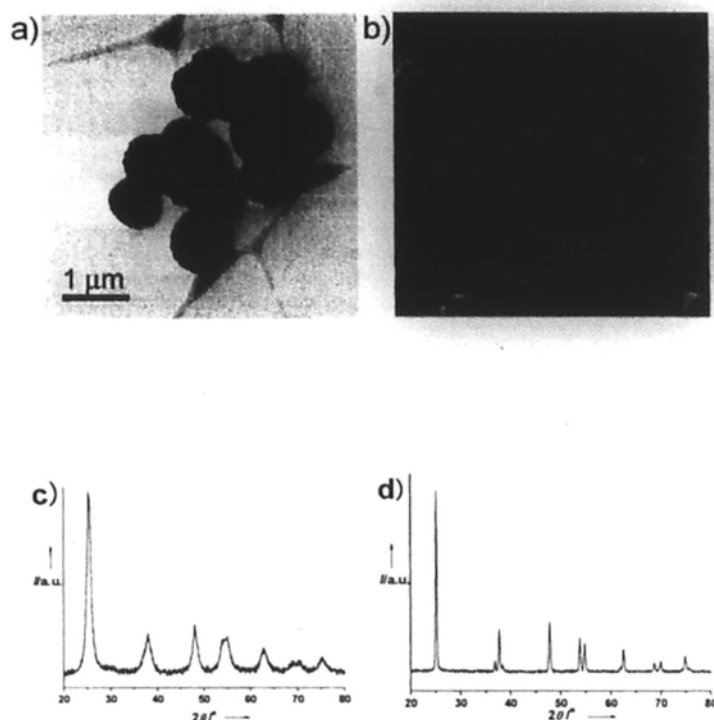


Figure 6.6 SEM image a) and XRD pattern c) of the anatase hollow spheres prepared without ionic liquid. SEM image b) and XRD pattern d) of the {001} unexposed TiO₂ single crystals.

6.3.3 Photocatalytic Activity

These anatase TiO₂ single crystals are expected to have higher reactivity due to the large percentage of {001} facets compared with the crystals having normal majority {101} facets. For applying these crystals in photocatalytic reaction, the fluorated surfaces must first be cleaned with a heat treatment at 600 °C, without altering the morphology. The activity of semiconductor photocatalysts depends on physicochemical properties, such as specific surface area, composition and crystal size.²⁰ The commercially available photocatalyst P25 (Degussa) is not suitable as a

standard to compare with due to the distinct size difference.²¹ Herein, {001} unexposed TiO₂ single crystals (shown in Fig. 6.6b,d), having almost the same specific surface area (0.5 m² g⁻¹), particle size and crystallinity as those truncated bipyramid shape anatase single crystals, were used as a standard to decompose 4-chlorophenol. The photodegradation experiments were carried out at 25 °C in a 150 ml reactor containing 0.08 g catalyst and 60 mL of 10 ppm 4-chlorophenol aqueous solution. A 300 W high-pressure mercury vapor lamp was used as the UV light source. The reaction time was 2 h. As shown in Fig. 6.7, the anatase single crystals exposed with {001} facets exhibit much higher activities than that of the {001} unexposed TiO₂ single crystals. This suggests that the reactive {001} facets play an important role in the photocatalytic reaction owing to their strong ability to dissociatively adsorb water to form hydrogen peroxide and peroxide radicals.^{5,22} It is obvious that the photoreactivity can be enhanced from 40.0 % to 84.5 % with increasing the percentage of {001} facets. Furthermore, the sheet-like micro-sized single crystals maintain the high photocatalytic activity even after eight cycles as shown in Fig. 6.8. This is because the micro-sized anatase TiO₂ single crystals are easily recovered through a gravitational settling.

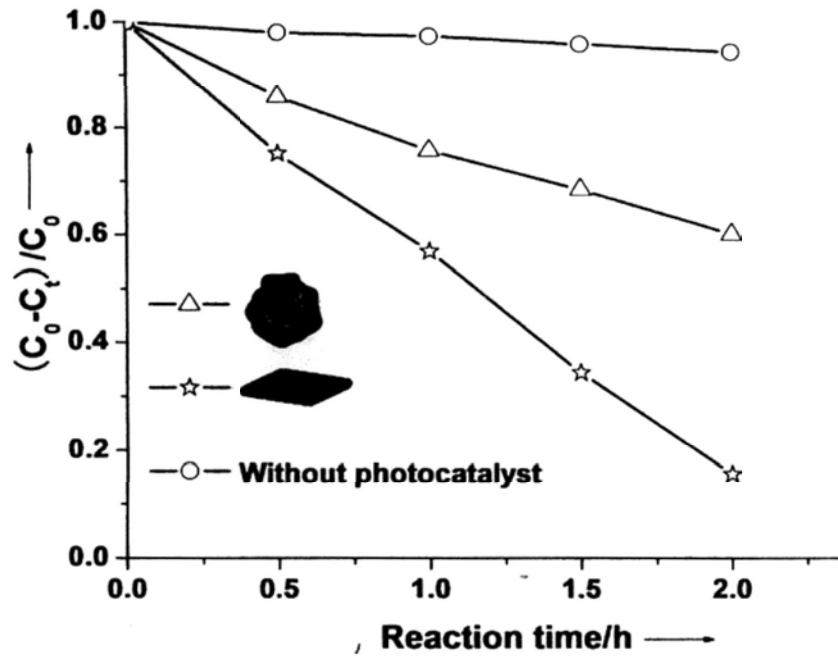


Figure 6.7 The effectiveness of samples with (-☆-) or without (-△-)exposed reactive {001} facets on the degradation of 4-chlorophenol under UV irradiation.

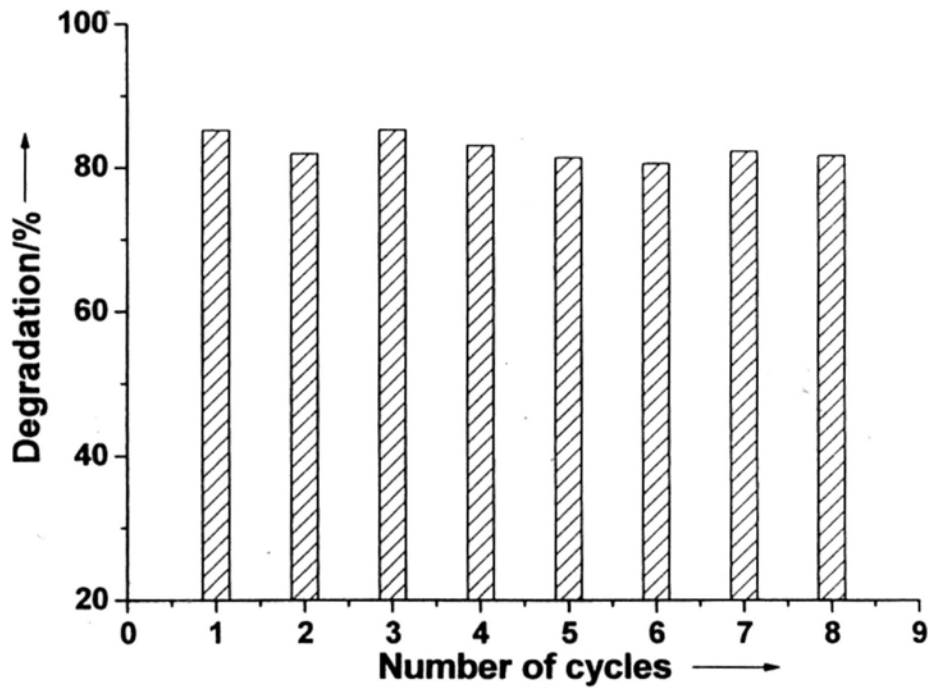


Figure 6.8 The recycle experiments of anatase TiO₂ single crystal exposed with {001} facets.

6.3.4 Thermal Stability Study

It is worthy to note that these {001} exposed TiO₂ single crystals are thermally stable up to 800 °C (Fig. 6.9). This temperature is much higher than the phase-transfer temperature of 500 °C²³ from anatase to thermodynamically stable rutile for the amorphous TiO₂ prepared by conventional method (Fig. 6.9). Such stable anatase TiO₂ single crystals are useful in high temperature catalysis or photo-electronic applications.

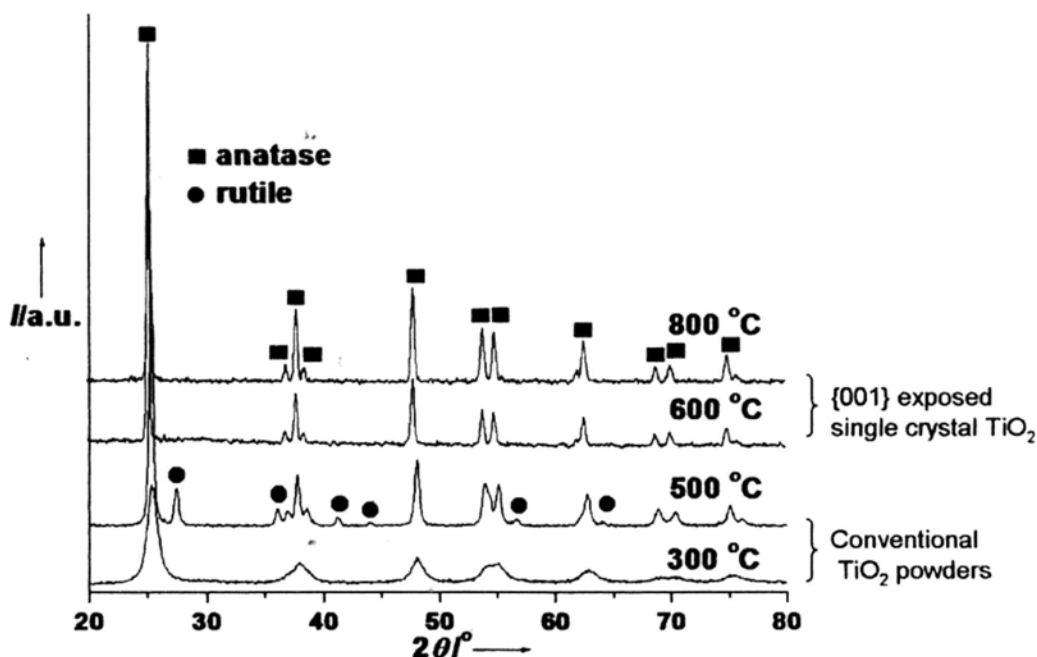


Figure 6.9 XRD patterns of a) anatase single crystals exposed with {001} facets and b) TiO₂ powders prepared by conventional, sol-gel method calcined at different temperatures.

6.4 Conclusion

In conclusion, relatively large micrometer-size anatase TiO₂ single crystals with remarkable 80 % reactive facets were prepared by a microwave-enhanced method with the assistance of an ionic liquid. The anion of the ionic liquid ([BF₄]⁻) offers a strong stabilization effect that promotes the growth along the {001} facets. The high percentage of the reactive facets make these single crystals highly photocatalytically active.

6.5 References

- [1] Tian, N.; Zhou, Z. Y.; Sun, S. G.; Ding, Y.; Wang, Z. L. *Science* **2007**, *316*, 732.
- [2] (a) Kiskinova, M. *Chem. Rev.* **1996**, *96*, 1431; (b) Somorjai, G. A. *Chem. Rev.* **1996**, *96*, 1223; (c) Seker, F.; Meeker, K.; Kuech, T. F.; Ellis, A. B. *Chem. Rev.* **2000**, *100*, 2505.
- [3] (a) Fujishima, A.; Honda, K. *Nature* **1972**, *238*, 37; (b) Fujihiram, M.; Satoh, Y.; Osa, T. *Natur* **1981**, *293*, 206; (c) Zhang, J.; Xu, Q.; Feng, Z. C.; Li, M. J.; Li, C. *Angew. Chem. Int. Ed.* **2008**, *47*, 1766; (d) Li, H. X.; Bian, Z. F.; Zhu, J.; Zhang, D. Q.; Li, G. S.; Huo, Y. N.; Li, H.; Lu, Y. F. *J. Am. Chem. Soc.* **2007**, *129*, 8406; (e) Sun, F. Q.; Yu, J. C.; Wang, X. C. *Chem. Mater.* **2006**, *18*, 3774; (f) Yu, J. C.; Li, G. S.; Wang, X. C.; Hu, X. L.; Leung, C. W.; Zhang, Z. D. *Chem. Commun.*

2006, 2717.

- [4] (a) Zhang, Z. H.; Zhong, X. H.; Liu, S. H.; Li, D. F.; Han, M. Y. *Angew. Chem. Int. Ed.* **2005**, *44*, 3466; (b) Shrestha, N. K.; Macak, J. M.; Schmidt-Stein, F.; Hahn, R.; Mierke, C. T.; Fabry, B.; Schmuki, P. *Angew. Chem. Int. Ed.* **2009**, *48*, 969; (c) Weatherspoon, M. R.; Cai, Y.; Crne, M.; Srinivasarao, M.; Sandhage, K. H. *Angew. Chem. Int. Ed.* **2008**, *47*, 7921; (d) Tomita, K.; Petrykin, V.; Kobayashi, M.; Shiro, M.; Yoshimura, M.; Kakihana, M. *Angew. Chem. Int. Ed.* **2006**, *45*, 2378; (e) Kawahara, T.; Konishi, Y.; Tada, H.; Tohge, N.; Nishii, J.; Ito, S. *Angew. Chem. Int. Ed.* **2002**, *41*, 2811.
- [5] Gong, X. Q.; Selloni, A. *J. Phys. Chem. B* **2005**, *109*, 19560.
- [6] Berger, H.; Tang, H.; Lévy, F. *J. Cryst. Growth* **1993**, *130*, 108.
- [7] Hosono, E.; Fujihara, S.; Imai, H.; Honma, I.; Masaki, I.; Zhou, H. S. *ACS nano* **2008**, *1*, 273.
- [8] Yang, H. G.; Sun, C. H.; Qiao, S. Z.; Zou, J.; Liu, G.; Smith, S. C.; Cheng, H. M. Lu, G. Q. *Nature* **2008**, *453*, 638.
- [9] Han, X. G.; Kuang, Q.; Jin, M. S.; Xie, Z. X.; Zheng, L. S. *J. Am. Chem. Soc.* **2009**, *131*, 3152.
- [10] Yang, H. G.; Liu, G.; Qiao, S. Z.; Sun, C. H.; Jin, Y. G.; Smith, S. C.; Zou, J.; Cheng, H. M.; Lu, G. Q. *J. Am. Chem. Soc.* **2009**, *131*, 4078.

- [11] Dupont, J.; de Souza, R. F.; Suarez, P. A. Z. *Chem. Rev.* **2002**, *102*, 3667.
- [12] Nakashima, T.; Kimizuka, N. *J. Am. Chem. Soc.* **2003**, *125*, 6386.
- [13] Kaper, H.; Endres, F.; Djerdj, I.; Antonietti, M.; Smarsly, B. M.; Maier, J.; Hu, Y. *S. Small* **2007**, *3*, 1753.
- [14] Zhou, Y.; Antonietti, M. *J. Am. Chem. Soc.* **2003**, *125*, 14960.
- [15] Barnard, A. S.; Curtiss, L. A.; *Nano Lett.* **2005**, *5*, 126
- [16] Pol, V. G.; Langzam, Y.; Zaban, A. *Langmuir* **2007**, *23*, 11211.
- [17] Addamo, M.; Bellardita, M.; Carriazo, D.; Paola, A. D.; Milioto, S.; Palmisano, L.; Rives, V. *Appl. Catal. B: Environ.* **2008**, *84*, 742.
- [18] Alterman, M.; Hallberg, A. *J. Org. Chem.* **2000**, *65*, 7984.
- [19] Hoffmann, J.; Nüchter, M.; Ondruschka, B.; Wasserscheid, P. *Green Chem.* **2003**, *5*, 296.
- [20] (a) Lidström, P.; Tierney, J.; Wathey, B.; Westman, J. *Tetrahedron* **2001**, *57*, 9225;
(b) Amano, F.; Yamakata, A.; Nogami, K.; Osawa, M.; Ohtani, B. *J. Am. Chem. Soc.* **2008**, *130*, 17650.
- [21] Nuechter, M.; Ondruschka, B.; Jungnickel, A.; Mueller, U. *J. Phys. Org. Chem.* **2000**, *13*, 579.
- [22] (a) Vittadini, A.; Selloni, A.; Rotzinger, F. P.; Gratzel, M. *Phys. Rev. Lett.* **1998**, *81*, 14; (b) Selloni, A. *Nat. Mater.* **2008**, *7*, 613; (c) Bredow, T.; Jug, K. *J. Phys.*

Chem. **1995**, *99*, 285.

[23] (a) Perera, S.; Gillan, E. G. *Chem. Commun.* **2005**, 5988; (b) Ovenstone, J.;

Yanagisawa, K. *Chem. Mater.* **1999**, *11*, 2770.

Chapter Seven

Green Synthesis of a Self-Assembled Rutile Mesocrystalline Photocatalyst

7.1 Introduction

Mesocrystals are oriented superstructures or colloidal crystals composed of individual nanocrystals that align in a common crystallographic fashion.¹ Many mesocrystals built from three-dimensional (3D) and well-aligned nanocrystals have been prepared. These include CeO_2 ,² CaCO_3 ,³ BaCrO_4 ⁴ and even metals.^{5,6} These 3D hierarchical structures can bring forth new properties.^{7,8} Titanium dioxide has been intensively studied in recent years for its applications in photocatalysis, solar cells and self-cleaning coatings.⁹⁻¹⁶ For the synthesis of anatase TiO_2 mesocrystals, templates such as carbon nanotubes are often used as the support.¹⁷ The fabrication of rutile TiO_2 mesocrystals unavoidably requires large amounts of organic solvents or expensive biological additives as morphology-controlling agents.^{18,19} The high cost and complicated procedures limit the TiO_2 mesocrystals from being used on a large scale. Therefore, the development of a green and sustainable pathway for the

preparation of TiO₂ is of considerable general interest.

Microwave heating is emerging as a rapid and environmentally friendly mode of heating for the generation of nanomaterials.^{20,21} Here we present an efficient and green approach for the preparation of rutile TiO₂ mesocrystal by heating titanium(III) chloride at 200 °C for 1 minute under microwave irradiation. As no templates or organic additives are involved in the system, we believe it is the greenest way to fabricate TiO₂ mesocrystals. Importantly, the products exhibit a high solar-light-driven photocatalytic oxidation rate for nitric oxide, a gaseous air pollutant which is responsible for photochemical smog and acid rain.

7.2 Experimental Section

7.2.1 Preparation of Photocatalysts

Titanium(III) chloride (solution about 15 % in about 10 % hydrochloric acid, for synthesis) was purchased from Merck-Schuchardt and used as received. 10 mL Titanium(III) chloride was sealed in a Teflon-lined double-walled digestion vessel. It was treated at 200 °C for 1 min with a heating rate 24 °C/min in a microwave digestion system (Ethos TC, Milestone). The reaction vessel was fitted with a temperature probe that was housed in a sturdy thermowell. The desired time and temperature were programmed by using Milestone's EasyControl software. The

temperature of the bulk reaction solution was monitored, and the preset profile was followed automatically by continuously adjusting the applied power. After the reaction the product was collected through centrifugation. Then the white precipitates were washed with water until $\text{pH} = 7$ and then dried in vacuum at $60\text{ }^{\circ}\text{C}$ for 4 h. For the synthesis of gold doped rutile sample, 0.13 g TiO_2 powder, 31 mL H_2O , 0.01 M $\text{HAuCl}_4 \cdot 4\text{H}_2\text{O}$ aqueous solution, and 2 mL methanol were mixed together under stirring. Then the mixture was irradiated with UV light for 20 min. The precipitate was collected through centrifugation. After washing and drying, a light purple Au doped TiO_2 product was obtained.

7.2.2 Characterization

Wide-angle X-ray diffraction measurements (XRD) were carried out using a Bruker D8 Advance X-ray diffractometer with Cu-K α radiation. The N_2 -sorption isotherms were recorded at 77 K using a Micromeritics ASAP 2010 instrument. The Brunauer–Emmett–Teller (BET) approach was used for the determination of the surface area. Standard transmission electron microscopy images (TEM) and high-resolution transmission electron microscopy images (HRTEM) were recorded by a JEOL-2010F at 200 kV. The scanning electron microscopy (SEM) images were taken on a FEI Quanta 400 FEG microscope. The diffuse reflectance spectra were

recorded by a Varian Cary 100 Scan UV-vis system. X-ray photoelectron spectroscopy (XPS) measurements were done with a PHI Quantum 2000 XPS system with a monochromatic Al-K α source and a charge neutralizer. All the binding energies were referenced to the C1s peak at 284.8 eV of the surface adventitious carbon.

7.2.3 Measurement of Photocatalytic Activity

The photocatalytic oxidation of NO gas was carried out in air at ambient temperature in a continuous flow reactor. The volume of the rectangular reactor which was made of stainless steel and covered with Saint-Glass was 4.5 L (10 \times 30 \times 15 cm (H \times L \times W)). A 300 W tungsten halogen lamp (General Electric) was used as the simulated solar light source. Four UV-A fluorescent lamps (TL 8W/08 BLB, Philips, Holland) were used as the ultraviolet light source and were vertically placed outside the reactor above the sample dish. The lamps had a maximum intensity at 365 nm. Four minifans were fixed around the lamps to cool the system. The weight of the photocatalysts used for each experiment was kept at 0.1 g. The stock NO gas was 48 ppm (N₂ balance, BOC gas) that was traceable to the National Institute of Standards and Technology (NIST) standard. The initial concentration of NO was diluted to about 400 ppb with an air stream supplied by a zero air generator

(Thermo Environmental Inc. Model 111). The relative humidity level of the NO flow was maintained at 70% (2100 ppmv) by passing the zero air streams through a humidification chamber. The gas streams were premixed completely by a gas blender, and the flowrate was controlled at 4 L min⁻¹ by a massflowcontroller. After the adsorption-desorption equilibrium among water vapor, gases, and photocatalysts was achieved, the lamp was turned on. The concentration of NO was continuously measured by using a chemiluminescence NO analyzer (Thermo Environmental Instruments Inc. Model 42c). The removal rate (%) of NO was calculated based on the following equation:

$$\text{NO removal rate (\%)} = ([\text{NO}]_{\text{in}} - [\text{NO}]_{\text{out}}) / [\text{NO}]_{\text{in}} \times 100\%$$

7.3 Results and Discussion

7.3.1 XRD, SEM and TEM Measurements

Fig. 7.1 shows the SEM image of the products with hierarchical architectures, assembled by nanowires. The corresponding XRD pattern of the products is shown in Fig. 7.2a. The pattern can be assigned to a pure tetragonal rutile TiO₂ phase (JCPDS card, 21-1276) with lattice constants $a = 4.593 \text{ \AA}$ and $c = 2.958 \text{ \AA}$. 18 No peaks for other phases are observed, showing the high purity and well crystallinity of the sample. A cross-section of a hemisphere displays the nanowires arrays that grow

radially (Fig. 7.2b). The nanowires are about 2 μm in length. The microstructure is further revealed by the TEM image (Fig. 7.2c). It shows that the superstructure is composed of individual nanowires. The high-resolution transmission electron microscopy (HRTEM) image (Fig. 7.2d) indicates the nanowires are single-crystalline in nature. The growth direction of the nanowires is along the (001) direction. The periodic fringe spacing of ~ 0.32 nm corresponding to the interplanar spacing between the (110) plane is in agreement with the literature value.²² The average diameter for the single nanowire is ~ 7.5 nm. Therefore, the aspect ratio, defined as the length of the major axis divided by the width of the minor axis, is estimated to be 267. Previous reports suggested that 1D ZnO nanostructure arrays, such as nanowires, could exhibit higher photocatalytic activity due to their large aspect ratio.²³⁻²⁵ Thus this rutile TiO_2 superstructure assembled by very high aspect ratio nanowires could be an excellent photocatalyst.



Figure 7.1 SEM image of the self-assembled rutile TiO₂ by microwave heating TiCl₃ at 200 °C for 1 min.

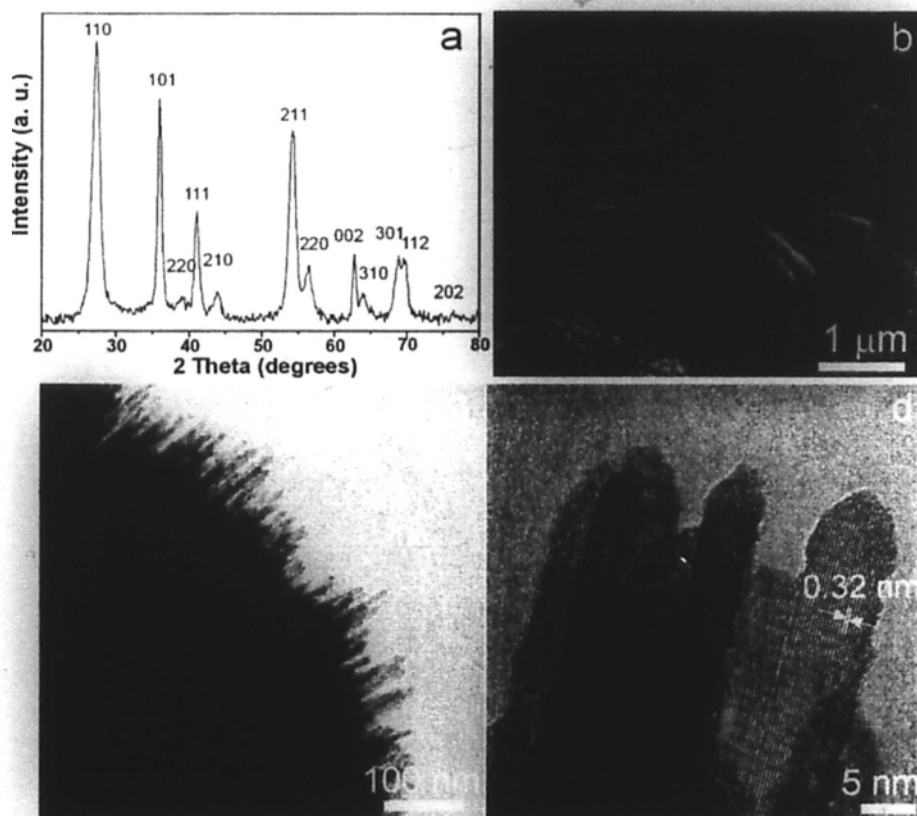


Figure 7.2 XRD pattern (a), SEM (b), TEM (c) and HRTEM (d) image of the self-assembled rutile TiO₂ by microwave heating TiCl₃ at 200 °C for 1 min.

7.3.2 BET Analysis

Nitrogen sorption analyses were conducted to further investigate the textural properties of the rutile TiO₂. The N₂ adsorption-desorption isotherm shows characteristics of porous materials (Fig. 7.3a). The BET specific surface area of the sample is 16 m²/g. There are two capillary condensation steps on the N₂ adsorption-desorption isotherm. These results suggest that the rutile TiO₂ mesocrystal is porous, possessing independently connected mesopores. The first hysteresis loop, $0.2 < P/P_0 < 0.8$, is attributed to the filling of the framework confined smaller mesopores formed between intra-agglomerated primary particles.²⁶ The second hysteresis loop is at $0.8 < P/P_0 < 1$, corresponding to the filling of larger textural mesopores produced by inter-aggregated secondary particles. The results are confirmed by the pore size distribution curve (Fig. 7.3b) calculated from the desorption branch of a nitrogen isotherm by the BJH method using the Halsey equation. Two types of pores can be defined in the sample, including small mesopores (3 nm) and large mesopores (20 nm).

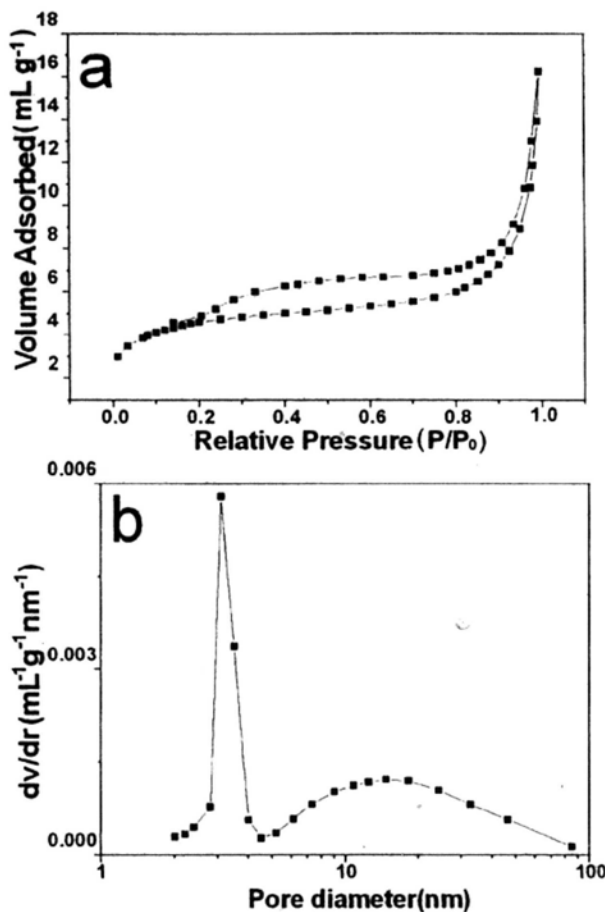


Figure 7.3 Nitrogen adsorption-desorption isotherm (a) and BJH pore size distribution plot (b) of the rutile TiO_2 .

7.3.3 UV/Vis Diffuse Reflectance Spectroscopy

UV/Vis diffuse reflectance spectroscopy (DRS) was used to characterize the electronic states. Fig. 7.4 shows the UV-visible absorption spectrum of the sample. It exhibits a broad absorption band from 200 to 420 nm, indicating the effective photo-absorption property for this hierarchical structure oxide composite photocatalyst system. The band gap energy of this sample can be calculated by using $(\alpha h\nu)^n = k(h\nu - E_g)$, where α is the absorption coefficient, k is the parameter that related to the effective masses associated with the valence and conduction bands, n is

$1/2$ for a direct transition, $h\nu$ is the absorption energy, and E_g is the band gap energy. Plotting $(\alpha h\nu)^{1/2}$ versus $h\nu$ based on the spectral response gives the extrapolated intercept corresponding to the E_g value (see inset of Fig. 7.4). The optical band energies of the rutile TiO_2 (2.80 eV) exhibit an obvious red-shift of 0.2 eV with respect to that of the pure rutile TiO_2 sample (3.00 eV). According to the previous report, the shape definition actually affects the optical properties.²⁷ A series of calculated spectra of Au nanorods with different aspect ratios show that the red-shifted variation of the longitudinal mode appears with increasing aspect ratio.²⁷ Therefore, the red-shift effect may be ascribed to the high aspect ratio of rutile nanowires. These results suggest that the mesocrystals are promising photocatalyst for solar-driven applications.

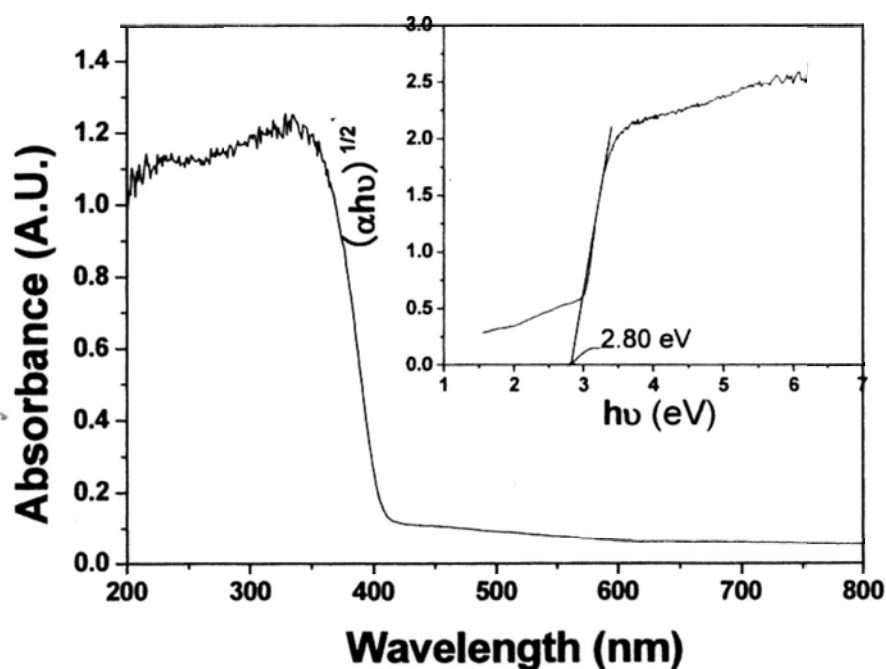


Figure 7.4 UV-visible absorption spectrum and determination of indirect interband transition energy (inset) for the rutile TiO_2 .

7.3.4 Photocatalytic Activity

To evaluate the photocatalytic performance of the rutile TiO₂ mesocrystal, the photo-oxidation of NO gas in a single pass flow was used as a photoreaction probe. Fig. 7.5a and b show the relative variations of NO removal rate against irradiation time in the presence of photocatalysts under ultraviolet and solar light irradiation. As shown in Fig. 7.5a, both commercial Degussa P25 and the prepared rutile TiO₂ photocatalysts exhibit high efficiency for the degradation of NO under UV light irradiation. However, P25 shows little activity under solar light irradiation (shown in Fig. 7.5b) while the removal rate of NO over the rutile TiO₂ photocatalyst reaches 15 % after 5 min irradiation (Fig. 7.5b). After 25 min irradiation, the removal rate of NO is further enhanced to 20 %, which is much better than that of carbon-doped mesoporous TiO₂.²⁸ Such high photocatalytic capability is probably due to the unique rutile TiO₂ nanowires nanostructures, allowing fast charge transport.²⁹ On the high-aspect-ratio nanowires, more photons could be adsorbed and consequently, a much higher quantum efficiency can be obtained. This is because such TiO₂ nanowire array architectures may result in a large effective surface area, thus enabling diffusive transport of photogenerated holes to oxidizable species.³⁰ Furthermore, the micrometer-sized architecture with meso/macro pore structures allows efficient penetration of light and diffusion of NO molecules into the

photocatalyst.³¹ Besides, TiO_2 with macro-scale dimensions is easier to recycle than the nano-sized photocatalytic powders.³² To test the recyclability, a sample after one trial was washed and dried for the subsequent photoreaction cycles. As shown in Fig. 7.6, the NO removal rate for pure rutile TiO_2 mesocrystal was well maintained even after three cycles under solar light irradiation.

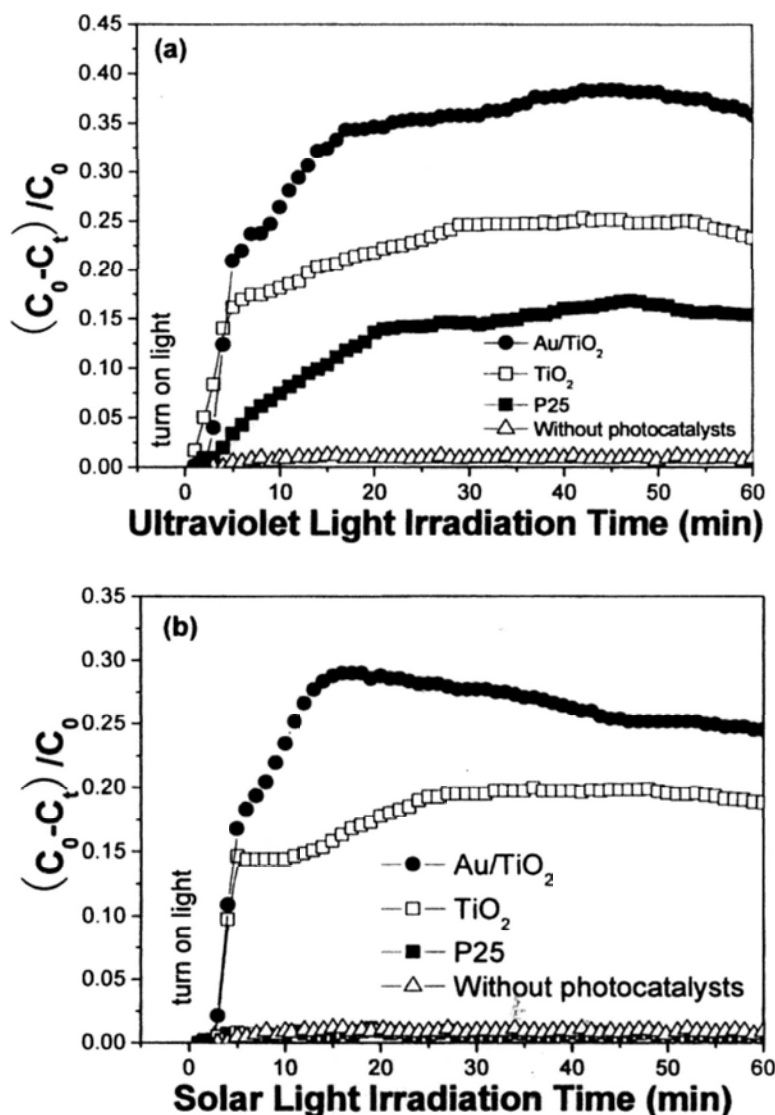


Figure 7.5 NO removal rate of rutile TiO_2 , Au/rutile TiO_2 and P25 in a single pass flow of air under ultraviolet light (a) and simulated solar light (b). Initial concentration of NO = 400 ppb.

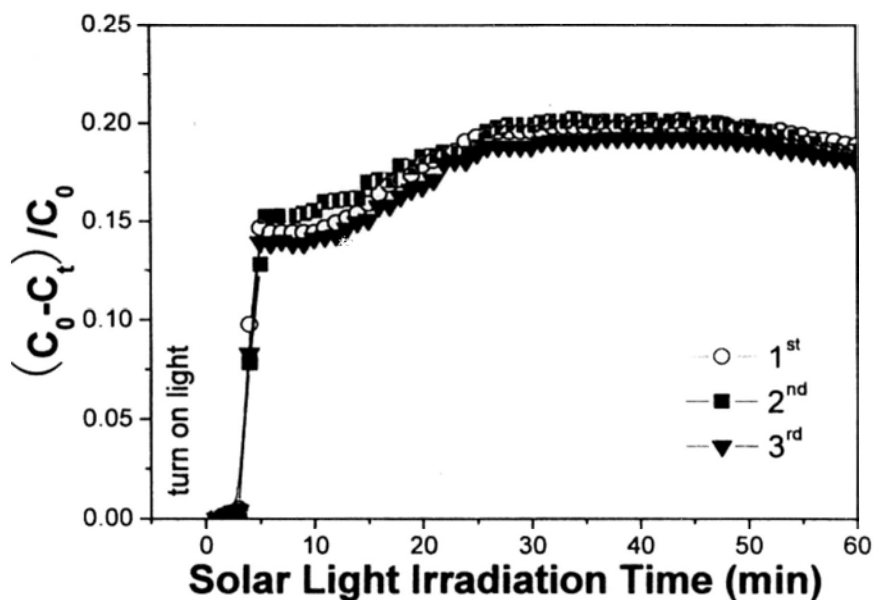


Figure 7.6 Cyclability of the rutile TiO_2 for NO removal in a single pass flow of air.

The photocatalytic activity of the as-prepared rutile TiO_2 can be further improved by incorporating gold nanoparticles on the surface of the nanowires via a green photochemical route to reduce Au^{3+} to Au. Metal gold modification can accelerate the photo-generated electron transition, resulting in a high quantum efficiency.³³ It can also enhance light absorption, taking advantage of the plasmon resonance effect of gold nanoparticles.³⁴ Results show that the loading of 1.0 mol % Au on the rutile TiO_2 would increase the degradation rate from 25 % to nearly 40 % under UV light irradiation (Fig. 7.5a). While under solar light irradiation, 50 % improvement in the photocatalytic performance, which is up to 30 % NO removal rate (Fig. 7.5b), is observed.

X-ray photoelectron spectra (XPS) (Fig. 7.7) show the binding energies (BE) of Au4f7/2 at 83.3 eV and Au4f5/2 at 87.0 eV, suggesting that gold is present in the metallic state. The XPS spectra of Ti2p and O1s indicate a positive shift of about 0.3 eV for gold-doped sample relative to that of pure rutile TiO₂. It indicates a strong interaction between gold and TiO₂. This is further supported by the UV/Vis diffuse reflectance spectroscopy (Fig. 7.8). As shown, the strong absorption at 200-400 nm is characteristic of the rutile TiO₂ phase. Compared to the pure rutile TiO₂, the gold-doped sample exhibits a significantly enhanced absorption in the visible range (500 – 700 nm) owing to the plasmon resonance effect of gold nanoparticles.³⁵

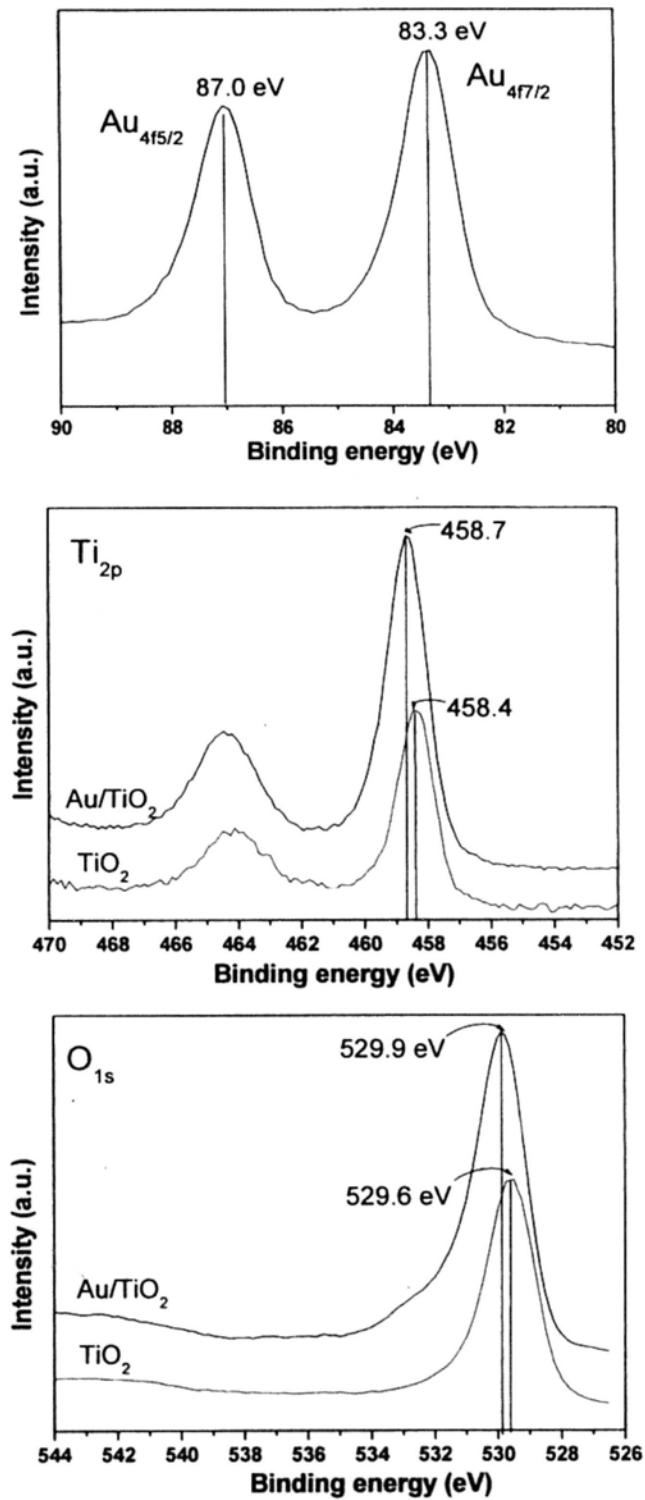


Figure 7.7 XPS spectra of Au4f, Ti2p and O1s of the pure and gold-doped rutile TiO_2 .

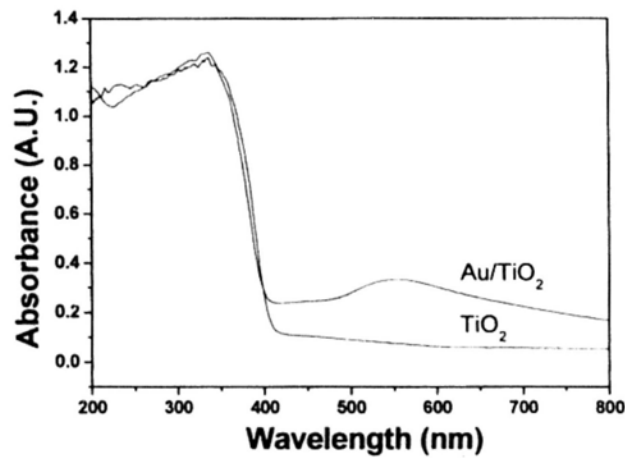


Figure 7.8 UV-visible absorption spectra for the rutile TiO₂ and gold doped rutile TiO₂.

7.4 Conclusion

In summary, we have demonstrated a novel and green synthesis route to the rutile TiO₂ mesocrystals assembled with ultra-long nanowires. We believe our method is fast, cost-effective, energy-saving and environmental friendly. The TiO₂ mesocrystals possess a well crystallized rutile phase, low band gap energy and fast electron transfer property, resulting in an excellent solar-light-driven photocatalytic activity for NO removal in air. Gold modification can greatly enhance the photocatalytic performance of the rutile TiO₂ mesocrystals.

7.5 References

- [1] Cölfen, H.; Antonietti, M. *Angew. Chem., Int. Ed.* **2005**, *44*, 5576.
- [2] Hsu, W. P.; Rönnquist, L.; Matijevic, E. *Langmuir* **1988**, *4*, 31.
- [3] Xu, W.; Antonietti, M.; Cölfen, H.; Fang, Y. P. *Adv. Funct. Mater.* **2006**, *16*, 903.
- [4] Li, M.; Schnablegger, H.; Mann, S. *Nature* **1999**, *402*, 393.
- [5] Fang, J. X.; Ding, B. J.; Song, X. P. *Appl. Phys. Lett.* **2007**, *91*, 083108.
- [6] Halder, A.; Ravishankar, N. *Adv. Mater.* **2007**, *19*, 1854.
- [7] Feng, L.; Li, S. H.; Li, Y. S.; Li, H. J.; Zhang, L. J.; Zhai, J.; Song, Y. L.; Liu, B. Q.; Jiang, L.; Zhu, D. B. *Adv. Mater.* **2002**, *14*, 1857.
- [8] Zhao, Y.; Zhai, J.; Tan, S. X.; Wang, L. F.; Jiang, L.; Zhu, D. B. *Nanotechnology* **2006**, *17*, 2090.
- [9] Fujishima, A.; Honda, K. *Nature* **1972**, *238*, 37.
- [10] Wang, R.; Hashimoto, K.; Fujishima, A.; Chikuni, M.; Kojima, E.; Kitamura, A.; Shimohigoshi, M.; Watanabe, T. *Nature* **1997**, *388*, 431.
- [11] Li, G. S.; Zhang, D. Q.; Yu, J. C. *Environ. Sci. Technol.* **2009**, *43*, 7079.
- [12] Feng, X. J.; Zhai, J.; Jiang, L. *Angew. Chem. Int. Ed.* **2005**, *44*, 5115.
- [13] Yu, J. C.; Li, G. S.; Wang, X. C.; Hu, X. L.; Leung, C. W.; Zhang, Z. D. *Chem. Commun.* **2006**, 2717.

- [14] Li, G. S.; Zhang, D. Q.; Yu, J. C. *Phys. Chem. Chem. Phys.* **2009**, *11*, 3775.
- [15] Sun, W. T.; Zhou, S. Y.; Chen, P.; Peng, L. M. *Chem. Commun.* **2008**, 603.
- [16] Li, G. S.; Zhang, D. Q.; Yu, J. C. *Chem. Mater.* **2008**, *20*, 3983.
- [17] Liu, B.; Zeng, H. C. *Chem. Mater.* **2008**, *20*, 2711.
- [18] Liu, S. J.; Gong, J. Y.; Hu, B.; Yu, S. H. *Cryst. Growth. Des.* **2009**, *9*, 203.
- [19] Xu, H.; Jia, F. L.; Ai, Z. H.; Zhang, L. Z. *Cryst. Growth. Des.* **2007**, *7*, 1216.
- [20] Zhang, D. Q.; Li, G. S.; Yu, J. C. *Chem. Commun.* **2009**, 4381.
- [21] Baruwati, B.; Polshettiwar, V.; Varma, R. S. *Green Chem.* **2009**, *11*, 926.
- [22] Murphy, C. J.; Jana, N. R. *Adv. Mater.* **2002**, *14*, 80.
- [23] Yang, J.; An, S.; Park, W.; Yi, G. *Adv. Mater.* **2004**, *16*, 1661.
- [24] Kuo, T.; Lin, C.; Kuo, C.; Huang, M. H. *Chem. Mater.* **2007**, *19*, 5143.
- [25] Tak, Y.; Kim, H.; Lee, D.; Yong, K. *Chem. Commun.* **2008**, 4585.
- [26] Ho, W. K.; Yu, J. C.; Lee, S. C. *Chem. Commun.* **2006**, 1115.
- [27] Lee, K. S.; El-Sayed, M. A. *J. Phys. Chem. B* **2005**, *109*, 20331.
- [28] Huang, Y.; Ho, W. K.; Lee, S. C.; Zhang, L. Z.; Li, G. S.; Yu, J. C. *Langmuir* **2008**, *24*, 3510.
- [29] Yu, J. G.; Xiang, Q. J.; Zhou, M. H. *Appl. Catal. B: Environ.* **2009**, *90*, 595.
- [30] Park, J. H.; Kim, S.; Bard, A. J. *Nano Lett.* **2006**, *6*, 24.
- [31] Yu, J.C.; Wang, X. C.; Fu, X. Z. *Chem. Mater.* **2004**, *16*, 1523

- [32] Li, G. S.; Yu, J. C.; Zhu, J.; Cao, Y. *Micropor. Mesopor. Mater.* **2007**, *106*, 278.
- [33] Li, H. X.; Bian, Z. F.; Zhu, J.; Huo, Y. N.; Li, H.; Lu, Y. F. *J. Am. Chem. Soc.* **2007**, *129*, 4538.
- [34] Wang, P.; Xie, T. F.; Li, H. Y.; Peng, L.; Zhang, Y.; Wu, T. S.; Pang, S.; Zhao, Y. F.; Wang, D. J. *Chem. Eur. J.* **2009**, *15*, 4366.
- [35] Yonezawa, T.; Matsune, H.; Kunitake, T. *Chem. Mater.* **1999**, *11*, 33.

Chapter Eight

8.1 Conclusions

Various functional materials including magnetic materials and photocatalytic materials were fabricated. Several fast and energy efficient methods were developed for fabricating nanocrystals or mesocrystals with controllable size distributions and morphologies.

Chapter Two reported the synthesis of size-tunable monodispersed hierarchical metallic Ni nanocrystals using an improved solvothermal method. The diameter of the particles could be tuned from 58 nm to 190 nm by simply changing the reaction time. The as synthesized Ni crystals exhibited higher coercivities than the bulk metallic material owing to the reduced size and the hierarchical surface structure. The saturation magnetization (M_s) and the ratio of remanence to saturation (M_r/M_s) increased with increasing particle size.

Chapter Three demonstrated that bismuth oxyhalide semiconductors (BiOBr, BiOCl) with marigold-like open architectures could be prepared by the solvothermal method involving imidazolium-based ionic liquids and ethylene glycol. The use of ionic liquids shortened the reaction time to only 1 hour. The products were effective

photocatalysts for degrading organic pollutants and generating hydrogen.

In Chapter Four, a facile microwave-assisted solvothermal method was developed for the controlled synthesis of novel 3D CdS structures including dendrite-, star-, popcorn- and hollow sphere-like CdS structures. The products with different morphologies exhibited interesting shape-dependent optical properties and photocatalytic activities.

In Chapters Five and Six, biocompatible anatase TiO₂ single-crystals with 27 % – 80 % chemically reactive {001} facets were obtained in 90 minutes by using a microwave-assisted method. The use of microwave heating was critical as it allowed rapid and uniform heating of the reaction mixture. Comparing to TiO₂ without exposing {001} facets, the products exhibited excellent photocatalytic efficiency for both oxidation of nitric oxide in air and degradation of organic compounds in aqueous solution under UV light irradiation.

In Chapter Seven, a simple, fast and environmentally benign microwave-assisted hydrothermal approach was developed for the synthesis of photocatalytically active rutile TiO₂ mesocrystals. Titanium (III) chloride was employed as the only reactant. The reaction time was only 1 min. It was the greenest way to fabricate TiO₂ mesocrystals. Importantly, the products exhibited a high solar-driven photocatalytic oxidation rate for nitric oxide, a gaseous air pollutant responsible for causing

photochemical smog and acid rain.

List of Publications

- (1) **D.Q. Zhang**, G.S. Li, J.C. Yu,* “Inorganic Materials for Photocatalytic Water Disinfection”, *Journal of Materials Chemistry*, **2010**, *20*, 4529-4536.
- (2) **D.Q. Zhang**, G.S. Li, J.C. Yu,* “A Micrometer-Size TiO₂ Single Crystal Photocatalyst with Remarkable 80 % Reactive Facets”, *Chemical Communications*, **2009**, 4381-4383.
- (3) **D.Q. Zhang**, G.S. Li, H.B. Wang, K.M. Chan, J.C. Yu,* “Biocompatible Anatase Single-Crystal Photocatalysts with Tunable Percentage of Reactive Facets”, *Crystal Growth & Design*, **2010**, *10*, 1130-1137.
- (4) **D.Q. Zhang**, G.S. Li, J.C. Yu,* “Synthesis of Size-Tunable Monodispersed Metallic Nickel Nanocrystals without Hot Injection”, *Crystal Growth & Design*, **2009**, *9*, 2812-2815.
- (5) **D.Q. Zhang**, G.S. Li, F. Wang, J.C. Yu,* “Green Synthesis of A Self-Assembled Rutile Mesocrystalline Photocatalyst”, *CrystEngComm*, **2010**, *12*, 1759-1763.
- (6) G.S. Li, **D.Q. Zhang**, J.C. Yu,* M.K.H. Leung,* “An Efficient Bismuth Tungstate Visible-Light-Driven Photocatalyst for Breaking Down Nitric Oxide”, *Environmental Science & Technology*, **2010**, *44*, 4276-4281.
- (7) Q. Tang, **D.Q. Zhang**, S.L. Wang, N. Ke, J.B. Xu, J.C. Yu, Q. Miao* “A

- Meaningful Analogue of Pentacene: Charge Transport, Polymorphs, and Electronic Structures of Dihydrodiazapentacene”, *Chemistry of Materials*, **2009**, *21*, 1400-1405.
- (8) G.S. Li, **D.Q. Zhang**, J.C. Yu,* “A New Visible-Light Photocatalyst: CdS Quantum Dots Embedded mesoporous TiO₂”, *Environmental Science & Technology*, **2009**, *43*, 7079-7085.
- (9) G.S. Li, **D.Q. Zhang**, J.C. Yu,* “Ordered Mesoporous BiVO₄ through Nanocasting: A Superior Visible-Light-Driven Photocatalyst”, *Chemistry of Materials*, **2008**, *20*, 3983-3992.
- (10) G.S. Li, **D.Q. Zhang**, J.C. Yu,* “Thermally Stable Ordered Mesoporous CeO₂/TiO₂ Visible-Light Photocatalysts”, *Physical Chemistry Chemical Physics*, **2009**, *11*, 3775-3782.
- (11) L.S. Zhang, K.H. Wong, **D.Q. Zhang**, C. Hu, J.C. Yu, C.Y.Chan, P.K. Wong*, “Zn:In(OH)_ySz Solid Solution Nanoplates: Synthesis, Characterization, and Photocatalytic Mechanism”, *Environmental Science & Technology*, **2009**, *43*, 7883-7888.
- (12) G.S. Li, J.C. Yu,* **D.Q. Zhang**, X.L. Hu, W.M. Lau, “A Mesoporous TiO_{2-x}N_x Photocatalyst Prepared by Sonication Pretreatment and in-situ Pyrolysis”, *Separation and Purification Technology*, **2009**, *67*, 152-157.